Thermal and Electric Properties of the Delafossites: The Apparent Fermi Liquid Scenario and the Extension of the Density Matrix Renormalization Group Method to Finite Temperatures

Zur Erlangung des akademischen Grades eines
DOKTORS DER NATURWISSENSCHAFTEN
von der Fakultät für Physik des
Karlsruher Instituts für Technologie (KIT)

genehmigte

DISSERTATION

von

Dipl.-Phys. Stefan Kremer
aus Stuttgart

Tag der mündlichen Prüfung	15. Juli 2011
Referent	Prof. Dr. Peter Wölfle Karlsruher Institut für Technologie (KIT)
Korreferent	Prof. Dr. Raymond Frésard ENSICAEN
Korreferent	Dr. Dietmar Weinmann IPCMS-DMONS, Strasbourg
Korreferent	Prof. Dr. Fakher F. Assaad Universität Würzburg

UNIVERSITE de CAEN/BASSE-NORMANDIE

U.F.R. : Sciences

ECOLE DOCTORALE d'appartenance **S.I.M.E.M.**

Cotutelle de thèse
entre
L'Université de Caen Basse-Normandie *(France)*
et
Karlsruhe Institute of Technology (KIT) *(Allemagne)*
Arrêté du 6 janvier 2005

T H E S E

Présentée par

M. Stefan KREMER

et soutenue

Le 15 juillet 2011

En vue de l'obtention du

DOCTORAT de l'UNIVERSITE de CAEN
Spécialité : Milieux denses, matériaux et composants
Arrêté du 7 août 2006

Titre : Propriétés électriques et thermiques des delafossites : Le scénario du liquide de Fermi apparent et l'extension de la méthode DMRG aux températures finies

MEMBRES du JURY

M. Dietmar WEINMANN	Directeur de recherche	CNRS IPCMS-DMONS, STRASBOURG (rapporteur)
M. Fakher F. ASSAAD	Professeur	Université de WÜRZBURG (rapporteur)
M. Peter WÖLFLE	Professeur émérite	KIT, KARLSRUHE (Directeur de thèse étranger)
M. Raymond FRESARD	Professeur	ENSICAEN, CAEN (Directeur de thèse français)
M. Thilo KOPP	Professeur	Université de AUGSBURG
M. Hilbert v. LÖHNEYSEN	Professeur	KIT, KARLSRUHE
M. Dieter ZEPPENFELD	Professeur	KIT, KARLSRUHE
M. Christoph KOTTMEIER	Professeur	KIT, KARLSRUHE

RÉSUMÉ en français
Dans cette thèse, des méthodes sont présentées pour accéder aux propriétés physiques dans un régime de températures intermédiaires. Cela comporte non seulement des techniques numériques mais aussi des méthodes analytiques. Les premières sont discutées dans le cadre du groupe de renormalisation de la matrice densité, dans le but de décrire des systèmes possédant une échelle de température par un ensemble d'états. Les autres sont appliquées à la densité d'états de systèmes quasi-bidimensionnels qui sont considérés comme un bon modèle pour décrire les delafossites, dont les propriétés thermoélectriques attirent beaucoup d'intérêt. De plus, leur comportement présente de fortes similitudes avec le liquide de Fermi, mais à haute température. Ce comportement est analysé par les méthodes proposées. En outre, nous montrons qu'il est possible d'extraire des propriétés de la densité d'états et le dopage de ces matériaux dans ce cadre.

TITRE en anglais
Thermal and Electric Properties of the Delafossites:
The Apparent Fermi Liquid Scenario and the Extension of the Density Matrix Renormalization Group Method to Finite Temperatures

RÉSUMÉ en anglais
This work aims to propose techniques to access physical properties at intermediate temperature scales. These methods include both numerical ones on the one hand and analytic ones on the other. The former ones operate within the framework of the density matrix renormalization group aiming to characterize a system at finite temperature by a set of states. The latter ones are applied to the density of states of slightly modified two-dimensional systems which are believed to describe the delafossite compounds. These materials recently attracted a huge interest due to their thermoelectric properties, but have revealed a behavior at intermediate temperatures resembling a Fermi liquid one. This behavior is examined with the proposed methods. Furthermore, it is shown that properties of the density of states as well as the charge carrier density of those materials can be extracted from a careful study.

MOTS-CLES INDEXATION RAMEAU

Thermoélectricité	Thermoelectricity
Thermodynamique	Thermodynamics
Physique en basse dimension	
Structure électronique	Electronic structure
Électrons – corrélation	Electron configuration
Physique numérique	Numerical physics – DMRG
Delafossites	Delafossites

DISCIPLINE
Milieux denses, matériaux et composants

INTITULE et ADRESSE du LABORATOIRE
Laboratoire Crismat-ENSICAEN
6, Bld. du Maréchal Juin
F-14050 Caen CEDEX 4

Contents

Abstract

This work aims to propose techniques to access physical properties at intermediate temperature scales. These methods include both numerical ones on the one hand and analytic ones on the other. The former ones operate within the framework of the density matrix renormalization group aiming to characterize a system at finite temperature by a set of states. The latter ones are applied to the density of states of slightly modified two-dimensional systems which are believed to describe the delafossite compounds. These materials recently attracted a huge interest due to their thermoelectric properties, but have revealed a behavior at intermediate temperatures resembling a Fermi liquid one. This behavior is examined with the proposed methods. Furthermore, it is shown that properties of the density of states as well as the charge carrier density of those materials can be extracted from a careful study.

Résumé

Dans cette thèse, des méthodes sont présentées pour accéder aux propriétés physiques dans un régime de températures intermédiaires. Cela comporte non seulement des techniques numériques mais aussi des méthodes analytiques. Les premières sont discutées dans le cadre du groupe de renormalisation de la matrice densité, dans le but de décrire des systèmes possédant une échelle de température par un ensemble d'états. Les autres sont appliquées à la densité d'états de systèmes quasi-bidimensionnels qui sont considérés comme un bon modèle pour décrire les delafossites, dont les propriétés thermoélectriques attirent beaucoup d'intérêt. De plus, leur comportement présente de fortes similitudes avec le liquide de Fermi, mais à haute température. Ce comportement est analysé par les méthodes proposées. En outre, nous montrons qu'il est possible d'extraire des propriétés de la densité d'états et le dopage de ces matériaux dans ce cadre.

Kurzbeschreibung

Ziel dieser Arbeit ist es Methoden vorzustellen, die Temperaturbereiche zwischen der Hoch- und Tieftemperaturentwicklung erschließen können. Dies beinhaltet einerseits numerische, andererseits aber auch analytische Vorgehensweisen. Erstgenannte Methoden arbeiten im Rahmen der Dichtematrix-Renormalisierungsgruppe, um Systeme bei endlicher Temperatur durch eine Vielzahl von Zuständen zu beschreiben. Die anderen Vorgehensweisen werden auf eine leicht modifizierte zweidimensionale Zustandsdichte angewendet, welche die Klasse der Delafossite beschreibt. Diese Materialien stehen seit kurzem wegen ihrer thermoelektrischen Eigenschaften im Fokus der Wissenschaft. Zudem zeigen sie ein Verhalten, das stark einer Fermiflüssigkeit ähnlet – allerdings bei Raumtemperatur. Dieses Verhalten wird mit den vorgeschlagenen Vorgehensweisen untersucht. Dabei wird dargestellt, wie Eigenschaften der Zustandsdichte sowie der Dotierung aus einer solchen Untersuchung ermittelt werden können.

Chapter 1

Introduction

1.1 Motivation

Humanity has always struggled with the goal of conserving energy. While ages ago this meant conserving the strength of one's own body in order to activate energy reserves in case a predator appears, nowadays we think more globally about how to deal with the limited resources of our planet. In the process of using renewable energies, reusing wasted energy has been put into focus as well. In particular, car industry found that nearly two thirds of the energy stored in gasoline is blown out of the exhausting pipe as heat. As a

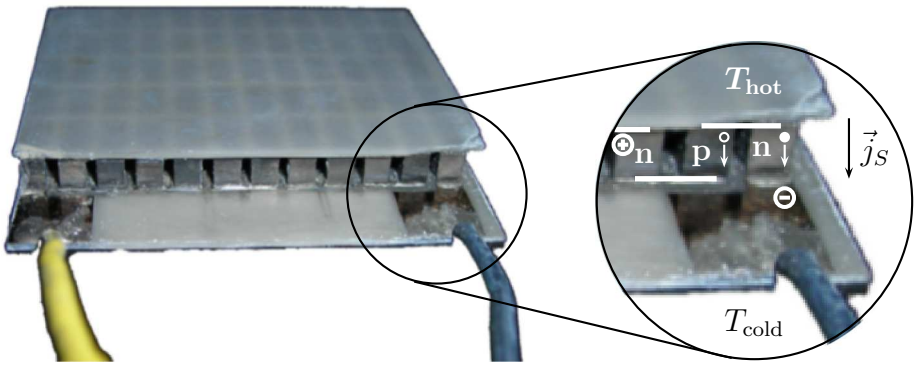

Figure 1.1: One element of a thermoelectric generator [1] consists of serial connected pairs of thermoelectric materials (here: differently doped semi-conductors denoted by n and p) which are meandered. If the upper area is connected to a hot reservoir T_{hot}, entropy is transported towards the lower plane at T_{cold} by different kind of charge carriers inside the pairs symbolized by $\circ$ and $\bullet$. The lower end of a material with negative charge carriers will therefore be placed on a lower electronic potential $\ominus$ than the one with hole-like charge carriers. Hence, an electric voltage bias is generated. The ratio of this conversion of heat energy into electrical energy is defined as the thermopower.

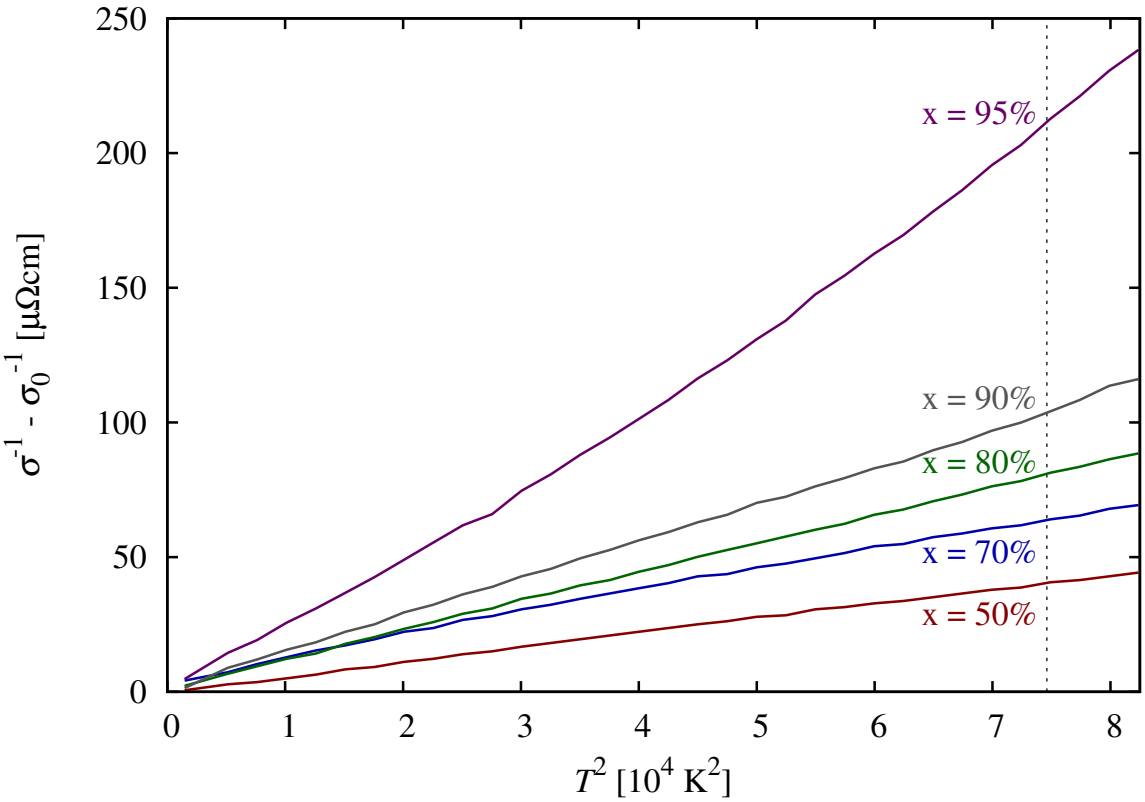

Figure 1.2: The quadratic behavior of the electronic contribution to the resistivity σ^{-1} from Fermi liquid theory showed to be valid up to the freezing point of water (dotted temperature on the right-hand side) and above in titanates $Sr_{1-x}La_xTiO_3$ according to [18].

solution various enterprises are trying to make this wasted heat again available by the use of thermoelectric generators [2].

Since the first days of space exploration those generators were used in order to power self-contained probes by means of the heat of radioactive materials [3]. However, the success of this technology in everyday life was hindered until now by issues concerning the efficiency of these generators. In order to overcome this drawback such generators consist of multiple layers of thermoelectric elements which are built up of only two wisely chosen, alternately stacked materials (cf. Fig. 1.1). The important feature of these materials is that they differ in the sign of the thermopower $S = \Delta V/\Delta T$, the final voltage drop ΔV which lies at the electrically disconnected material related to the applied temperature difference $\Delta T = T_{\text{hot}} - T_{\text{cold}}$. The maximum efficiency η of energy conversion of one pair of those materials with similar absolute value of their material properties is then given by the thermopower [4]:

$$\eta = \eta_{\text{Carnot}} \left[\frac{\sqrt{1+ZT}-1}{\sqrt{1+ZT}+T_{\text{cold}}/T_{\text{hot}}} \right] \qquad \text{with} \qquad Z = S^2 \frac{\sigma}{\kappa}\,, \tag{1.1}$$

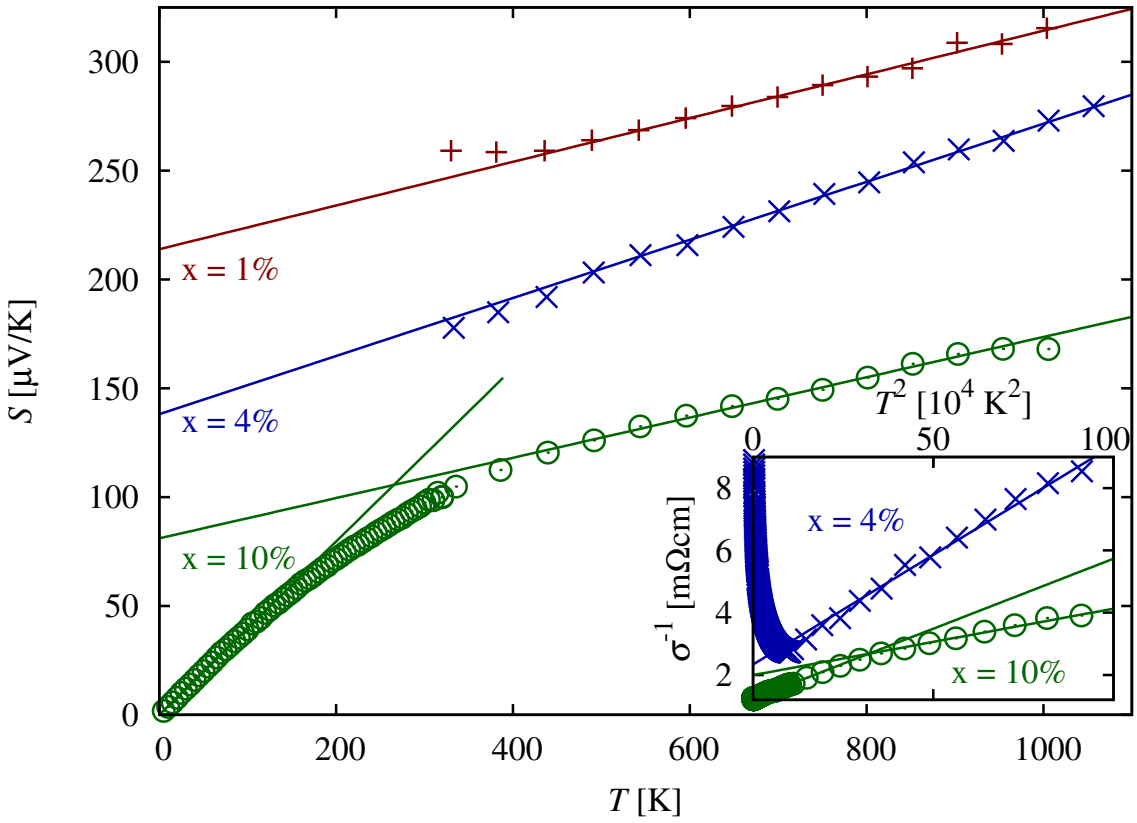

Figure 1.3: The thermopower of Mg-doped $CuRhO_2$ shows above room temperature a linear behavior while the resistivity (inset) is characterized by a quadratic behavior with respect to temperature. In addition, for the highest doped sample another linear (quadratic) region with a different coefficient is observed at low temperature [23].

where η_{Carnot} specifies the maximal obtainable efficiency as given in a Carnot process, $T = (T_{\text{hot}} + T_{\text{cold}})/2$ denotes the averaged temperature, while σ and κ represent the electrical and heat conductivity of the used thermoelectric material whose ratio is often fixed by the Wiedeman-Franz law [5, 6]. Promising candidates, like manganites [7], titanates [8], clathrates [9, 10], skutterudites [11] or delafossites [12–15], showed that high efficiency can be obtained from correlated metals with narrow bands [16] as well as band insulators with sharp band edges [17].

Furthermore, since the goal is a high efficiency at room temperature it might question the use of theoretical frameworks, like Fermi liquid theory, since they usually contain low temperature expansions. Nevertheless, some materials like the titanates have shown a broad temperature region where the behavior from Fermi liquids theory is valid even up to room temperature (cf. Fig. 1.2) [18]. As will be shown in section 2.3, this theory leads to a quadratic resistivity and a linear thermopower with respect to temperature. Such a

behavior has been found in the materials mentioned below (1.1), although deviations were noticed at very low temperature (cf. Fig. 1.3). Additionally, in some cases an offset was observed too [19–21]. In measuring the low temperature behavior of these quantities for some delafossites [22, 23] a Fermi liquid behavior was obtained at low temperature which contains a different slope in the thermopower, respectively a different quadratic coefficient in the resistivity and where no offsets were required. Thus revealing the behavior at room temperature to be apparently a Fermi liquid behavior. This phenomenon might be explained by a structural phase transition, but this has never been evidenced experimentally. For other explanations of this behavior, which will be called an apparent Fermi liquid (AFL) one, theoretical tools have to be introduced in order to access this intermediate temperature range.

Before addressing this question in chapter 3 and 4, the key aspects of the materials, where this kind of behavior was found, is addressed in the following section 1.2. Chapter 2 will then introduce the theoretical framework of accessing quantities which are dependent on temperature in general, where the observed Fermi liquid behavior is quantitatively explained too. The final chapter 5 will summarize the results.

1.2 The Delafossites

In 1873 Friedel named the commonly found mineral $CuFeO_2$ after his colleague Gabriel Delafosse [24]. Nearly a century later it was shown that in the same structure several compounds crystallize, allowing a systematic study of the group which was therefore called the delafossites [25, 26]. In this group, copper could even be replaced by platinum, palladium or silver, leading to rarely known crystalline oxides of noble metals. However, these substances are not so important for thermoelectric applications since this replacement leads to a d^9 configuration of the substituents and therefore a metallic behavior with a good heat conductivity (cf. (1.1)).

More important in this sense is the semi-conductor class. Additionally, it shows a rich variety of physical systems due to an underlying low dimensional structure. This range reaches from band insulators, like $CuRhO_2$ [19] over multiferroica, like doped $CuFeO_2$ [27], to Mott-insulators, like $CuCrO_2$ [28, 29], where an AFL behavior has been observed for doped systems too. In section 4.5 and 4.6, the former and latter materials will be used to apply the theory described in this work. The physics of these materials are governed by the substituent of iron since the other metallic atom in the unit cell is in a d^{10} configuration in this case. The observed effects of strong correlation is due to the close oxygen atoms, mediating a superexchange coupling between these atoms (cf. Fig. 1.4). Moreover, the oxygen atoms are octrahedraly coordinated around these atoms. From group theory as well as from a near field expansion of the crystal field the five d-orbitals will split into the two-fold degenerate e_g and the three-fold degenerate t_{2g} states [30]. Thus the different shifts in energy of these states arising from the crystal field explains the semi-conductor gap.

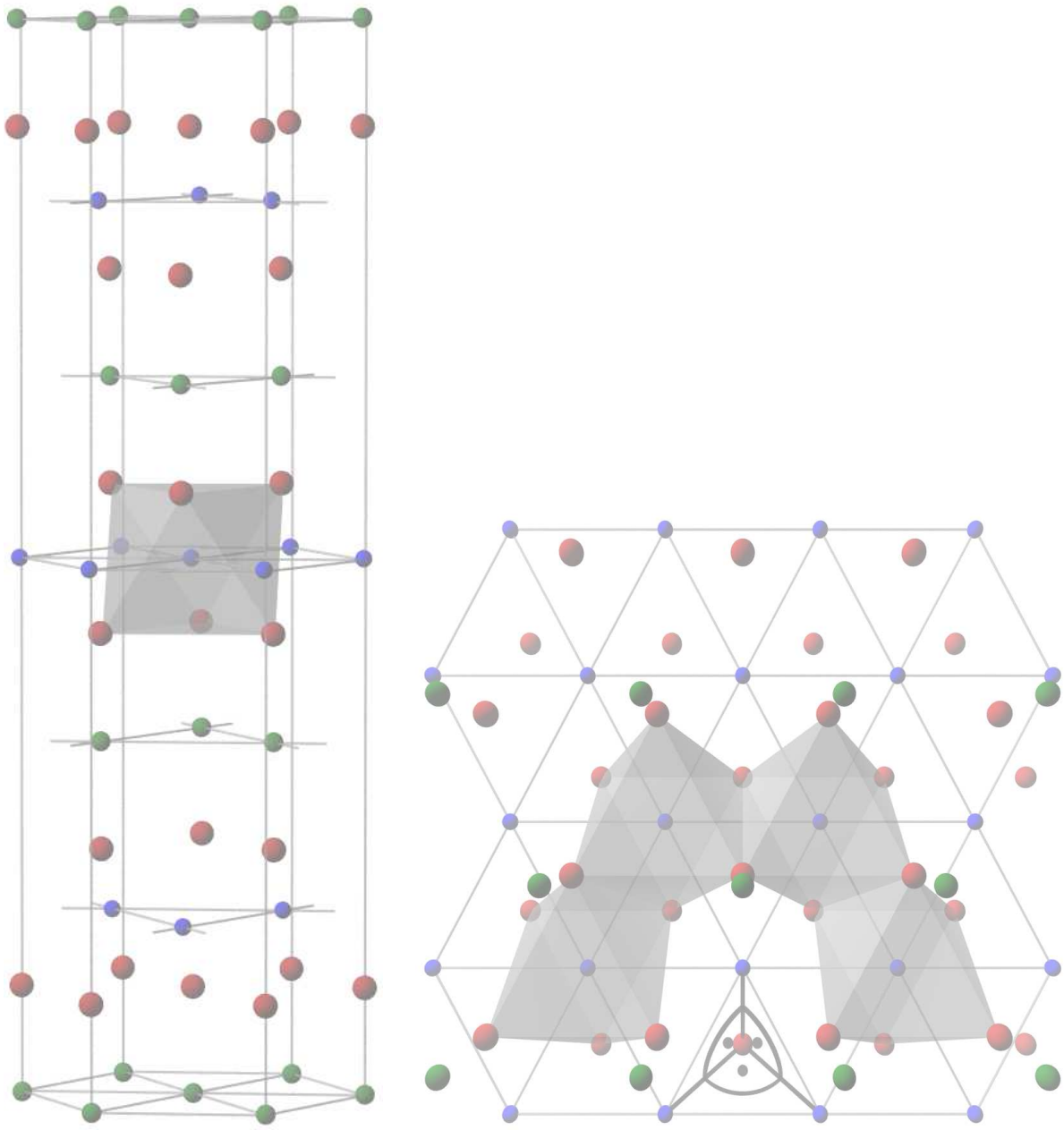

a) Unit cell b) Connections of the octahedrons inside a layer

Figure 1.4: The structure of the delafossites (left) consists of hexagonal layers (right) of one kind of atoms (blue) octahedrally coordinated (gray octahedrons) with oxygen ones (red). The axis from the oxygen atoms to those of the transition metal inside the layers are therefore perpendicular (bottom right). The layers are separated by another kind of atoms (green), which are the copper ones for the original $CuFeO_2$. Furthermore, the layers are slightly shifted leading to a rombohedral system with space group $R\bar{3}m$.

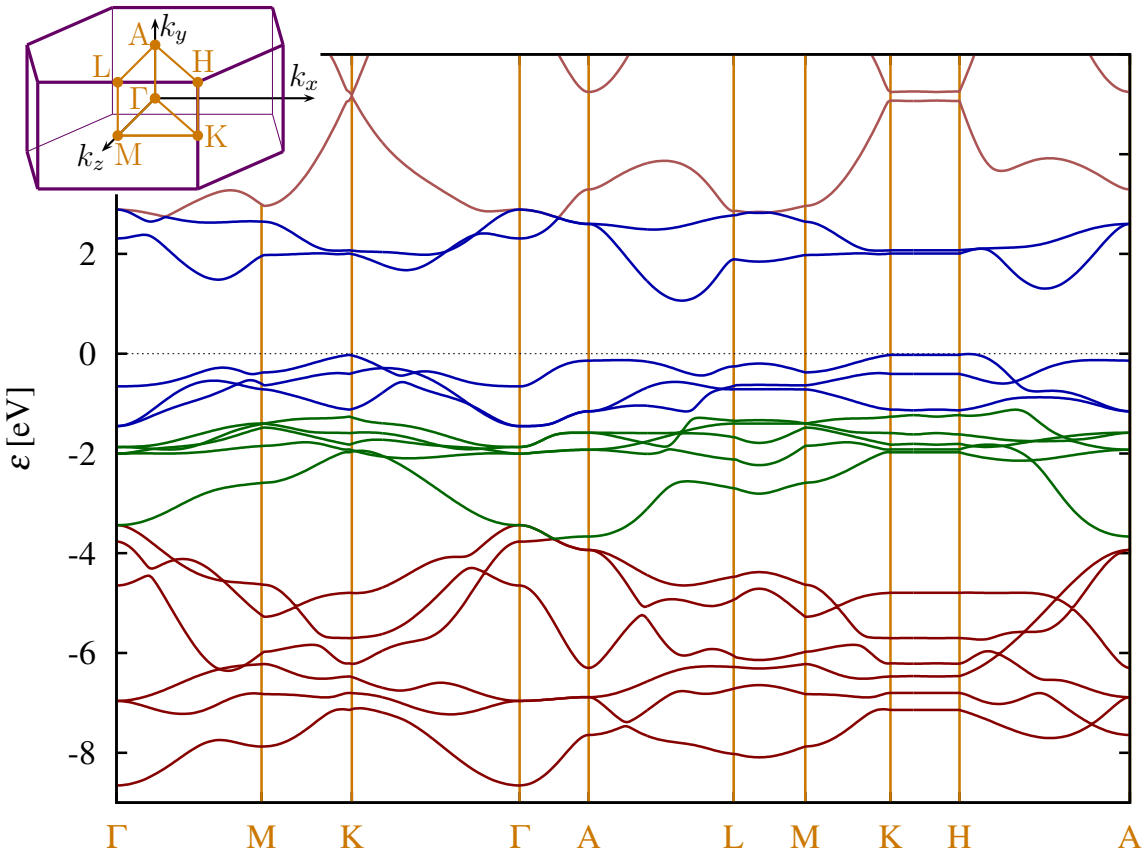

Figure 1.5: The electronic band structure of $CuRhO_2$ (where the zero point of energy was placed at the upper band edge of the highest occupied band dominated by the t_{2g}-orbitals of rhodium) as calculated by the augmented spherical wave method according to [19], shows a dispersionless region along the direction K-H (with respect to the Brillouin zone pictured on the left-hand side). The colors of the band distinguish the dominant contribution of atoms in the unit cell according to Fig. 1.4.

These octahedrons form layers which are separated by the copper atoms, like in the perovskite structure. However, in contrast to this structure the layers are closer since neighboring octahedrons not only share two, but three oxygen atoms. Therefore the layers form a hexagonal lattice. Furthermore, the directions from the oxygen atoms to the low dimensional lattice atoms form an angle of 90°. Thus, the p-orbitals of the oxygen atoms with maximum overlap to the lattice atoms do not overlap with each other. This would lead to an insulating behavior even if the layer is doped. In contrast, experimentally, a metallic behavior is observed in the doped case. Therefore small influences, like the asymmetric configuration of the oxygen atoms in the crystal field, can cause significant change in physical properties, leading to a perturbation of the two-dimensional environment.

In order to consider all atoms in the unit cell, density functional theory as well as augmented spherical wave methods have been applied to several classes of delafossites to determine their electronic structure [19, 29, 31–36]. In some studies even the thermopower could be accessed within the constant scattering time approximation of Boltzmann transport theory [19, 33, 36]. In these investigations a strong increase of states at the band edge was observed. Moreover, a recent one [19] revealed a dispersionless region in the vicinity of the Fermi energy along a particular direction of the Brillouin zone (cf. Fig. 1.5). This feature can be viewed as the residual effect of the previously described underlying two-dimensional structure. Conclusively, this leads to a discontinuous augmentation of the density of states at the band edge.

While on the one hand, such features might be difficult to resolve numerically, physical properties on the other are known to be strongly dependent on such analytic anomalies. As found for other anomalies, like a cusp in the density of states [37] or Van-Hove singularities [38, 39], this could render other phases observable, like marginal Fermi liquid ones [38]. Furthermore, the discontinuous band edge can be seen as a quantum phase transition [40] where a metal-insulator transition occurs varying with the (doping dependent) Fermi energy. Therefore the presence of a discontinuous density of states could cause novel phases to emerge which might explain the observed AFL behavior.

Chapter 2

Temperature Dependence of Physical Quantities

In this chapter, the general theoretical framework of the calculation of physical quantities, which are dependent on temperature, is discussed. The first section introduces the key attributes by which clean physical systems are described. In particular, a simplified microscopic model is introduced, to which the numerical techniques proposed in chapter 3 will later be applied. Afterwards, the formalism for the calculation of thermodynamic properties in section 2.2 as well as transport properties in section 2.3 is discussed, in order to understand the previously mentioned low temperature behavior of Fermi liquid theory.

Of course, this chapter should not be understood as replacing a profound study on these topics but rather to summarize the key aspects qualitatively in order to illustrate the point of the methods in the following chapters, as well as to distinguish the Fermi liquid behavior from those later described. However, since the numerical computation in chapter 3 is often done for fixed particle number, a method to calculate thermodynamic quantities in this case is explained in order to obtain reference curves. In addition, an approximation is introduced which enables the determination of the thermopower by equilibrium properties in particular cases. For a thorough survey of the other topics the reader should refer to further literature [41–44].

2.1 Non-interacting and Interacting Fermions

Quantum-mechanical particles are usually separated into two groups. Those which can occupy the same quantum-mechanical state multiple times and those which can do so only once. This work will consider only the latter one, in particular those which have an anti-symmetric wave function and are named fermions. If the particles do not interact with each other, the particles can move freely (with respect to the motion of the other particles) and one superposes the wave function of each particle. This means the allowed energies of the whole system E is fully determined by the single-particle energies ε. The

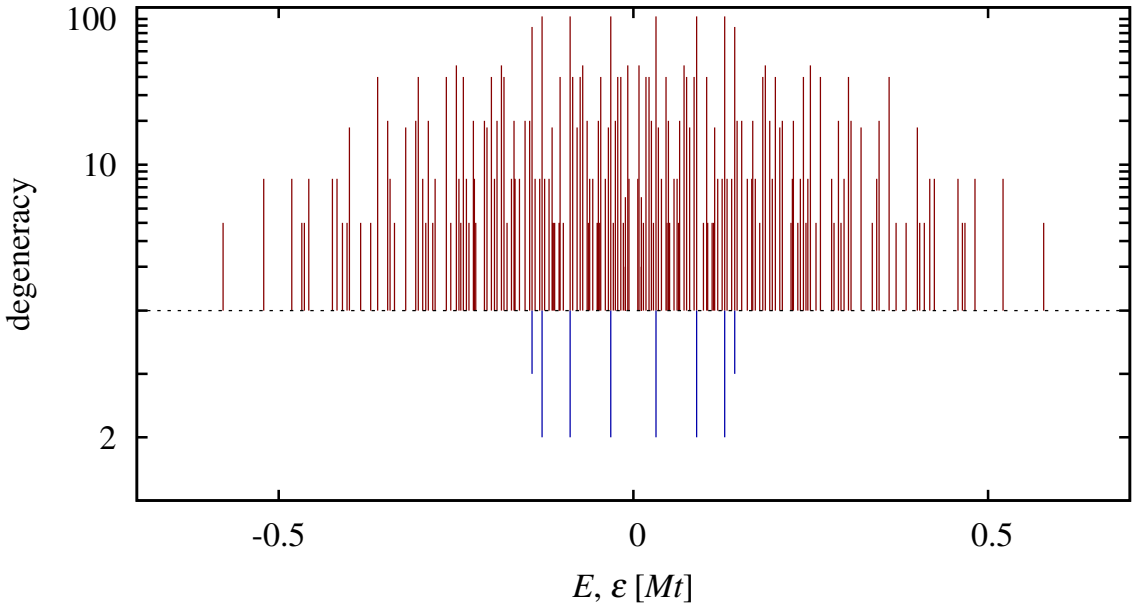

Figure 2.1: The distribution and degeneracy of the energy levels of the ring described by (2.3) with $M = 14$ sites and $N = 7$ fermion where no interaction is present $V = 0$. Upwards the many-body energies are shown on a logarithmic scale while downwards the single-particle ones can be viewed on an ordinary scale. Apparently the number of states greatly increases for the former ones as are the possible number of degenerate levels. The different gap sizes will play an important role later on.

latter quantity usually depends on various quantum numbers including the spin. However, in fully polarized systems the spin dependency can be neglected, naming the considered fermions spinless. For convenience the other quantum numbers will be represented only by one multi index k which becomes only a single index for one-dimensional systems.

In contrast, for interacting fermions, e.g. electrons which repel each other by the Coulomb interaction, the self-energy $\Sigma(\omega, k)$ further enters, which appears in the single-particle Green's function

$$G(\omega, k) = \frac{1}{\omega - \varepsilon_k - \Sigma(\omega, k)}\,, \tag{2.1}$$

where ω denotes the Fourier transformed variable of time dependency scaled by the reduced Planck constant $\hbar$. For small interaction strength Fermi liquid theory is often applicable. Thereby the energy levels vary only adiabatically, leading to small changes in the self energy. The real part of this quantity modifies then the dispersion relation only slightly leading to a renormalization of parameters entering the single-particle energies ε_k, like the introduction of an effective mass. However, since the self-energy can obtain complex values, its imaginary part can lead to qualitative new features. In particular, in Fermi

liquid theory this part is interpreted as the inverse of a finite lifetime,

$$\tau^{-1}(\varepsilon) = \left.\operatorname{Im}\Sigma(\varepsilon, k)\right|_{\varepsilon=\varepsilon_k}, \tag{2.2}$$

of the quasi-particles with energy ε. This interpretation is due to the fact that, unlike in the non-interacting case, the superposition of single-particle states are no longer eigenstates of the full Hamiltonian. Therefore these single-particle states of the quasi-particles will decay into many-body states. In general, it is therefore necessary to consider these states which are usually described by the occupation number formalism, where the many-body states are represented by the occupation numbers of each site. Respectively, it is more appropriate to look at the many-body energies E than the single-particle ones ε (cf. Fig. 2.1). This spectrum is broader and can obtain huge values of the degeneracy, especially in the non-interacting case.

A simple system which exemplifies this difference and which is not described by a Fermi liquid picture is a one-dimensional one where N spinless fermions are distributed on M sites (cf. Fig. 2.2). For instance, it can be interpreted as one empty orbital of each of the considered atoms, forming a ring in real space. Therefore in the case of $M = 6$ this system can be seen as a simplified model of benzene, but larger rings can be realized experimentally too [45, 46]. In the theoretical description the fermions are assumed to be able to hop only to the closest sites with the hopping amplitude t. Additionally, an interaction V is present between these neighboring sites. Therefore the Hamilton operator takes in second quantization the form

$$\hat{H} = t\sum_{j=1}^{M}(\hat{c}_{j+1}^{\dagger}\,\hat{c}_j + \hat{c}_j^{\dagger}\,\hat{c}_{j+1}) + V\sum_{j=1}^{M}\hat{n}_j\,\hat{n}_{j+1}\,, \tag{2.3}$$

where $\hat{n}_j = \hat{c}_j^{\dagger}\,\hat{c}_j$ is the occupation operator and the operator $\hat{c}_j$ destroys, respectively $\hat{c}_j^{\dagger}$ creates, a fermion at the site j which can be occupied only once by one fermion. This leads to the algebra described by

$$\{\hat{c}_i, \hat{c}_j^{\dagger}\} = \delta_{i,j}\,. \tag{2.4}$$

Additionally, the ring geometry is considered by identifying the site $M + 1$ with the first one, i.e. $\hat{c}_{M+1} = \hat{c}_1$, but could be modified by an additional phase if a magnetic field is taken into account [47–54]. In addition, the model can include diagonal disorder by adding terms for each site j which are proportional to $\hat{n}_j$ [50–54]. Afterwards, a stochastic sampling over ensembles with different proportionality constants is performed. The clean model can also be mapped on a spin-½-chain, namely the XXZ model by a Jordan-Wigner transformation [55].

In the case of the non-interacting system $V = 0$ the Hamiltonian can easily be diagonalized by a Fourier transformation

$$\hat{c}_j = \frac{1}{\sqrt{M}}\sum_k \mathrm{e}^{-ijk}\,\hat{\tilde{c}}_k \qquad \text{with} \qquad k \in \left\{\frac{2\pi}{M}n \,\middle|\, n \in \{1, 2, \ldots, M\}\right\}, \tag{2.5}$$

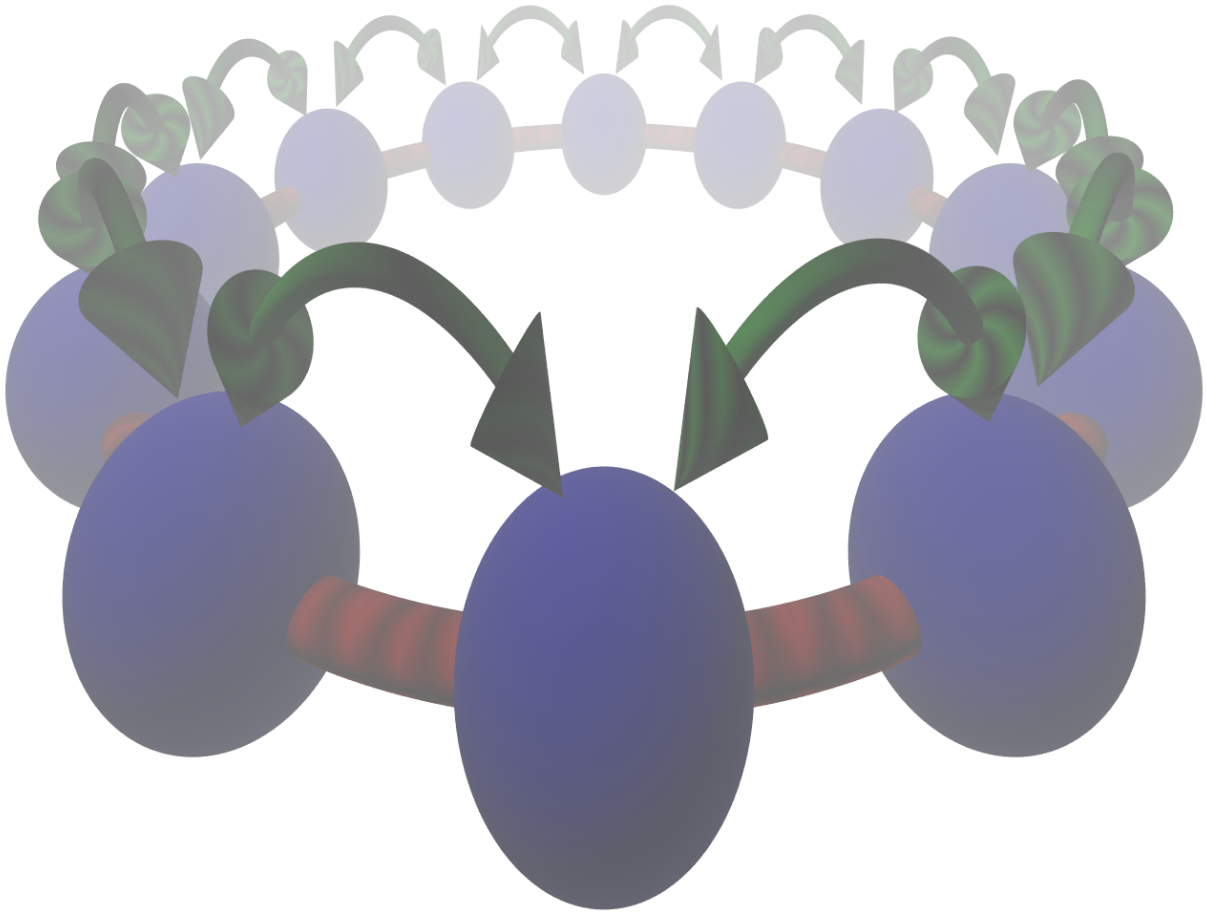

Figure 2.2: The system modeled by (2.3) where the blue spheres represent the sites which can be singly occupied by a fermion. These particles can interact with fermions on neighboring sites, illustrated by the red connections, or can hop to those sites if they are not occupied (green arrows).

where $\hat{\tilde{c}}_k$ is the transformed annihilation operator. This leads to the single-particle energies to be given by

$$\varepsilon_k = -2t \cos k \,. \tag{2.6}$$

While at finite system sizes M a gap is obtained due to the discrete spectrum, the finite size gap vanishes in the limit of infinite system size $M \to \infty$, and the momentum k becomes continuous leading to a continuous dispersion relation ε_k. Furthermore, the appearance of this quantity as a quantum number means that the fermions are fully delocalized throughout the ring. Since the particles can not circumvent each other in the one-dimensional environment, in the case of small interaction strength the low-energy excitations are collective modes which are no longer characterized by the framework of Fermi liquid theory, but by the description of a Luttinger liquid [56–58].

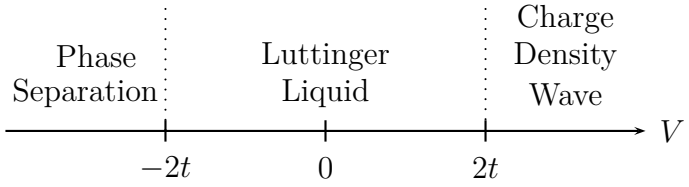

Figure 2.3: Phase diagram of the ring (2.3) in the thermodynamic limit.

In contrast, if the Hamiltonian (2.3) is dominated by the interaction part ($t = 0$), the ground state changes qualitatively. On the one hand, if an attractive interaction $V < 0$ is present, all particles will accumulate in one region of the system. Therefore the ground state describing this phase separation would be M-fold degenerate and consists of the states

$$|\underbrace{\bullet\bullet\cdots\bullet}_{N}\underbrace{\circ\circ\cdots\circ}_{M-N}\rangle, \qquad |\circ\underbrace{\bullet\bullet\cdots\bullet}_{N}\underbrace{\circ\circ\cdots\circ}_{M-N-1}\rangle, \ldots \tag{2.7}$$

where $\bullet$ describes an occupied and $\circ$ an empty site, thus distinguishing this state from the one obtained by (2.5). On the other hand for repulsive interaction $V > 0$ unoccupied sites between the fermions are favorable. For an even number of sites M and exactly at half filling $N = M/2$ only two states are therefore possible for the ground state where the sites are alternately occupied in real space

$$|\bullet\circ\bullet\circ\cdots\rangle \qquad \text{and} \qquad |\circ\bullet\circ\bullet\cdots\rangle\,. \tag{2.8}$$

Since the fermions usually carry charges, this phase is called a charge density wave. Furthermore, moving a particle to another site for both phases would need a finite amount of energy due to the finite interaction strength V. Therefore a gap arises between the ground state and the first excited state which is not due to the finite system size, in contrast to the non-interacting system. Thus, the system resembles a charge density wave insulator in contrast to the metallic behavior of the non-interacting system. Similarly, an electron-phonon interaction instead of the discussed electron-electron one would result in a charge density wave as well, leading to a Peierls insulator due to the resulting deformation of the one-dimensional lattice [59–61]. Furthermore, such a transition has been suggested in the two-dimensional analog of this model, too [62, 63].

Therefore, for the general case of the Hamiltonian (2.3) two phase transitions between these phases are expected (cf. Fig. 2.3). From the Bethe Ansatz [64–67] as well as from the density matrix renormalization group method (DMRG) [68], which will be discussed in section 3.2, the transition points have been found at $V = \pm 2t$. While for the charge density wave this transition will only occur at half filling $N = M/2$, the transition point at the edge of the phase separation phase is independent of the particle number in contrast to systems like the t-J model where the spin of the fermions is taken into account [69, 70]. Furthermore, since the argument was made by only varying the interaction strength V as system parameter both transitions should take place even at vanishing temperature. This kind of transitions are therefore called quantum phase transition [40] in contrast to thermal driven ones, like the melting of ice.

2.2 Thermodynamic Properties

When considering physical systems, properties might change with different boundary conditions. In particular, the system might interchange particles with its environment leading to the distinction between the grand canonical ensemble, where this is possible, and the canonical one, where this is restrained. The resulting thermodynamic properties, like the specific heat C, differ for both cases in general, but can easily be calculated for non-interacting fermions.

The basic quantity that defines thermodynamic properties is the partition function Z. In general, this quantity can be obtained by trying to maximize the statistically defined entropy $\mathcal{S}$ under the constraints given by the considered ensemble and the norm of the probability distribution. In another approach it is obtained as the normalization of the statistical operator $\hat{W}$ of the system. This operator can be calculated from the total statistical operator describing the system and the environment, if the degrees of freedom of the environment are traced out

$$\hat{W} = \operatorname{Tr}_{\text{environment}} \hat{W}_{\text{total}} \,. \tag{2.9}$$

Furthermore, assuming a large enough environment means that the variation on the energy and particle expectation value will be small. Therefore the logarithm of the resulting statistical operator can be expanded to first order in these quantities

$$\hat{W} \propto \mathrm{e}^{-\beta\left(\hat{H}-\langle\hat{H}\rangle\right)+\beta\mu\left(\hat{N}-\langle\hat{N}\rangle\right)+\dots} \,, \tag{2.10}$$

where the coefficients have already been associated as the inverse temperature $\beta = 1/k_{\mathrm{B}}T$ where k_{B} denotes the Boltzmann constant, and the chemical potential μ. For the partition function this leads to

$$Z_\mu = \operatorname{Tr} \hat{W} = \operatorname{Tr} \mathrm{e}^{-\beta(\hat{H}-\mu\hat{N})} = \sum_{\{n\}} \mathrm{e}^{-\beta(E_n-\mu N_n)} \qquad \text{with} \qquad N_n = \sum_{k=1}^{M} n_k \,, \tag{2.11}$$

where n is used, like in the following, as a multi index and whose entries n_k run over all the possible occupation numbers of a state, i.e. 0, 1 for fermions, and E_n denotes as before the many-body energies of the Hamiltonian $\hat{H}$. Here, the dependence of the partition function on temperature via the inverse temperature β was suppressed, in contrast to the dependence on the chemical potential in order to distinguish it from the quantity in the canonical ensemble later on. Thermodynamic properties such as the internal energy[1] U or the entropy $\mathcal{S}$ are then given by the derivatives of this function:

$$N_\mu = \beta^{-1}\frac{\partial \ln Z_\mu}{\partial \mu} \qquad \mathcal{S}_\mu = -k_{\mathrm{B}}\beta^2 \frac{\partial \beta^{-1} \ln Z_\mu}{\partial \beta} \tag{2.12}$$

$$U_\mu = \mu N_\mu - \frac{\partial \ln Z_\mu}{\partial \beta} \qquad C_\mu = k_{\mathrm{B}}\beta^2 \frac{\partial^2 \ln Z_\mu}{\partial \beta^2} \tag{2.13}$$

[1] To be precise, the internal energy $U\big(N\big((k_{\mathrm{B}}\beta)^{-1},\mu,\mathcal{V}\big),\mathcal{S}\big((k_{\mathrm{B}}\beta)^{-1},\mu,\mathcal{V}\big),\mathcal{V}\big)$ where $\mathcal{V}$ represents the volume given by the number of sites M for models like (2.3), is calculated above due to the dependencies of the partition function.

These relations can also be expressed in operator notation as

$$N_\mu = \langle \hat{N} \rangle_{\beta,\mu} \,, \quad \mathcal{S}_\mu = -k_\mathrm{B} Z_\mu \langle \ln \hat{W} \rangle_{\beta,\mu}, \tag{2.14}$$

$$U_\mu = \langle \hat{H} \rangle_{\beta,\mu} \,, \quad C_\mu = k_\mathrm{B} \beta^2 \Big[\langle \hat{H}^2 \rangle_{\beta,\mu} - \Big(\langle \hat{H} \rangle_{\beta,\mu} \Big)^2 \Big] \,, \tag{2.15}$$

where the thermodynamic expectation value of an operator $\hat{X}$ is defined as

$$\langle \hat{X} \rangle_{\beta,\mu} = Z_\mu^{-1} \operatorname{Tr}\Big(\hat{W} \hat{X} \Big) \,. \tag{2.16}$$

For a non-interacting system with M single-particle states the grand canonical partition function can be written as the product of the distributions of single particles:

$$Z_\mu = \sum_{n_1} \sum_{n_2} \cdots \sum_{n_M} \mathrm{e}^{-\beta \sum_{k=1}^{M} n_k (\varepsilon_k - \mu)} = \prod_{k=1}^{M} \sum_{n_1} \mathrm{e}^{-\beta n_1(\varepsilon_k - \mu)} = \prod_{k=1}^{M} Z_k \tag{2.17}$$

Thereby it could be seen, that even the zero point of the single-particle energies is arbitrary if the chemical potential is measured from the same point. Furthermore, in a fermionic system the occupation number n_1 of eigenstates can only be zero or unity as mentioned in the last section. Therefore defining the distribution of a single particle by the reciprocal of the Fermi function f:

$$Z_k = \sum_{n_1=0}^{1} \mathrm{e}^{-\beta n_1 (\varepsilon_k - \mu)} = 1 + \mathrm{e}^{-\beta(\varepsilon_k - \mu)} = \frac{1}{f\Big(-\beta(\varepsilon_k - \mu) \Big)} \tag{2.18}$$

Thus all quantities in (2.12) and (2.13) can easily be obtained. However, for a large system size M the product in (2.17) might be difficult to evaluate. This product becomes a sum if put in (2.12) or (2.13) due to the logarithmic dependence of the thermodynamic properties on the partition function. Therefore this sum is usually rewritten by the density of states ρ into an integral

$$\sum_k F(\varepsilon_k) = M \int_{-\infty}^{\infty} \rho(\varepsilon)\, F(\varepsilon)\, \mathrm{d}\varepsilon \qquad \text{with} \qquad \rho(\varepsilon) = \frac{1}{M} \sum_k \delta(\varepsilon - \varepsilon_k) \,. \tag{2.19}$$

This description is especially beneficial in the thermodynamic limit, where the system size M tends to infinity but a constant density is assumed. Thereby the sum in the definition of the density of states becomes an integral with a prefactor of $M/(2\pi)^d$, where d denotes the dimension, explaining the prefactor in the definition (2.19). For instance, this quantity of a d-dimensional system with the dispersion relation

$$\varepsilon_k = \frac{\hbar^2 k^2}{2m} \qquad \text{with} \qquad k \in \mathbb{R} \tag{2.20}$$

can be derived as

$$\rho(\varepsilon) = \frac{S_d\, (2m)^{d/2}}{2\,(2\pi\hbar)^d}\, \varepsilon^{d/2-1} \,, \tag{2.21}$$

where m describes the mass of the considered particles and S_d denotes the area of the unit sphere in d dimension, e.g. $S_1 = 2$, $S_2 = 2\pi$ or $S_3 = 4\pi$. While for a one-dimensional system this expression shows a square-root singularity at $\varepsilon = 0$ known as a Van-Hove singularity, it is constant for a two-dimensional system like the idealized one discussed in section 1.2.

The transfer from a grand canonical to a canonical ensemble is usually done by a Legendre transformation between the grand canonical potential $\Omega = -\beta^{-1} \ln Z_\mu$ and the free energy $F = -\beta^{-1} \ln Z_N$. Thereby, the dependence on the chemical potential μ changes to one on the fixed particle number N, i.e. $F(N) = \Omega\Big(\mu(N)\Big) + \mu(N)N$. Thus the needed task for this transformation is determining the chemical potential for the desired particle number. This leads to the challenge of inverting the particle number condition,

$$N_\mu/M = \int_{-\infty}^{\infty} \rho(\varepsilon)\, f\Big(\beta(\varepsilon - \mu)\Big)\, \mathrm{d}\varepsilon\,, \tag{2.22}$$

following from putting (2.18) in (2.12) and applying the transformation (2.19). The occurring integral can be found as a series in the polylogarithm function Li_{s+1}, where the order $s \in \mathbb{C}$ is given by the corresponding power in the expression of the density of states as a series of such powers (cf. appendix). However, the inversion of these functions can usually not be expressed as finite combinations of elementary functions. Therefore it is only possible to treat them in approximations or numerical evaluation.
The most famous of these approximations would probably be the Sommerfeld approximation. For this, the integral in (2.22) is expanded for low temperature by considering the deviation of the Fermi function from a step function. The result for a non-interacting three-dimensional system, which is described by the density of states in (2.21), would be a behavior which would be quadratic in temperature. This leads to a quadratically dependent chemical potential, too, and through similar derivation rules as in (2.12) and (2.13) to a linear specific heat:

$$\mu = \varepsilon_F - \varpi\, T^2 \qquad C_N = \gamma\, T + \mathcal{O}(T^3)\,, \tag{2.23}$$

where ε_F describes the Fermi energy (cf. Fig. 2.4) and ϖ and γ are material dependent coefficients. They are given for a three-dimensional system with (2.20) by

$$\varpi = \frac{\pi^2 {k_\mathrm{B}}^2}{12\varepsilon_F}, \qquad \gamma = \frac{\pi^2 {k_\mathrm{B}}^2}{2\varepsilon_F} N\,. \tag{2.24}$$

In the Fermi liquid theory of interacting systems these parameters get renormalized, but a linear behavior of the specific heat with respect to temperature still remains, in contrast to critical systems [71–73]. This result can be visualized by the use of the Fermi surface too (cf. Fig. 2.4). The temperature raises the energy of the fermions by $k_\mathrm{B}T$. However, since at zero temperature the particles occupy every state of the density of states below the Fermi energy only those with an energy around this energy scale contribute to the specific heat, leading to the system dependent parameter γ.

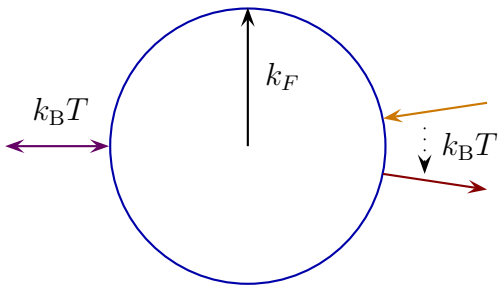

Figure 2.4: At zero temperature the states which are lowest in energy, are filled by the particles which have a wave vector smaller than k_F which corresponding energy is the Fermi energy ε_F. Since every state can be occupied only once, this leads to the Fermi surface separating occupied and empty states. At finite temperature excitations around this Fermi surface can happen with maximum energy $k_\mathrm{B}T$ (left). Therefore the scattering of two quasi-particles, which describe the excitations, can maximally transfer the same amount of energy (right).

Although with the above mentioned technique physical quantities usually needed can easily be obtained, numerical simulations are often limited to finite system sizes as will become clear later on. For such finite system sizes the quantities of the grand canonical system vary from the ones in the canonical ensemble. Nevertheless, the latter ones can still be calculated by the partition function but the sum in (2.11) has to be restricted to those states which obey the fixed particle number N. In addition the chemical potential will not appear:

$$Z_N = Z_{\mu=0}\Big|_{\text{particle number=N}} = \sum_{\{n\}} \mathrm{e}^{-\beta E_n}\Big|_{\text{particle number=N}} \tag{2.25}$$

The difference between both ensembles can already be seen at low temperatures. For both ensembles, the behavior for those temperatures is given by the first terms describing the many-body level spacing Δ between the ground state and the first excited states due to the finite system size in the corresponding ensemble:

$$Z = 1 + \mathrm{e}^{-\beta\Delta}\left(1 + \mathcal{O}(\mathrm{e}^{-\beta\delta})\right), \tag{2.26}$$

where δ denotes the level spacing between the first two excited states. The relation in (2.13) will then lead to a low temperature behavior of the specific heat familiar from insulators

$$C = k_\mathrm{B}\Delta^2\beta^2\,\mathrm{e}^{-\beta\Delta} + \mathcal{O}(\beta^2\,\mathrm{e}^{-2\beta\Delta}) + \mathcal{O}(\beta^2\,\mathrm{e}^{-\beta(\Delta+\delta)}). \tag{2.27}$$

Note that in a grand canonical system of non-interacting fermions the gap Δ is given by inserting an additional fermion into the system which occupies a state with the energy ε_{n_F+1}, where n_F denotes the highest occupied single-particle level in the ground state (cf. Fig. 2.5). In contrast, for a canonical system additional energy is necessary to release

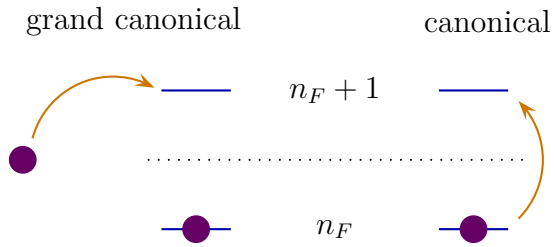

Figure 2.5: Illustration of the lowest energy excitation of grand canonical and canonical systems with finite size. In the former one lesser energy is needed to occupy the first excited state than in the latter one, since in this ensemble the particle of the highest occupied state has to be released first.

a fermion from its original state so that it can occupy the next higher one. Therefore the finite size gap Δ of a canonical system is larger than the one in the grand canonical system, resulting in different exponential increase of the specific heat at low temperatures (cf. Fig. 2.6).

The restriction to states which fulfill the particle number constraint in the case of the canonical ensemble can be treated exactly too. The constraint as formulated by Kronecker's delta can be dealt with by using its Fourier transformed representation:

$$Z_N = \sum_{\{n\}} \mathrm{e}^{-\beta \sum_k \varepsilon_k n_k} \; \delta_{N, \sum_k n_k} \tag{2.28}$$

$$= \frac{1}{M} \mathrm{Re} \sum_{p=1}^{M} \sum_{\{n\}} \mathrm{e}^{-\beta \sum_k \varepsilon_k n_k + 2\pi i p (\sum_k n_k - N)/M} \tag{2.29}$$

$$= \frac{1}{M} \mathrm{Re} \sum_{p=1}^{M} \mathrm{e}^{-2\pi i p N/M} \prod_k \sum_{n_k=0}^{1} \mathrm{e}^{-\beta \varepsilon_k n_k + 2\pi i p n_k/M} \tag{2.30}$$

Here, the periodicity of the Fourier transform was chosen as M since the maximal violation of the constraint will always be lower than that number for singly occupied states. From (2.30) the canonical partition function can be calculated from the grand canonical one using an imaginary chemical potential. This is similar to the Popov-Fedotov trick in the two-dimensional anti-ferromagnetic Heisenberg model, where such a chemical potential was used in order to constrain the local auxiliary-fermion-charge [74]. In the calculation above the problem was restricted to its real part which can easily be evaluated when using the complex logarithm after the sum over the occupation of one state is performed in (2.30):

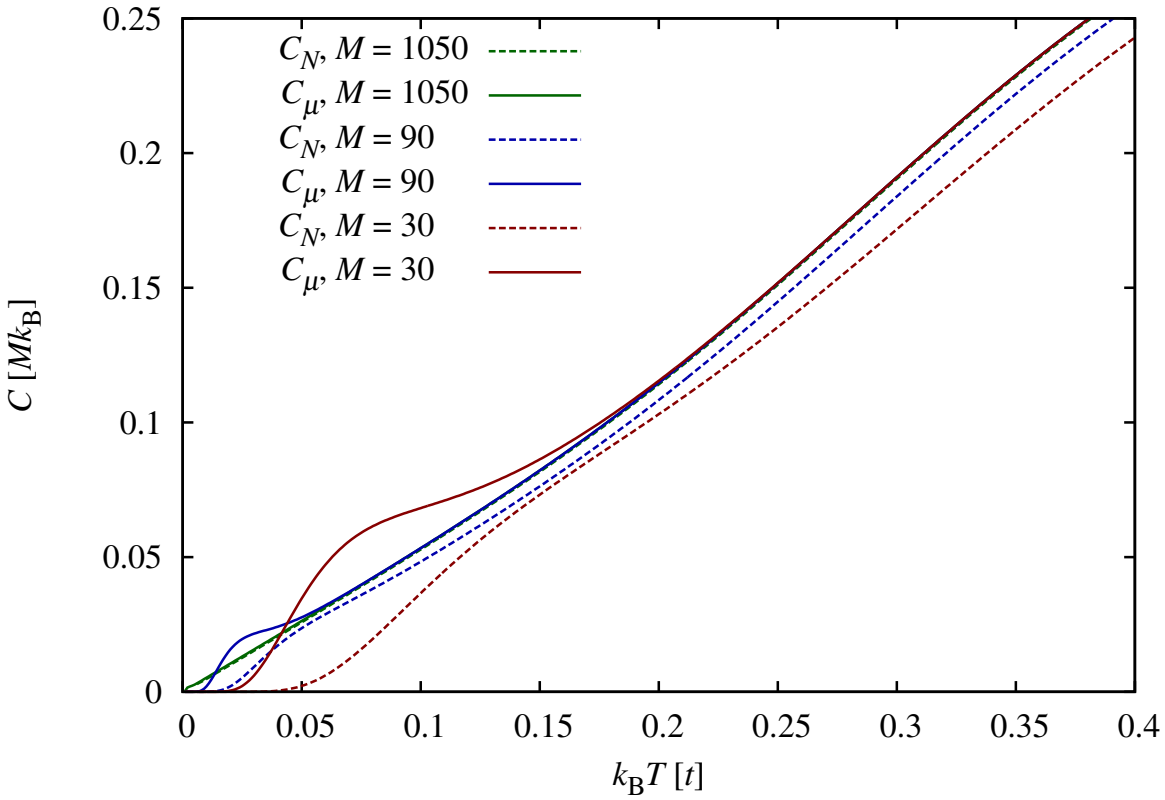

Figure 2.6: Comparison of the specific heat of a canonical C_N and a grand canonical system C_μ for different system sizes M as calculated by taking the derivatives of (2.33) and (2.17) with (2.18) according to (2.13) for the ring (2.3). The different gap Δ between the ground state and the first excited state of the grand canonical or canonical system causes the curves to approach the specific heat in the thermodynamic limit from upwards or from below. As seen, both curves for a system size of $M = 1050$ coincide in the diagram and therefore can be viewed as the one in the thermodynamic limit.

$$Z_N = \frac{1}{M} \operatorname{Re} \sum_{p=1}^{M} \mathrm{e}^{-2\pi i p N/M} \exp\left(\sum_k \ln\left(1 + \mathrm{e}^{-\beta\varepsilon_k + 2\pi i p/M}\right)\right) \tag{2.31}$$

$$= \frac{1}{M} \sum_{p=1}^{M} \cos\left(2\pi p N/M - \sum_k \arctan\left[\frac{\sin(2\pi p/M)}{\mathrm{e}^{\beta\varepsilon_k} + \cos(2\pi p/M)}\right]\right) \cdot$$

$$\cdot \prod_k \sqrt{1 + \mathrm{e}^{-2\beta\varepsilon_k} + 2\,\mathrm{e}^{-\beta\varepsilon_k} \cos(2\pi p/M)} \tag{2.32}$$

The $p = M$ term in this expression resembles the grand canonical result with vanishing chemical potential. In using further the symmetry of this expression under the transforma-

tion $p \to M-p$ the relative difference between the canonical and grand canonical partition function, with vanishing chemical potential, is obtained

$$\begin{aligned}\frac{Z_N - Z_{\mu=0}}{Z_{\mu=0}} &= (-1)^N \prod_k \tanh(\beta\varepsilon_k/2)\Big|_{M \text{ even}} \\ &\quad + 2 \sum_{p=1}^{\lfloor (M-1)/2 \rfloor} \cos\left(2\pi p N/M - \sum_k \arctan\left[\frac{\sin(2\pi p/M)}{\mathrm{e}^{\beta\varepsilon_k} + \cos(2\pi p/M)}\right]\right) \cdot \\ &\quad \cdot \prod_k \sqrt{1 + \frac{\cos(2\pi p/M) - 1}{\cosh(\beta\varepsilon_k) + 1}}\,, \end{aligned} \tag{2.33}$$

which turns out to be numerically stable even for low temperatures (cf. Fig. 2.6). Since the sum has been reduced by adding the p and $M-p$ values, a term appears when the sum contains an odd number of terms. This resulting first term in the expression above might resemble a qualitative difference between and even and odd number of particles. For the ground state of a one-dimensional system such a qualitative difference is known by the application of Legett's theorem [75] to the ring (2.3) which has been derived for polarized systems as well [76].

The different finite size gaps of a canonical and a grand canonical system implicates another interesting feature which can be exemplified using the above formula (2.33) (cf. Fig. 2.6). For $M = 2$ the grand canonical system of (2.3) resembles the two-level system where a Schottky-anomaly is known in the specific heat. When increasing the system size an additional peak emerges from this anomaly since the exponential increase due to the finite size gap (2.27) does not match the one of the original anomaly. Between these features a linear region appears, which extends to vanishing temperature in the thermodynamic limit, where the position of the finite size peak is suppressed. This result is also known from conformal field theory from which the slope as defined in (2.23) is given by [77, 78]

$$\gamma = \frac{\pi {k_\mathrm{B}}^2}{6t} M\,. \tag{2.34}$$

Furthermore, the approach of the canonical system towards the thermodynamic limit shows a slightly different behavior due to the above discussed different finite size gaps (cf. discussion after (2.27)). Therefore the linear region, when extrapolated to vanishing specific heat, does not intersect the origin, but the intersection point moves towards it if the system size is increased. In this sense, the grand canonical version can be regarded as resembling the thermodynamic limit better than the canonical one. However, in numerical simulations the canonical version might be more easily accessible since the restriction to the states of a canonical system reduces the amount of memory needed as will be further discussed in section 3.1.

2.3 Transport Properties

Within Drude transport theory [79] the electrical conductivity is given by

$$\sigma = \frac{q^2 N \tau}{m \mathcal{V}} \,, \tag{2.35}$$

where q and m denote the charge and mass of the conducting particles and $\mathcal{V}$ represents the volume while τ is the mean time between two scattering events, i.e. the time those particle remain in the same momentum state. Since for non-interacting fermions the particles always remain in their initial momentum state this time τ would be given by external processes, like impurity scattering [43]. However, for interacting fermions the finite lifetime might be shorter than the times of these external processes and will therefore cause significant changes in the conductivity of a lattice. The rate of the decay of the quasi-particles is usually given in second order in the interaction strength by the imaginary part of the Feynman diagram

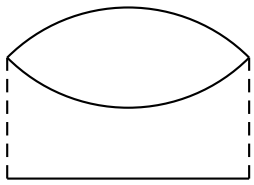

but can be estimated by Fermi's golden rule when considering the scattering of two quasi-particle excitations above the Fermi surface (cf. Fig. 2.4) [80]. In this formula, the transition probability would be determined by the product of the processes that the one quasi-particle can increase its energy and that the other one can decrease its by the same amount. Both processes are proportional to the maximal transfered energy $\Delta\varepsilon$. At finite temperature, this energy is given by the thermal energy $k_\mathrm{B}T$. Since the determined transition probability is proportional to the inverse life time, the electrical contribution to the reciprocal conductivity would be quadratic with temperature

$$\sigma^{-1} \propto \tau^{-1} \propto \Delta\varepsilon^2 \propto T^2 \,, \tag{2.36}$$

as was seen experimentally (cf. Fig. 1.2). Furthermore, a universal ratio A/γ^2 was found in experiments where A denotes the quadratic coefficient of the resistivity with respect to temperature, i.e. the proportionality constant of (2.36), and γ was defined in (2.23). Even heavy fermion compounds [81] as well as metallic oxides [82–84] seem to obey this Kadowaki-Woods relation although with a different value than simple metals due to many-body correlations [85] (cf. Fig. 2.7). This behavior is in contrast to the known activated behavior of an insulator [6]:

$$\sigma^{-1} \propto \mathcal{V}/N \sim \mathrm{e}^{\beta\Delta/2} \,, \tag{2.37}$$

where Δ denotes again the gap of the insulator, which was seen for one sample in the inset of Fig. 1.3.

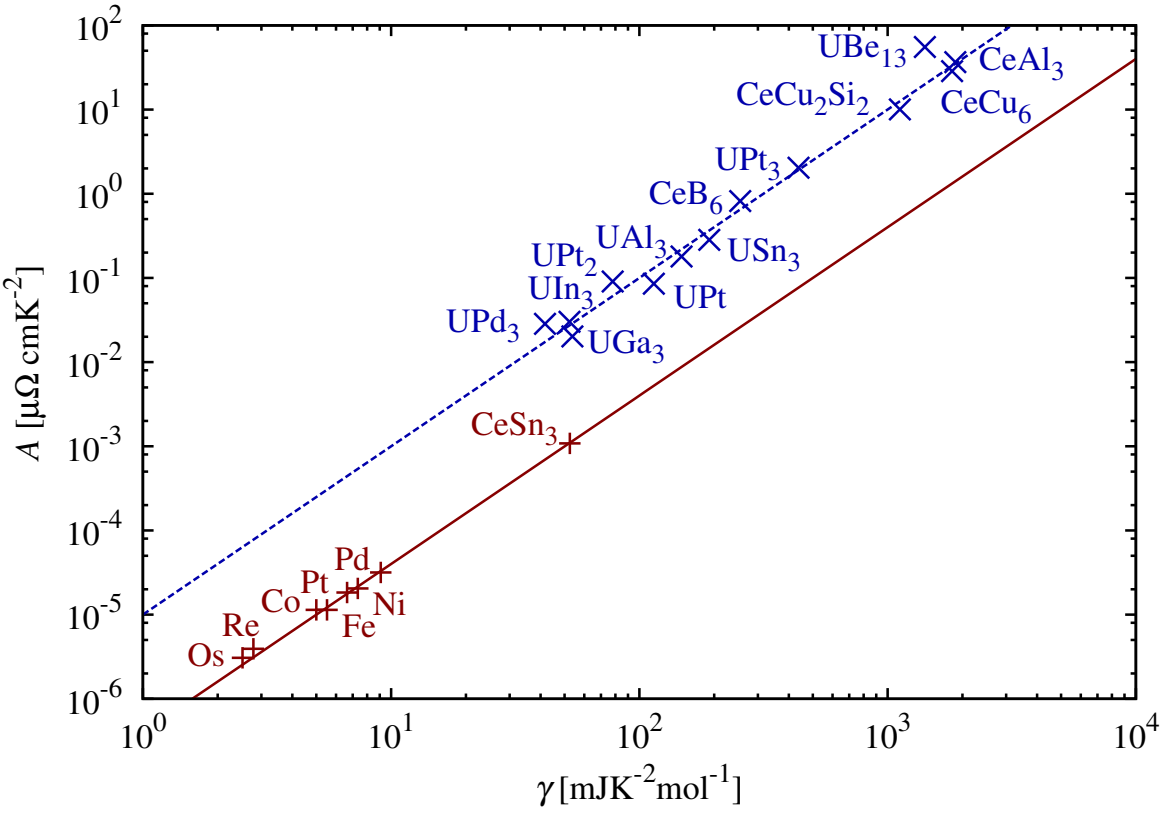

Figure 2.7: Quadratic coefficient of the resistivity against the linear one of the specific heat according to [82]. Transition metals follow the Kadowaki-Woods ratio $A/\gamma^2 = 4 \cdot 10^{-7}\,\mu\Omega\mathrm{cm}/(\mathrm{mJ/Kmol})^2$ (solid line) while heavy fermion compounds exhibit the slightly larger value of $A/\gamma^2 = 1 \cdot 10^{-5}\,\mu\Omega\mathrm{cm}/(\mathrm{mJ/Kmol})^2$ (dashed line).

Another quantity mentioned previously in (1.1) important for practical applications is the thermopower. This quantity is defined as the voltage drop ΔV resulting from a temperature gradient ΔT where no particle current or concentration gradients are present. It can therefore be expressed as the ratio of correlation functions [44]:

$$S = \frac{\Delta V}{\Delta T} = \frac{1}{q_e T} \frac{\langle \hat{j}_Q \hat{j}_n \rangle}{\langle \hat{j}_n \hat{j}_n \rangle} \tag{2.38}$$

$$= \frac{1}{q_e T} \left(\frac{\langle \hat{j}_E \hat{j}_n \rangle}{\langle \hat{j}_n \hat{j}_n \rangle} - \mu \right) \tag{2.39}$$

$$= \frac{1}{q_e T} \big(E_0(T) - \mu(T) \big) , \tag{2.40}$$

where the first law of thermodynamics was used to obtain (2.39) and q_e denotes the negative charge of the electron while $\hat{j}_n$, $\hat{j}_Q$ and $\hat{j}_E$ describes the particle, heat and energy current operator respectively. In the last step the thermopower was decomposed into a transport property described by the function $E_0(T)$ and a term determined from the equilibrium situation given by the chemical potential. Nevertheless, the actual value of these two terms are explicitly dependent on the zero point of the single-particle energies. When considering a specific temperature T the expression in the brackets of (2.40) represents the chemical potential when the single-particle energies are shifted by $E_0(T)$. Therefore the actual value of the thermopower for this specific temperature is fully determined by the equilibrium situation but in a reference frame in which the correlation function $\langle \hat{j}_E \hat{j}_n \rangle$ vanishes. Although for the full temperature dependence of the shift E_0 transport theory is still needed, it can be estimated in special cases.

In the limit of very high temperatures, Chaikin and Beni argued that the transport function $E_0(T)$ takes a constant value within Kubo formalism [86]. They even determined it in the atomic limit by stochastic arguments, and this convenient formula became known as the Heikes formula

$$S = \frac{k_\mathrm{B}}{q_e} \ln \frac{1-\mathrm{x}}{\mathrm{x}}, \tag{2.41}$$

where x denotes the doping. The doping dependence of this formula was applied to many systems although it needed to be modified in case of degenerate systems or in the presence of an interaction scale which is even much greater than the temperature scale [86–93]. However, as neither the temperature nor the dimensionality of the system enter these formulas, using them might be questionable, especially if the thermopower decreases when increasing the temperature above the application region where it had seemed to saturate [92, 93]. Applying these formulas to the delafossites discussed in section 1.1 would raise doubts, too, due to the observed linear behavior of the thermopower in temperature, which was defined as the one of the AFL. Therefore formulas for the thermopowers depending on temperature at intermediate temperature ranges are needed.

When considering a single resonant level, e.g. in molecular junctions, another expression can be derived in case the coupling to ballistic leads is weak and temperature independent. If such a level is in resonance, i.e. at the same energy as the chemical potentials of both leads, a temperature gradient would not lead to a current I due to the symmetry of the model. Therefore the thermopower (2.38) would vanish. Thus in the following will be considered the opposite situation where the level would be far away from the chemical potentials. In this limit, the Lorentzian transmission $\mathcal{T}(\varepsilon)$ for the non-resonant level model [94] might be expanded in terms of the broadening Γ of the level

$$\mathcal{T}(\varepsilon) = \Gamma\, \delta(\varepsilon - \varepsilon_0) + \mathcal{O}(\Gamma^2), \tag{2.42}$$

where ε_0 denotes the energy of the level and the normalization at zero temperature was taken into account. The Landauer formula [95, 96] for the tunneling current I gives for

such a transmission in the spinless case

$$I = \frac{q_e}{\pi\hbar}\int \mathcal{T}(\varepsilon)\left[f\Big(\beta_L(\varepsilon-\mu_L)\Big) - f\Big(\beta_R(\varepsilon-\mu_R)\Big)\right]\mathrm{d}\varepsilon \tag{2.43}$$

$$= \frac{q_e\Gamma}{\pi\hbar}\left[f\Big(\beta_L(\varepsilon_0-\mu_L)\Big) - f\Big(\beta_R(\varepsilon_0-\mu_R)\Big)\right], \tag{2.44}$$

where $\hbar$ is the reduced Planck constant and the inverse temperature β as well as the chemical potential μ in the left and right lead where distinguished by the indices L and R. For the condition that no current flows $I = 0$, which was asked for in the definition of the thermopower, the Fermi functions and therefore their arguments have to be equal

$$(\varepsilon_0 - \mu_R)\, k_\mathrm{B} T_L = k_\mathrm{B} T_R\, (\varepsilon_0 - \mu_L)\,. \tag{2.45}$$

In expressing therein the quantities of the left and right environment by their small differences $q_e\Delta V$ and ΔT as well as the averaged temperature T and chemical potential μ previously used, the thermopower is obtained according to (2.38) as

$$S = \frac{1}{q_e T}\Big(\varepsilon_0 - \mu\Big)\,. \tag{2.46}$$

Therefore the $E_0(T)$ function assumes the constant position of the considered level ε_0. Furthermore, the same relation can be derived when the transmission is governed by thermal processes [97].

Motivated by the results of these formulas the temperature independent correlation functions ratio approximation (TICR) approximates the transport term of the thermopower as a constant $E_0(T) \approx E_0$ in a certain temperature region [98]:

$$S(T) \approx \frac{1}{q_e T}\Big(E_0 - \mu(T)\Big) \tag{2.47}$$

Thereby, the freedom of choice for the zero point of the single-particle energies is preserved. Furthermore, regarding the constant E_0 as an independent parameter may include some contributions of electron-electron scattering or electron-phonon scattering. The latter one can be treated approximately as well. However, a detailed study on a cubic lattice [99, 100] pointed out a linear behavior of the thermopower with respect to temperature in the low and high temperature limit, but without an offset. In addition, the obtained features at intermediate temperatures of this calculation get smeared over for large Debye temperatures, which were reported for several delafossites [101–103]. Therefore, this work will only consider the purely electronic part of the thermopower while the effects of the phonons will merely be accounted by the E_0 parameter.

Of course, such a determination of a transport property by results known from the system at equilibrium will not always be possible. For instance, while this approximation might work well for high temperatures where the chemical potential has left the conduction band and this band might seem as a single level as in (2.46), it will fail at low temperature:

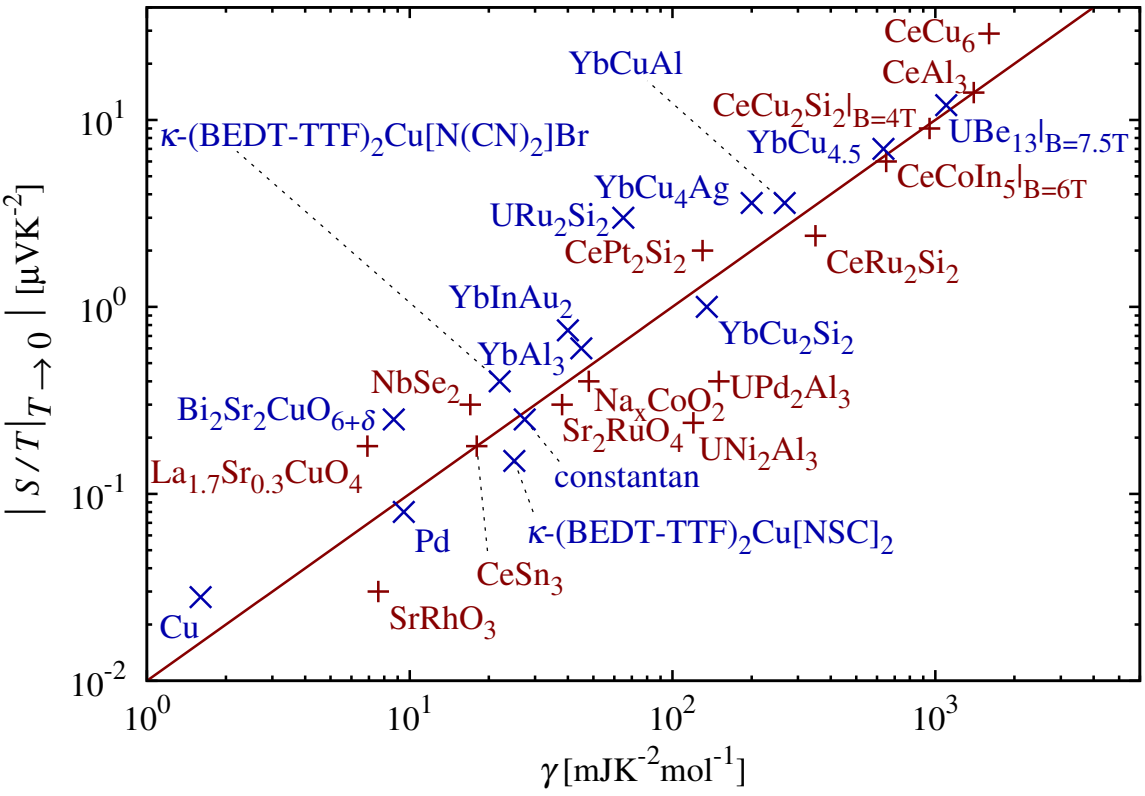

Figure 2.8: Absolute value of the linear coefficient of the thermopower against the one of the specific heat in the low temperature limit from data collected in [104]. The different point types represent different sign of the thermopower.

This can be seen when looking at the thermopower of a metal. In this case this quantity vanishes at zero temperature. This means that the TICR constant E_0 takes the value of the Fermi energy:

$$E_0 = \varepsilon_F \tag{2.48}$$

With the chemical potential from (2.24) this gives a linear thermopower

$$S_{\mathrm{TICR}} = -\frac{\pi^2 {k_\mathrm{B}}^2}{12 q_e \varepsilon_F} T\,. \tag{2.49}$$

However, the temperature dependence of the transport function $E_0(T)$ is still important: Within the framework of Boltzmann transport theory a linear thermopower in Fermi liquid theory could be derived [104]

$$S = \frac{\pi^2 {k_\mathrm{B}}^2}{2 q_e} \frac{T}{\varepsilon_F} \left(1 + \frac{2}{3}\xi\right)\,. \tag{2.50}$$

Thereby, the coefficients of non-interacting fermions in three dimension with the common dispersion relation (2.20) are renormalized in the Fermi liquid by the correlation length ξ. In comparing this result to the one previously derived from the TICR (2.50) the quadratic term of the $E_0(T)$ function seems to contribute to the thermopower by three times the amount of the chemical potential at low temperatures. Also in other models such deviation at low temperatures have been observed by the use of a finite frequency formulation of the thermopower [105–109].

Surprisingly, when comparing the thermopower (2.50) to the specific heat (2.23) another universal ratio $\mathfrak{q}$ is found for a non-interacting fermionic system:

$$\mathfrak{q} = -\frac{S\, q_e}{T\, \gamma} = -\frac{1}{N} \tag{2.51}$$

Furthermore, it could be shown that this ratio remains even if scattering processes are considered [110]. Therefore, this constant ratio has been found experimentally, too (cf. Fig. 2.8).

Chapter 3

Numerical Evaluation at Finite Temperatures

In this chapter, the numerical evaluation of the expectation values (2.14) and (2.15) is discussed. At present, these can be numerically determined using techniques like density functional theory [111] or quantum monte carlo techniques [112, 113]. However, this work will be concerned about the implementation of a temperature scale into another technique, namely the density matrix renormalization group method. While this technique can be applied to any fermionic system formulated in second quantization without any further assumptions, it is usually efficient only in one-dimensional systems. Even so, the application to systems with higher dimension is still part of ongoing research [114–116].

Due to the two-dimensionality of the delafossites, this method will therefore be applied to the model introduced in (2.3). Furthermore, owing to the question of efficiently implementing a temperature scale, the thermopower is not yet accessible by this approach. This question is successfully addressed for a system with weak interaction strengths in section 3.5, and in section 3.6 a general scope is presented. Before this the numerical approach by (iterative) diagonalization is introduced in the following section 3.1, as well as the density matrix renormalization group (DMRG) technique in section 3.2. The final section 3.7 will summarize the results.

3.1 Exact Diagonalization

Often, a physical system is reduced to only a few key features. For instance, in the tight binding approximation used in section 2.1 the motion of a particle like an electron is restricted to the hopping between lattice sites. Furthermore, the infinitely many orbitals of an atom at a lattice point in the considered crystal is usually modeled by taking only a few of them. This leads to a finite number of states for such systems which can be represented as vectors in a Hilbert space $\mathcal{H}$ with finite dimension. The physical quantities, which are represented by quantum mechanical operators, are then described as matrices

in this space. Finding all excited states of the Hamiltonian $\hat{H}$ therefore reduces to the problem of diagonalizing the Hamilton matrix H.

With modern computers, this problem can easily be solved for small systems, i.e. a small number of lattice points and only a few orbitals per site. However, on increasing the system size the Hilbert space $\mathcal{H}$ grows very fast. For instance, while for a canonical system of $N = 5$ spinless fermions distributed on $M = 10$ singly occupied sites only 252 many-body states have to be considered, for twice the number of particles and sites more than 10^5 states need to be determined. This leads to a total cost of memory up to 273 GB (for the storage of a fully occupied Hamilton matrix in double precision). Of course, this amount can be reduced by considering more symmetries of the system, but the scaling to larger systems still remains that drastic. Therefore means have to be developed to reduce the Hilbert space $\mathcal{H}$ during the calculation to only those states, which are important for the actual quantity one is interested in.

Since often the attention is focused on ground state properties, the method has been extended to include iterative techniques. An important role is played by those using Krylov subspaces $\mathcal{K}_n$. With each iteration n, these subspaces cover a growing part of the Hilbert space $\mathcal{H}$. This allows one to save memory if the iterating process is stopped at a given tolerance of the desired quantity. The subspaces $\mathcal{K}_n$ are build as the linear span of those vectors, which are generated from an initial vector $|i\rangle$ by applying the Hamilton matrix H multiple times:

$$\mathcal{K}_n = \left[|i\rangle, H|i\rangle, H^2|i\rangle, \ldots, H^n|i\rangle\right] \tag{3.1}$$

The state generated from the initial vector $|i\rangle$, which is usually chosen randomly, would then tend towards the ground state of the Hamiltonian, providing it has a finite overlap with this state. In addition, the Lanczos algorithm [117] orthonormalizes these vectors as they are generated, leading to a basis of this subspace

$$\left\{ |m\rangle = \left(H|i\rangle - \sum_{p<m} \langle m|H|i\rangle \, |m\rangle \right) / \mathcal{N} \,\middle|\, m = 1, 2, \ldots, n \right\}, \tag{3.2}$$

where $\mathcal{N}$ is chosen so that $\langle m|m\rangle = 1$. This leads to a representation of the Hamiltonian as a trigonal matrix which is easily diagonalized.

However, Davidson [118] showed that a faster convergence is obtained, if a so-called preconditioner $\mathcal{A}$ is used. His algorithm can be expressed by considering the eigenvectors $|n_k\rangle$ and eigenvalues $\lambda_{n,k}$ of the Hamilton matrix $H_\mathcal{K}$ projected to the previous Krylov space of the former iteration $\mathcal{K}_n$. Thereby, the new basis vector of the Krylov space for the subsequent iteration $\mathcal{K}_{n+1}$ is given by the component of

$$[\mathcal{A} - \lambda_{n,k}\mathbb{1}_\mathcal{H}]^{-1}(H - \lambda_{n,k}\mathbb{1}_\mathcal{H})|n_k\rangle_\mathcal{H} \tag{3.3}$$

orthogonal to the previous ones. For the practical algorithm, the eigenvector $|n_k\rangle$ has to be transformed from a basis representation of the Krylov space (3.1) (where only n numbers

are necessary to identify a state) to vectors lying in the whole Hilbert space $\mathcal{H}$. This transformation is usually shifted into the operator in round brackets. That operator determines the residual vector, i.e. the error vector of the generated state to the actual k-th eigenstate of the Hamilton matrix. In order to assure faster convergence, the additional operator given by the square brackets in (3.3) is applied leading to the correction vector. Preferably, the preconditioner $\mathcal{A}$ would be the full Hamilton matrix, so that this process would give the true eigenstate after one step. However, inverting the full Hamilton matrix would be another tough issue. Therefore, the matrix $\mathcal{A}$ denotes an approximation to the original Hamilton matrix which is easy to invert. For instance, for $\mathcal{A} = \mathbb{1}$ again the Lanczos algorithm is obtained, while in the original Davidson algorithm the matrix containing only the diagonal elements of the Hamilton matrix is used. Nevertheless, more advanced algorithms, like the Jacobi-Davidson one [119], usually consider more sophisticated preconditioners.

While the iterative techniques reduce greatly the amount of memory needed to obtain and store the results, building up the system still requires a lot of resources. If only non-interacting particles are concerned an $M \times M$-matrix is sufficient. However, for interacting particles the Hamilton matrix has to be build in the many-body basis as discussed in section 2.1, leading again to memory problems. To overcome this difficulty, techniques have been developed using the renormalization group.

3.2 The Density Matrix Renormalization Group

In the year 1971, Wilson introduced renormalization group theory to second-order phase transitions and critical phenomenon, and was by this mean able to solve the Kondo problem [120, 121]. In these problems correlations appear on various energy scales, leading to the failure of perturbation theory. The main idea of renormalization group theory is now to tackle the physical problem in steps, one for each scale. By renormalizing system parameters, the model at a larger scale is then mapped onto one at a smaller scale. However, this reduction of used basis states in order to describe the system still needs a clear separation of energy scales for the numerical renormalization group (NRG). In contrast, transport functions, boundary conditions or interactions in a tight binding model require representations other than the one given by the lowest eigenfunctions of the Hamiltonian as used in NRG. In order to find targets better suited for a given system, the density matrix renormalization group (DMRG) method was introduced [122–126].

This method already assumes that the considered system is part of a much larger structure, called the superblock C. Hence it distinguishes between the system A and an environment B. Furthermore, it searches for the most probable state in the system A with respect to the superblock C which resembles the ground state. Such a search was addressed in section 2.2 by acquiring the statistical operator in (2.10). It will be processed in this framework as follows (cf. Fig. 3.1):

By iterative diagonalization, e.g. by the Jacobi-Davidson algorithm as in the calculation below, the ground state $|\Psi_C\rangle$ of the superblock C is obtained. However, in general this

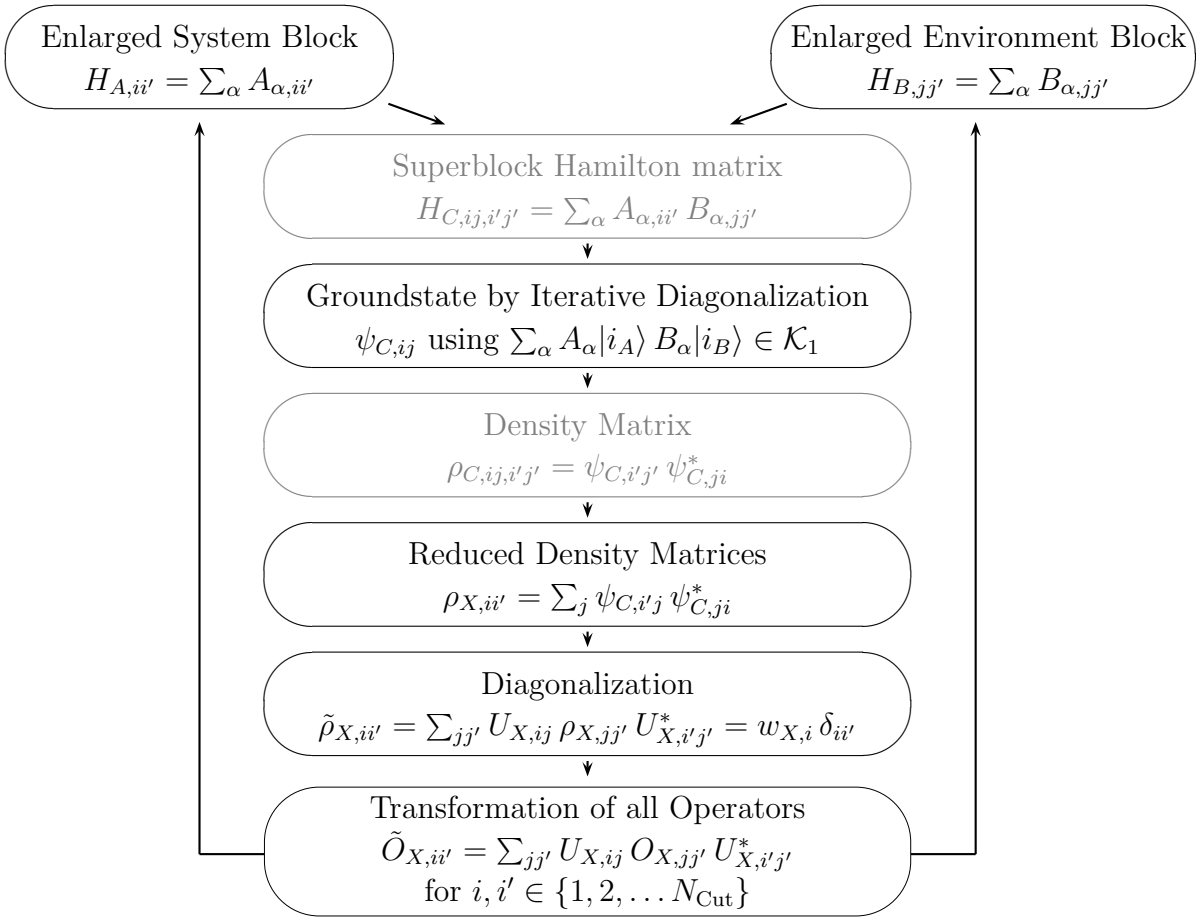

Figure 3.1: Reduction scheme of the DMRG method: The operators which construct the Hamilton matrix of the system A and environment block B are used to generate the one in the superblock C. However, this Hamilton matrix as well as the density operator of the superblock does not need to be stored (gray) since only the action of a state decomposed as a tensor product from the parts of the system and environment block (denoted by the double index ij) has to be calculated in order to find the ground state by iterative diagonalization routines. From it the reduced density matrix is constructed, its lowest eigenstates are determined and the reduction transformation is obtained for each block (if no symmetries are considered).

vector will resemble an entanglement between the system A and the environment B. This means that the system can not only be in a pure state, described by a single wave function, but in a mixed state, characterized by a density matrix ρ_A, too. This density matrix is obtained from the one of the superblock,

$$\rho_C = |\Psi_C\rangle\langle\Psi_C| \,, \tag{3.4}$$

by tracing out the degrees of freedom of the environment B:

$$\rho_A = \mathrm{Tr}_B\, \rho_C = \sum_\alpha w_\alpha |\alpha\rangle\langle\alpha| \tag{3.5}$$

Here, the reduced density matrix is expressed by its ordered eigenvalues $w_\alpha \leq w_{\alpha-1}$ and eigenvectors $|\alpha\rangle$, which span the Hilbert space $\mathcal{H}_A$ of the system A. In general, multiple eigenvectors are necessary describing the entanglement of the system. However, often, especially in one-dimensional systems, the ordered eigenvalues w_α decay rapidly. Therefore the ground state of the system A may be approximated by taking only the first N_{Cut} terms of the sum in (3.5), e.g. $N_{\mathrm{Cut}} = 800$ in the following calculation. The validity of this approximation can be checked during this procedure by confirming that the sum of the discarded weights $\sum_{\alpha>N_{Cut}} w_\alpha$ or the discarded entropy,

$$\mathcal{S}_{\mathrm{disc}} = -\sum_{\alpha>N_{\mathrm{Cut}}} w_\alpha \, \ln w_\alpha \,, \tag{3.6}$$

is negligible. While in statistical physics the weights w_α are interpreted as probabilities of finding the most probable state in the system A as mentioned previously, it can also be shown, that in this case the approximation represents the best way to project the dimension of the Hilbert space $\mathcal{H}_A$ of the system A to another one with dimension N_{Cut}, in the sense of a least-squares minimization of the differences between the exact ground state of the system and the approximated one [123].

With this reduction scheme it is possible to increase the size of the superblock. At the beginning of the process of achieving this goal a sufficiently small number M_A and M_B of the first sites as well as of the last sites are diagonalized exactly.[1] These are forming the initial system A and environment block B (cf. Fig. 3.2). Afterwards, a neighboring site is attached to each block. These sites are also connected forming the link between the system and environment. Together, the increased blocks construct the superblock C, i.e. the new basis vectors are composed by

$$|A\rangle \otimes |\sigma\rangle \otimes |\tau\rangle \otimes |B\rangle \,, \tag{3.7}$$

where $|A\rangle$ and $|B\rangle$ lie in the Hilbert space of blocks A and B, and $|\sigma\rangle$ and $|\tau\rangle$ represent basis vectors of those of the additional sites. This enables the determination of the ground

[1] If no order is given in the structure, like if periodic boundary conditions are applied, an arbitrary cut has to be chosen.

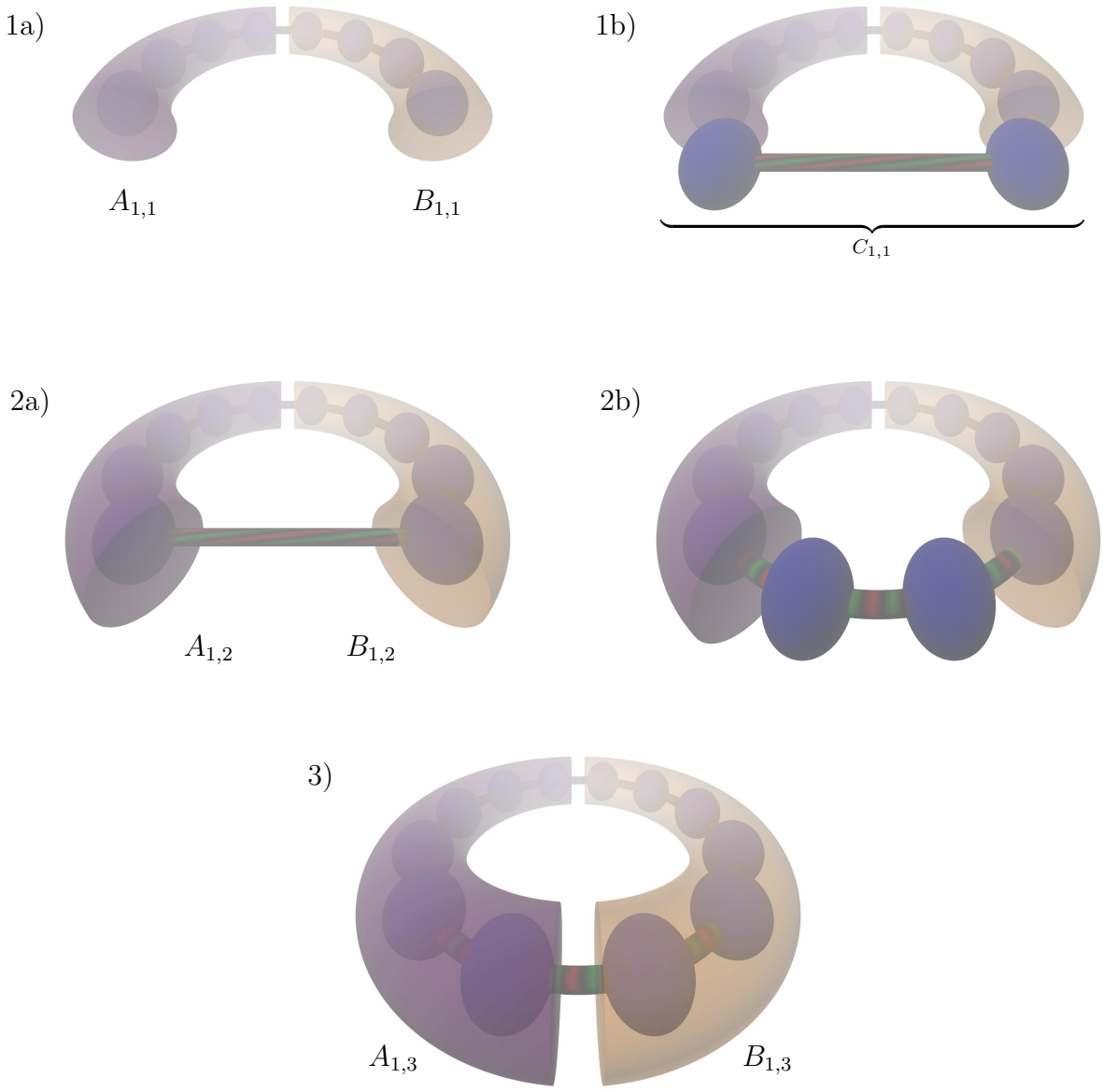

Figure 3.2: In the infinite system algorithm of the DMRG the structure is successively built up by adding one site to both the system A and the environment block B. The states of both blocks form the basis of the Hilbert space of the superblock C at each step. The representation of each step, distinguished here by the indices, are stored for later purpose.

state in the superblock C which permits the evaluation of quantum-mechanical expectation values of various operators. In addition, the density matrix of the system block and similarly that of the environment can be constructed from this state as described above. The projection of the states to the subspace given by only the N_{Cut} states with the highest eigenvalues in the density matrix leads therefore to the reduction of the Hilbert space for each block. This transformation of the basis states and the successive truncation to the subspace with reduced dimension have to be applied to every operator which is of interest. Subsequently, both blocks are further enlarged, leading to a continuous increase of the size of the superblock.

Despite that, this renormalization procedure often converges only very poorly. A reason for that can be seen in (2.33): In increasing the system size oscillating behavior typically occurs [127]. Therefore one should question a blind extrapolation to infinite system sizes. Furthermore, if the system is not totally uniform the procedure involving the addition of only one site might choose ill-advised states since the further structure of the system is not known. Thus the method scales also badly with the number N_{Cut} of states kept in this case [128]. Since increasing this number requires soon a huge amount of memory it is more useful to think of the previous infinite system algorithm as a process to generate an initial guess for the ground state of the system with a particular size. In the following finite system algorithm, where the size of the superblock remains fixed, this guess is improved by shifting the border between the system and environment block through the superblock (cf. Fig. 3.3). Therefore the system block increases while the environment block decreases. When the environment block can be treated exactly, the role of system and environment is interchanged reversing the direction of the shift. This sweeping through the superblock is repeated multiple times. After a few of those sweeps convergence is often obtained for a specific system size and the final expectation values can be determined by the entries of the operators in the space of the superblock C. In comparing different system sizes a trend towards the thermodynamic limit can then be determined.

However, achieving convergence in the DMRG algorithm is usually better if hard wall boundary conditions, i.e. the superblock ends sharply on the left and right side, are applied than if periodic boundary conditions are used (cf. Fig. 3.4). As mentioned in the previous footnote, one of the reasons for this can be found by the arbitrary cut which has to be introduced for periodic boundary conditions. Therefore the DMRG is better suited for hard wall boundary conditions. Furthermore, a deepened understanding could be obtained when the DMRG was formulated as an optimization in the spaces formed by matrix product states [129, 130]. While for strict one-dimensional systems with hard wall boundary conditions usually one of these states represents the ground state, for periodic boundary conditions of a system with higher dimension a different state might be searched for. Thus quantum information theory could propose a better suited algorithm which generalizes the DMRG to tensor networks [131, 132]. However, these techniques have to operate with matrices which are not sparsely occupied. Since this means a strong increase of required memory the DMRG algorithm is often used even for periodic boundary conditions as in the following study.

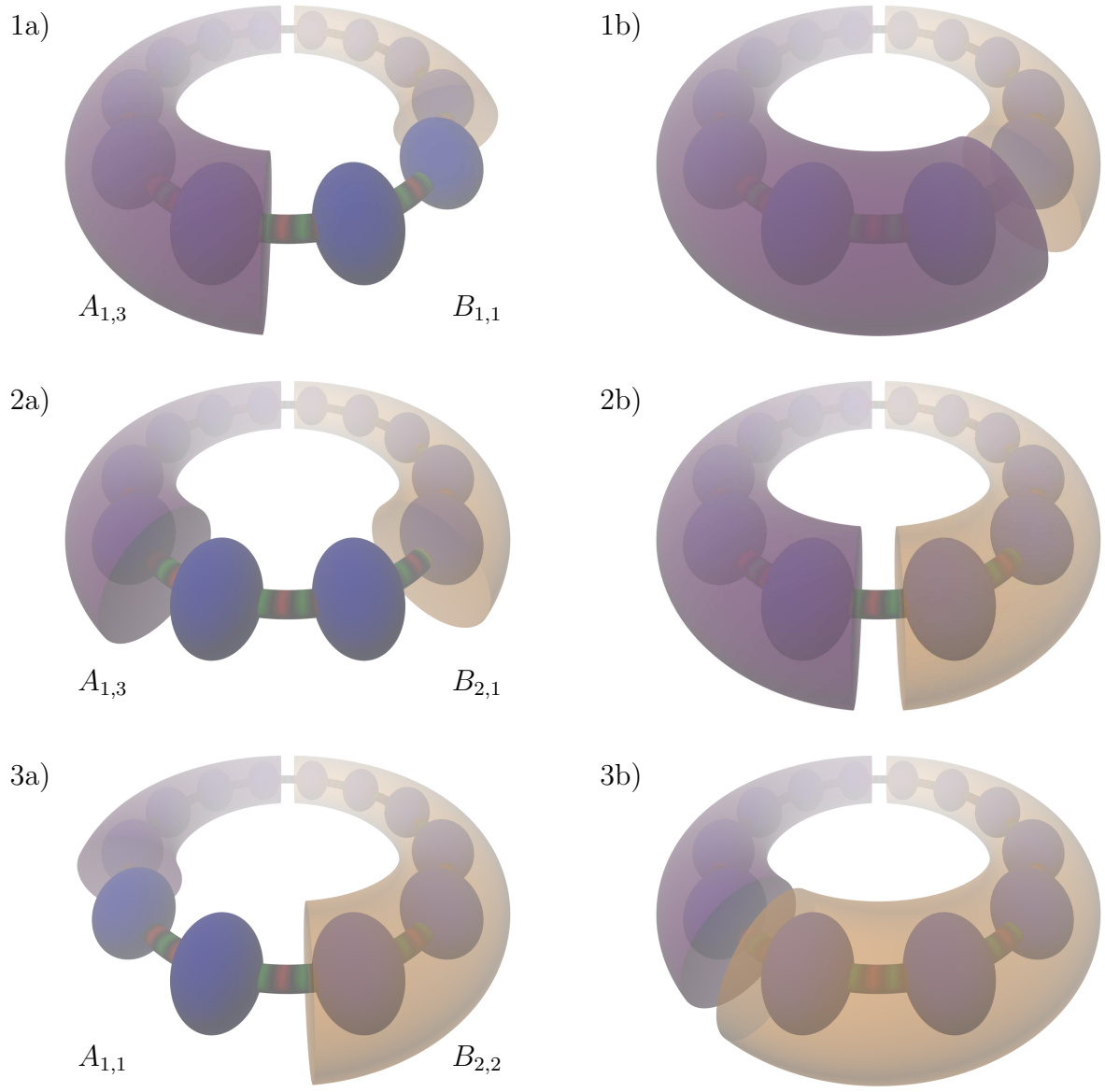

Figure 3.3: In the finite system algorithm of the DMRG the size of the superblock C stays fixed. Instead, the size of the system block is enlarged by decreasing the size of the environment block. Once the maximum size is obtained the role of the system and environment block interchange (1b). The labels A and B refer to the original distinction of the system and environment block while their indices represent the number of the sweep and step therein from which the basis states are recalled from memory according to Fig. 3.2.

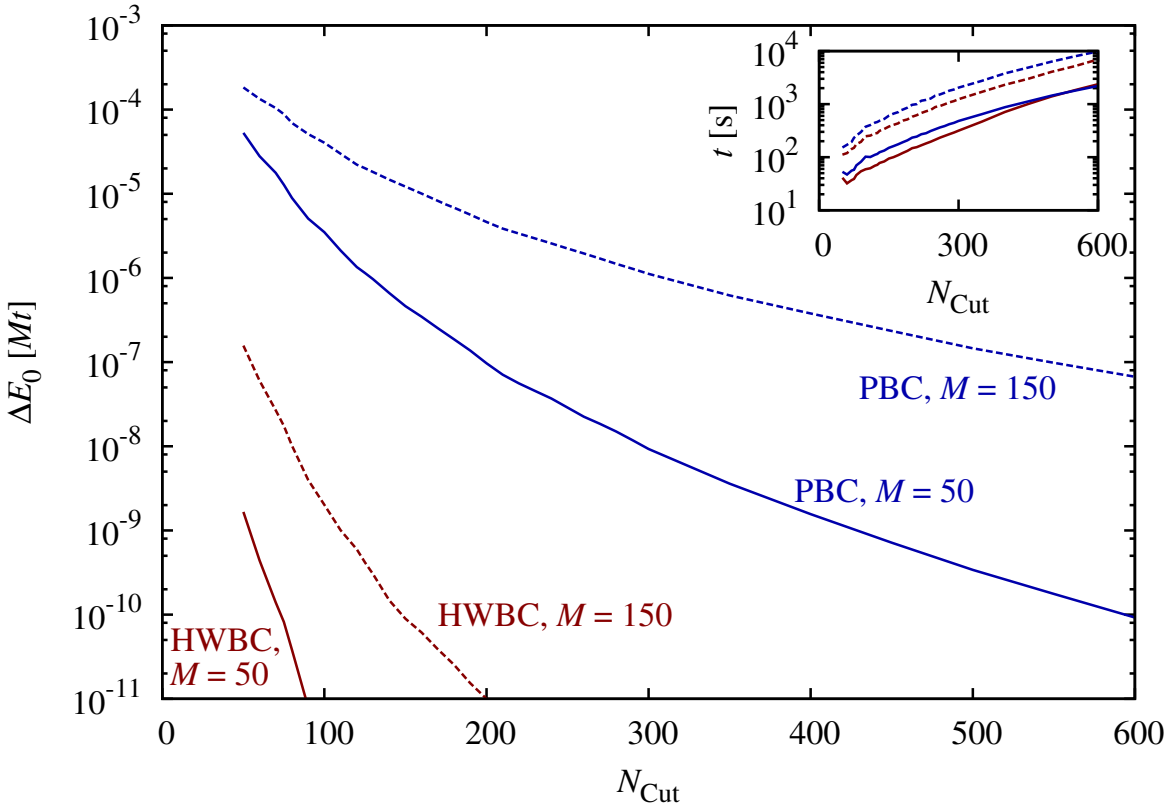

Figure 3.4: When comparing the application of the DMRG to strict one-dimensional spinless systems of size M with periodic (PBC) or hard wall boundary conditions (HWBC) the method shows a better convergence for the latter one. This can be seen both when looking at the difference of the obtained ground state energy to the real one ΔE_0 and when comparing the time t the computation takes (inset) with respect to an increase of the number of states N_{Cut} kept in the density matrix.

In addition, this procedure motivates to enlarge the Hilbert space, on which the DMRG is usually operating, to the space of linear operators acting on it. Without changing the DMRG algorithm much, this allows one to target in (3.4) not only the ground state but the full statistical operator as well (without determining the full spectrum in detail). Since in the infinite temperature limit this matrix is given by the unit matrix, finite temperature properties can be accessed by implementing a suitable evolution, i.e. cooling, technique [133, 134]. However, when cooling the system more entries of the statistical operator become non-zero and therefore important. This means that the appearing matrices are again not sparsely occupied leading to an increase of memory usage. The technique therefore breaks down at low temperatures. For that reason, this work will develop methods accessing finite temperature properties where the DMRG will operate only on the Hilbert space as discussed above.

The substitution of the target in (3.4) of the former method is not the only way of accessing finite temperature properties. In particular, substituting the ground state in (3.4) by the eigenstate of the transfer matrix with the largest eigenvalue leads to the transfer matrix renormalization group (TMRG) [126]. This means instead of diagonalizing the Hamilton matrix of the superblock C the transfer matrix of this block is constructed. Afterwards, its eigenstate with the largest eigenvalue is again determined by iterative diagonalization techniques. Since this leads to targeting the maximum eigenvalue of the superblock during the sweeps of the TMRG the thermodynamic limit is obtained right away. Within this technique it is possible to calculate thermodynamic properties of mostly two-dimensional classical systems and some corresponding quantum-mechanical systems [135]. Nevertheless, this technique only works for those few specific types of systems and is technically difficult since the transfer matrix is non-hermitian. Therefore, additional techniques have to be developed in order to calculate expectation values which are dependent on temperature for more general systems.

3.3 Calculation using Excited States

Since the presented DMRG algorithm so far does not allow the evaluation of thermodynamic expectation values without increasing the memory requirements enormously, the remainder of this chapter will be concerned with the implementation of a temperature scale into the DMRG without this need. In particular, thermodynamic quantities are of interest. In order to calculate those quantities, according to (2.11) or (2.25) energies of excited states are needed. Within the DMRG framework these expectation values can be calculated by targeting not only the ground state of the superblock, but also the excited states as well. The reduced density matrix (3.5) is then determined by the sum over all their contributions

$$\rho_A = \sum_n \mathrm{Tr}_B \left|\Psi_{Cn}\right\rangle\left\langle\Psi_{Cn}\right| . \tag{3.8}$$

As a modification of this technique, the statistical operator (2.10) is sometimes already introduced in the sum of (3.8).

However, the number of excited many-body states grows rapidly with increasing system size as mentioned previously. For instance, while for a canonical ensemble consisting of $N = 7$ spinless fermions distributed on $M = 14$ sites 3432 excited states are needed to compute the exact curve of the specific heat, this number increases for 30 sites at half filling to over 10^8. Nevertheless, in restricting the sum in (2.11) or (2.25) to the lowest eigenstates it should be possible to obtain the low temperature behavior for a certain system size (cf. (2.26)):

$$Z_N \approx \sum_{n<\mathrm{cutoff}} \mathrm{e}^{-\beta E_n} \tag{3.9}$$

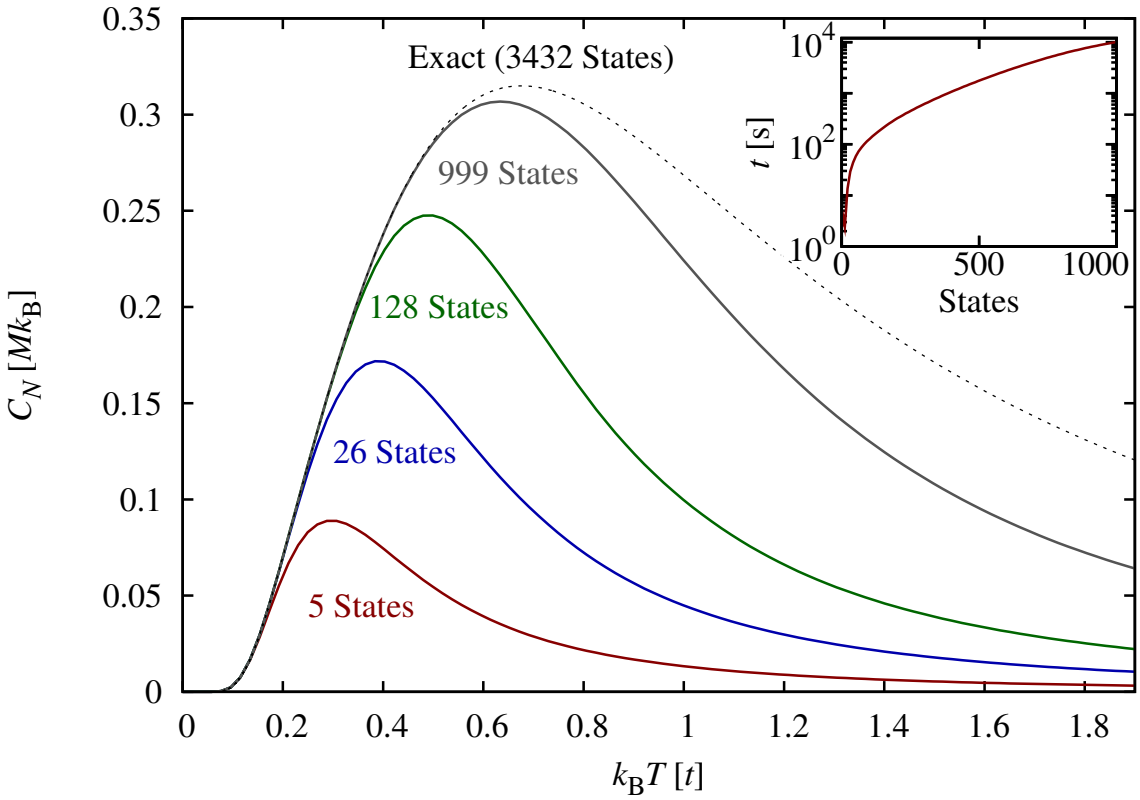

Figure 3.5: Specific heat of $N = 7$ spinless non-interacting fermions distributed on a ring (2.3) with $M = 14$ sites. Depending on how many excited states according to (2.6), (2.13) and (3.9) are considered in a DMRG calculation the exact curve (dashed line) is approximated with different quality. Initially, the validity range with respect to temperature is rapidly increasing while afterwards convergence becomes very slow. However, in taking into account more states the computation time (inset) and memory demand increases rapidly too. Due to the large degeneracy (cf. Fig. 2.1) the curves represent the consideration of all degenerate energy levels in (3.9) up to and including the first, fifth, 15^{th} and 65^{th} excited one (from 215 in total).

Even so, the scaling of the breakdown temperature of this method with the cutoff is still a cause for concern. While in the case of spectral functions it is still possible to gain valuable insight [136], in the case of the specific heat convergence with increasing the number of excited states is very poor (cf. Fig. 3.5). The reason for this behavior lies in the growing number of states needed when the probed energy region is located near the middle of a many-body band: In contrast to the edge of the band which is characterized by a large gap between the many-body states due to the finite system size, the gaps between the excited many-body states in the middle of the band are narrower (cf. Fig. 2.1). While for a low cutoff this means that the breakdown temperature can greatly be increased by

taking more states, for a cutoff where the corresponding states lie within the many-body band the augmentation of this temperature is only marginal. In particular, this leads to the conclusion that it is not possible to access the behavior in the thermodynamic limit, where the finite size gap vanishes, by this technique.

3.4 Thermal Quantum States

Since in the previous section the evaluation of the sum appearing in the partition function caused numerical difficulties in (3.9), in the remainder of this chapter the explicit evaluation of this sum will be avoided. Ideal would be an evaluation process like the one used in case of a pure state as prescribed by quantum mechanics. There, the formulation of the problem in terms of field theory, using creation and annihilation operators (2.4), allowed the extraction of the desired values by a diagonalization process. In fact, finite temperature expectation values (2.16) are surprisingly similar to quantum mechanical ones. This becomes clear if the contribution of the statistical operator is split into two parts which are related to the states over which the trace is running:

$$\langle \hat{X} \rangle_{\beta,\mu} = \sum_n \langle n| \frac{1}{\sqrt{Z_\mu}} \mathrm{e}^{-(\hat{H}-\mu\hat{N})\beta/2} \, \hat{X} \, \frac{1}{\sqrt{Z_\mu}} \mathrm{e}^{-(\hat{H}-\mu\hat{N})\beta/2} \, |n\rangle \tag{3.10}$$

If the sum in this formula was not present, thermodynamic expectation values could be calculated like in quantum mechanical field theory by assuming the system would be in the state $\mathrm{e}^{-(\hat{H}-\mu\hat{N})\beta/2}|n\rangle/\sqrt{Z_\mu}$. However, the external sum prevents defining a simple state which characterizes the system at finite temperature in general.

In 1975, Takahashi and Umezawa [137] presented an analytical way to overcome this difficulty and therefore laid the corner stone to what was later called a thermo field theory. To this purpose, he proposed to enlarge the Hilbert space by a copy of the system, so that the orthogonality relation between the supplementary eigenstates $|\tilde{n}\rangle$ can be used to define a thermal quantum state

$$|\beta\rangle_\mu = \frac{1}{\sqrt{Z_\mu}} \sum_n \mathrm{e}^{-(\hat{H}-\mu\hat{N})\beta/2} \, |n\rangle \times |\tilde{n}\rangle \,, \tag{3.11}$$

where $\times$ denotes the direct product. This state will then represent the system at a certain temperature since the expectation value of an arbitrary operator under this state determines the thermodynamic one:

$$\begin{aligned} {}_\mu\langle\beta|\hat{X}|\beta\rangle_\mu &= \frac{1}{Z_\mu} \sum_{n,m} \langle n| \mathrm{e}^{-(\hat{H}-\mu\hat{N})\beta/2} \, \hat{X} \, \mathrm{e}^{-(\hat{H}-\mu\hat{N})\beta/2} \, |m\rangle \langle\tilde{n}|\mathbb{1}|\tilde{m}\rangle & (3.12) \\ &= \frac{1}{Z_\mu} \sum_n \mathrm{e}^{-\beta(E_n-\mu N_n)} \langle n|\hat{X}|n\rangle & (3.13) \end{aligned}$$

Thereby, note that the sum in (3.11) include only the same excited eigenstates of both subspaces, but the operators appearing in (3.12) only act on the part of the Hilbert space of the original system.

Finding a thermal quantum state at finite temperature is still challenging. However, this task simplifies in the limit of infinite temperature $\beta \to 0$. In this limit the proposed state is uniformly distributed on the combined eigenspaces of the system and its copy:

$$\Big(\langle n| \times \langle \tilde{n}|\Big)|\beta = 0\rangle_\mu = \frac{1}{\sqrt{Z_\mu}} \tag{3.14}$$

Still, if a basis transformation is only applied to the system states,

$$|n\rangle = \sum_k U_{nk} \, |k\rangle \, , \tag{3.15}$$

this distribution would change in general:

$$\Big(\langle n| \times \langle \tilde{n}|\Big)U^\dagger|\beta = 0\rangle_\mu = \frac{1}{\sqrt{Z_\mu}} \, {U_{nn}}^* \tag{3.16}$$

In order to preserve the equal distribution, the supplementary states $|\tilde{n}\rangle$, which later became known as ancilla states, are entangled with the ones of the original system by forcing a similar basis transformation on the ancilla space [138]

$$|\tilde{n}\rangle = {U_{kn}}^* \, |\tilde{k}\rangle \, , \tag{3.17}$$

where ${U_{kn}}^*$ represents the complex conjugate of the entries of the transpose of the transformation matrix U. Therefore, the state in this limit is characterized by a uniform distribution in any basis:

$$|\beta = 0\rangle_\mu = \frac{1}{\sqrt{Z}} \sum_n |n\rangle \times |\tilde{n}\rangle = \frac{1}{\sqrt{Z}} \sum_{n,k} U_{nk} \, {U_{kn}}^* \, |k\rangle \times |\tilde{k}\rangle = \frac{1}{\sqrt{Z}} \sum_k |k\rangle \times |\tilde{k}\rangle \tag{3.18}$$

For numerics, this means that such a state can easily be created since a uniform distribution in the real space basis can be used. Therefore, only an evolution technique has to be found in order to obtain those thermal quantum states at lower temperatures. Since the entanglement with the ancilla state has to be taken into account (3.17) the evolution technique is more advanced but could successfully be implemented in the DMRG algorithm [139]. In addition, cooling the system iteratively, as in the implemented scheme, might lead to an increasing numerical error. Therefore, the technique fails when low temperature expectation values are addressed. Hence, a way to generate a state, like the thermal quantum one, at finite temperature would be beneficial.

3.5 Thermal States

In this section we address two goals which arose in the last section, namely generating a thermal state which characterizes the system at arbitrary temperature, and reducing the necessary memory by avoiding ancilla states. While the former one will be discussed later on for a weakly interacting system, the latter one will be addressed in the following.

For thermodynamic properties like the specific heat in (2.14), the considered operators in (3.10), $\hat{H}$ and $\hat{H}^2$, commute with the Hamiltonian and therefore possess already a common eigenspace with the statistical operator. The increase in system size by the ancilla space and the more complicated algorithm is therefore not necessary. Instead, the thermal state,

$$|\beta, \Phi\rangle_N = \frac{1}{\mathcal{N}} \sum_n \mathrm{e}^{-E_n\beta/2 + i\Phi_n} |n\rangle \,, \tag{3.19}$$

in the original Hilbert space can be used in order to obtain those expectation values. Here, the normalizing partition function was substituted by a normalization constant $\mathcal{N}$ since for practical application its contribution would be calculated as the norm of this state, e.g. for the canonical ensemble:

$$\begin{aligned} \langle \hat{X} \rangle_{\beta,N} &= \frac{{}_N\langle \beta, \Phi | \hat{X} | \beta, \Phi \rangle_N}{{}_N\langle \beta, \Phi | \beta, \Phi \rangle_N} = \frac{1}{Z_N} \sum_{n,m} \langle n | \, \mathrm{e}^{-\hat{H}\beta/2} \, \hat{X} | m \rangle \, \mathrm{e}^{-E_m\beta/2} \\ &= \frac{1}{Z_N} \sum_{n,m} \langle n | \, \mathrm{e}^{-\hat{H}\beta/2} \, | m \rangle X_m \, \mathrm{e}^{-E_m\beta/2} = \frac{1}{Z} \sum_n \mathrm{e}^{-\beta E_n} X_n \end{aligned} \tag{3.20}$$

In addition, supplemental phases Φ_n have been introduced in (3.19) to the former definition (3.11) since they will cancel when calculating the expectation value but will prove useful later on. Therefore, the system at a specific temperature can not only be characterized by one special state but by one out of a certain set. However, note that since the ancilla states were not used the knowledge of the eigenstates of the system are necessary in order to construct such states. Generating an equal distribution in another basis as previously mentioned will therefore not lead to a thermal state in the infinite temperature limit in general, in contrast to previous studies [140].

A given thermal state in the original Hilbert space can easily be evolved describing a cooling of the system. The operator needed for this process is the statistical operator where the inverse temperature has been replaced by half of the difference between the target β and initial inverse temperature β_0:

$$\hat{T}(\beta - \beta_0) = \mathrm{e}^{-\hat{H}(\beta-\beta_0)/2} = \mathrm{e}^{i\hat{H}(i(\beta-\beta_0)/2)} \tag{3.21}$$

which resembles the time evolution operator but with a purely imaginary time equal to this difference (multiplied by the imaginary unit i). Therefore Krylov subspace techniques,

e.g. the Arnoldi algorithm, can be applied in order to evaluate the action of this operator onto the initial thermal state [141, 142]. Thereby, the Hamilton operator in (3.21) is projected onto the Krylov space (3.1) allowing the calculation of the full matrix exponential. The Krylov space is then enlarged until the gain in precision falls below a predefined accepted error margin, e.g. for the calculations following below 10^{-9}. Therefore, this technique allows preservation of the unitarity of the real time evolution operator instead of other methods like the Runge-Kutta algorithm [143], but can also be applied to ladder systems in contrast to Suzuki-Trotter based approaches [144].

An initial thermal state can easily be generated in the special case of a system without interaction in the grand canonical ensemble. Since in this case the many-body states are constructed simply by a tensor product $\bigotimes$ in occupation number formalism, the thermal state should be represented by

$$\bigotimes_k \Big(|0\rangle_k + b_k \, \mathrm{e}^{i\phi_k} |1\rangle_k \Big) = \sum_{n \subseteq \{x | 1 \leq x \leq M\}} \prod_{q \in n} b_q \, \mathrm{e}^{i\phi_q} \bigotimes_{k \notin n} |0\rangle_k \otimes \bigotimes_{q \in n} |1\rangle_q \tag{3.22}$$

$$= \sum_n \mathrm{e}^{\sum_q \ln b_q + i \sum_q \phi_q} |n\rangle \, , \tag{3.23}$$

where $|0\rangle_k$ describes the unoccupied and $|1\rangle_k$ denotes the occupied state k. Comparison with the grand canonical version of (3.19) determines the relative occupation probability b_k leading to the thermal state as

$$|\beta, \Phi\rangle_\mu = \bigotimes_k \left(\sqrt{f\Big(-(\varepsilon_k - \mu)\beta \Big)} |0\rangle_k + \sqrt{f\Big((\varepsilon_k - \mu)\beta \Big)} \, \mathrm{e}^{i\phi_k} |1\rangle_k \right) \tag{3.24}$$

$$\propto \bigotimes_k \Big(|0\rangle_k + \, \mathrm{e}^{-(\varepsilon_k - \mu)\beta/2 \, + \, i\phi_k} |1\rangle_k \Big) \, , \tag{3.25}$$

with $\Phi_n = \sum_{k \in n} \phi_k$ and where ε_k are the single-particle energies and f denotes the Fermi function (2.18). Note that in this expression, the 2^M arbitrary phases Φ_n introduced in the sum over many-body states in (3.19) have been restricted to the combination of M site depended ones ϕ_k due to the use of the single particle picture. However, they can again be generalized if a linear combination of those tensor product states is considered. Remarkably, in the normalized state (3.24) the coefficients represent the hole and particle occupation number amplitude combined with an arbitrary relative phase. Since in the canonical case the particle number constraint is present in the partition sum (2.25) and therefore in the definition of the thermal state (3.19) the tensor product in the above calculation has to be restricted to satisfy this constraint as well:

$$|\beta, \Phi\rangle_N = \bigotimes_k \left(\sqrt{f\Big(-(\varepsilon_k - \mu)\beta \Big)} |0\rangle_k + \sqrt{f\Big((\varepsilon_k - \mu)\beta \Big)} \, \mathrm{e}^{i\phi_k} |1\rangle_k \right) \Big|_N \tag{3.26}$$

Within exact diagonalization the evolution of those states show very good results (cf. Fig. 3.6). In addition, these results indicate, that the thermal state of the system

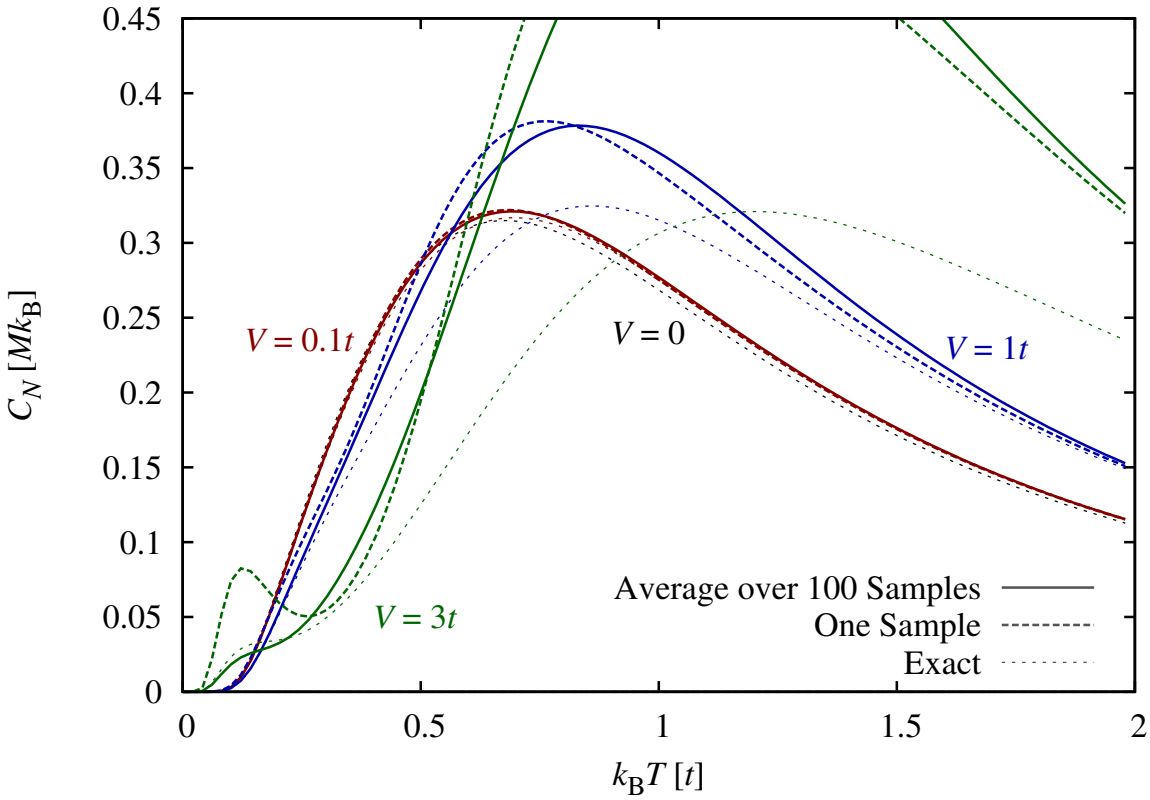

Figure 3.6: Results for the specific heat for the ring (2.3) with $M = 14$ sites and $N = 7$ particles obtained within exact diagonalization by using the thermal state of the non-interacting system as a trial one for the interacting system. Even in the strong interacting case $V = 3t$, the results after sampling the concerning expectation values $\langle H\rangle_{\beta,N}$ and $\langle H^2\rangle_{\beta,N}$ approach the exact curve of the specific heat for low temperatures. The additional peak which emerges there is due to the phase transition between the charge density wave and the Luttinger liquid (cf. Fig. 2.3).

with interaction might be well approximated by that of the system without interaction. In addition, this agreement can be increased if the arbitrary phases are sampled. This stochastic sampling would decrease the noise in the exponential decay of the overlap of the trial thermal state with the excited states of the interacting system (cf. Fig. 3.7). Such a decay with respect to the many-body eigenenergies would be obtained by the real thermal state according to (3.19).

This technique can be implemented within the DMRG framework since the thermal state is build as a tensor product. For instance, the Hamilton matrix can be represented in the DMRG procedure in Fourier representation. When the block size is enlarged by an additional site (3.7) the occupation number operator $\hat{n}_k$ of this site k would be diagonal. Therefore, the ground state of the superblock $|\Psi_C\rangle$, which is afterwards used to generate

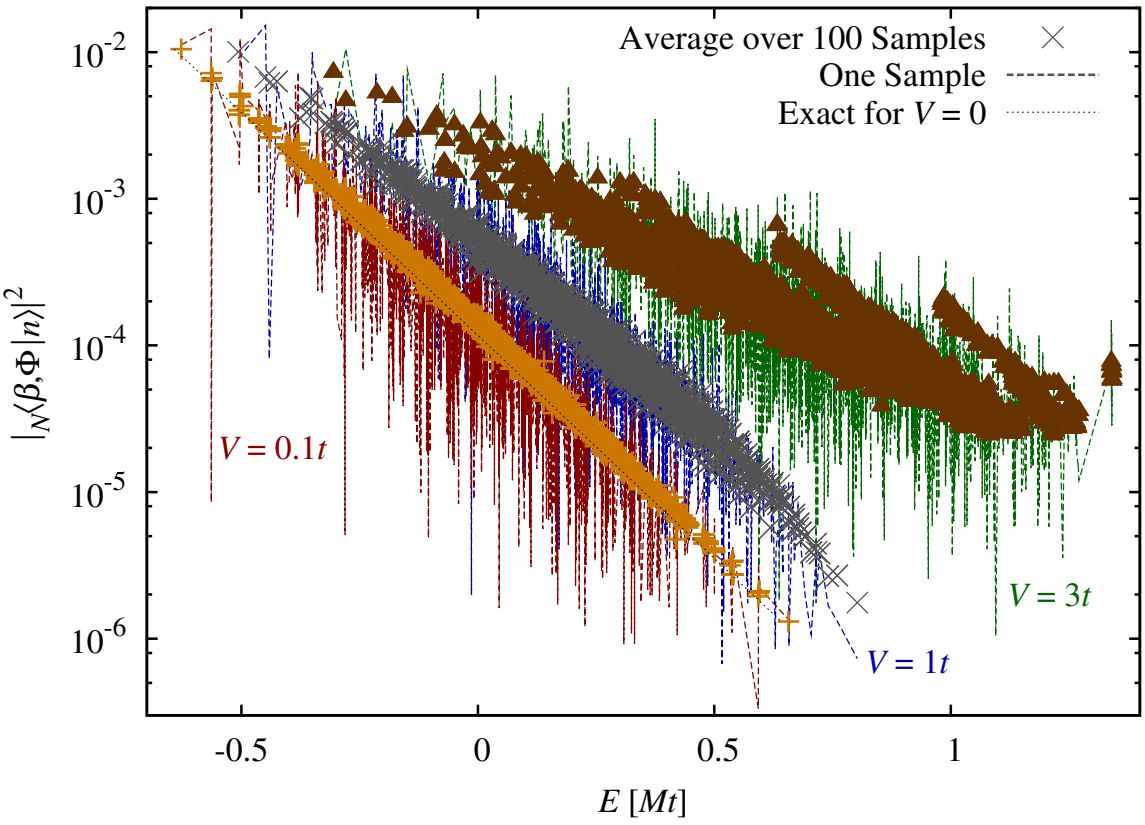

Figure 3.7: Results for the distribution of the trial thermal state $|\beta, \Phi\rangle_N$ with $\beta = 0.5t$ projected on the excited states $|n\rangle$ of the interacting system for the ring (2.3) with $M = 14$ sites and $N = 7$ fermions obtained within exact diagonalization. According to (3.19) this would be an exponential decay for the true thermal state which is shown for the non-interacting case for comparison. Since the interaction increases the energy of the system in (2.3), the curves of the interacting system is shifted to larger energies. As seen, sampling over relative phases between single-particle eigenstates with occupied and unoccupied sites reduces the noise greatly. Even in the strong interacting regime $V = 3t$, where the ground state has completely changed into a charge density wave, an exponential decay is obtained in the low energy region after sampling. Nevertheless, additional spikes in the averaged curves appear at larger energy leading to substantial disagreement between the obtained curves of the specific heat and the exact one at high temperature (cf. Fig. 3.6).

the density matrix (3.4), can be decomposed by applying this operator as well as its complement $\mathbb{1} - \hat{n}_k$. These components can then be weighted by the coefficients of the thermal state in (3.24) in order to construct a suitable target for the DMRG. This leads to excellent agreement between the calculated curve of the specific heat with respect to temperature and the exact one for the non-interacting system (cf. Fig. 3.8). Furthermore, this observation still holds if the curves are compared to the results of the low temperature approximation (3.9) for an interacting system in its validity region.

3.6 Stochastic Sampling Techniques

While in the last section a thermal state, which characterizes a system at a given temperature, could be generated for weakly interacting systems, applying this framework to arbitrary interaction strength is questionable. Nevertheless, from the situation considering weak interaction it could be inferred that stochastic sampling was beneficial to the goal of finding an initial thermal state. In fact, in order to calculate thermodynamic expectation values depending on temperature, stochastic sampling can already be introduced in their definition (2.16). In practice, this means replacing the trace over the states of the whole Hilbert space by randomly obtained states $|\xi\rangle$:

$$Z_N \langle \hat{X} \rangle_{\beta,N} = \sum_n \langle n| \, \mathrm{e}^{-\beta \hat{H}} \hat{X} |n\rangle \approx \sum_\xi \langle \xi| \, \mathrm{e}^{-\beta \hat{H}} \hat{X} |\xi\rangle = \sum_{n,\xi} |\langle \xi | n \rangle|^2 \, \mathrm{e}^{-\beta E_n} X_n \,, \tag{3.27}$$

where for simplicity again an operator was assumed which commutes with the Hamiltonian for a canonical ensemble.

Jaklič [145] argued that the random states $|\xi\rangle$ and the application of the statistical operator in (3.27) can be obtained within the Lanczos algorithm from iterative exact diagonalization techniques. Thereby from an initial, random state the basis states of a Krylov space (3.1) are generated. These states can then be used to evaluate the high temperature expansion of (3.27)

$$Z_N \langle \hat{X} \rangle_{\beta,N} \approx \sum_\xi \sum_k \frac{(-\beta)^k}{k!} \langle \xi | \hat{H}^k \hat{X} | \xi \rangle \,. \tag{3.28}$$

The results are afterwards averaged over a few randomly chosen initial states. However, while this technique proves reliable at high temperatures by construction, sampling errors occur at low temperatures. An improvement can be made by splitting the statistical operator in two steps, one before and one after the considered operator [146]. This means treating the stochastically chosen states more like the thermal one in (3.20). Nevertheless, this technique assumes that the convergence with the number of random samples is sufficiently fast which is still demanding at very low temperatures.

The reason for this breakdown becomes clear when the overlaps of the randomly chosen states in (3.27) are compared to those of the thermal state (3.19). While at high temperatures the thermal state is nearly uniformly distributed at low temperates its distribution

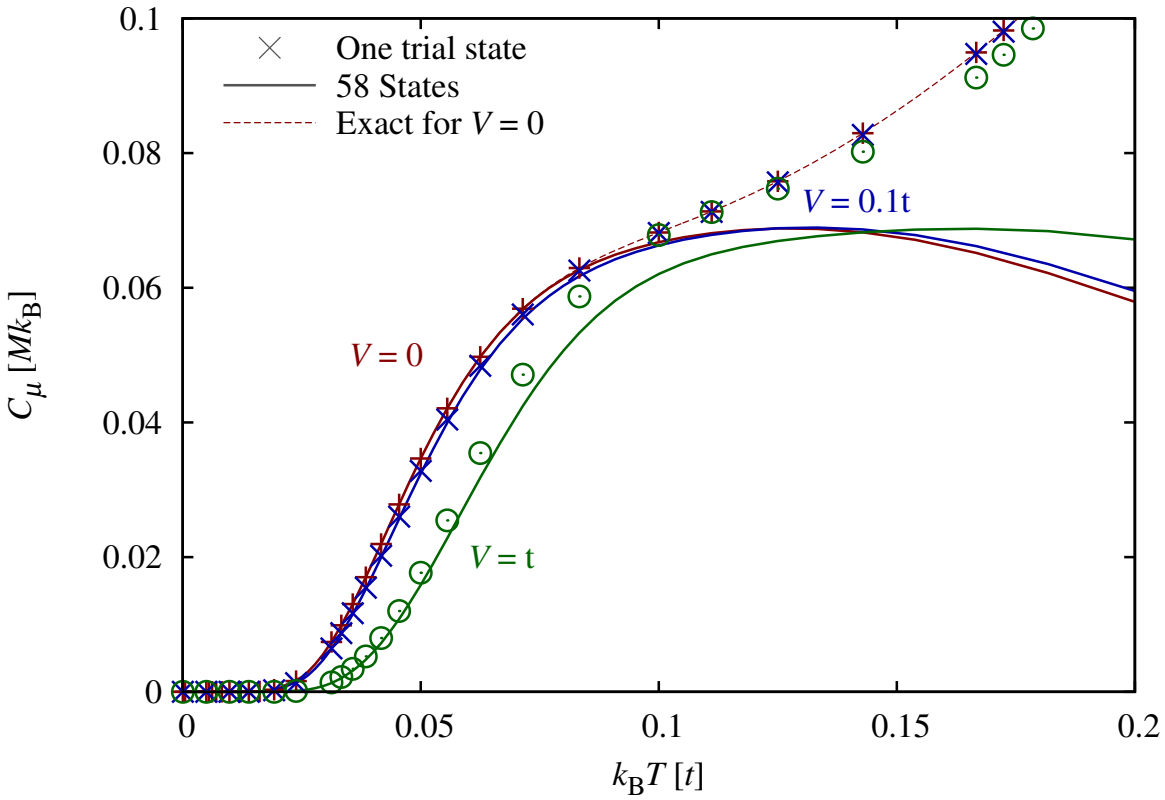

Figure 3.8: Results for the specific heat for the ring (2.3) with $M = 30$ and $\mu = 0$ obtained within the DMRG framework by using a trial thermal state for different interaction strength V. For finite interaction strength the chemical potential is fixed to the above value by using the particle-hole symmetric version of (2.3), i.e. lowering the energy by $V\hat{N}$ where $\hat{N}$ is the particle number operator. Therefore the system remains at half filling.

decays exponentially with the excitation energy of the many-body states. Therefore at low temperature the randomly chosen states should have a larger overlap with the ground state of a system in order to resemble the thermal state more adequately. For this goal the original Hamiltonian can be perturbed by diagonal disorder of maximum strength W and the ground state of the new Hamiltonian can be used as random state. However, as seen by the phases of the thermal state at the end of the last section 3.5, a complex disorder might be important as well. Therefore a complex off-diagonal disorder along hopping bonds was added to the Hamiltonian too:

$$|\xi\rangle \in \left\{ \text{ground state}\left(\hat{H} + \sum_j [\mu_j \, \hat{n}_j + (t'_j + i t''_j) \, \hat{c}^\dagger_j \, \hat{c}_{j+1}] + \text{h.c.} \right) \middle| \, \mu_j, \, t'_j, \, t''_j \in [0, W] \right\} \quad (3.29)$$

The resulting overlap with the excited states of the clean system obtained from exact diagonalization decays for the ring (2.3) surprisingly close to an exponential one (cf. Fig. 3.9).

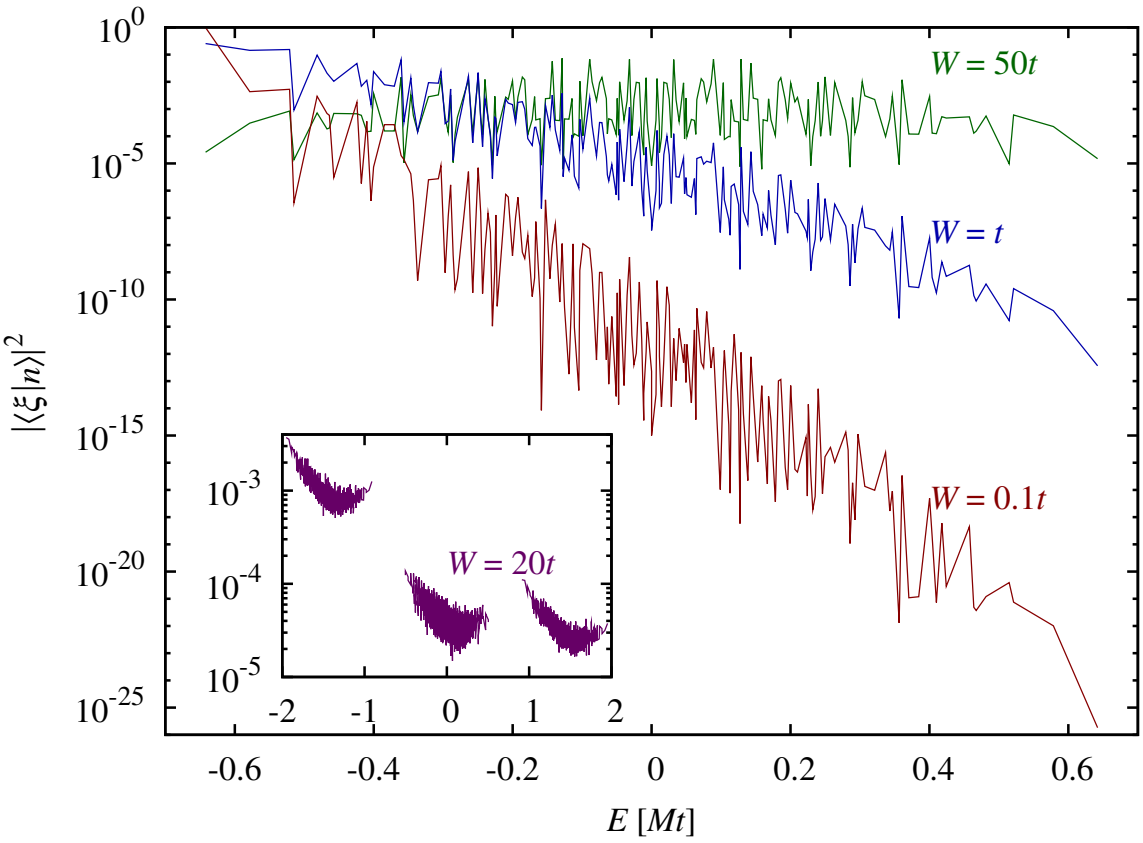

Figure 3.9: Overlap of the ground state of a perturbed system Hamiltonian (with maximum disorder strength W) with the excited states of the original one for the ring of size $M = 14$ with $N = 7$ spinless non-interacting fermions. The result is nearly an exponential decay. In addition, the inset shows the overlap of a similar system (3.30) where one site is taken out of ring and has an increased hopping amplitude $t' = 20t$. This causes the degenerate levels to split and therefore three separate many-body bands occur. However, for those multiple many-body bands slight deviations from an exponential decay can be seen.

The occurrence of such an exponential decay for a sparsely occupied off-diagonal on top of a diagonal perturbation of the original Hamiltonian was already noted in [147] but were placed there in the framework of a quantum micro-canonical ensemble where the expansion (2.10) is not valid. However, the temperature of the states generated is not known, but will scale with the maximal disorder strength W used. This allows the reaching of higher temperatures. Nevertheless, a larger maximal disorder strength might lead to the need of taking into account a large number of samples.

Furthermore, deviations from the decay of a thermal state occurs if the system has multiple energy scales. For instance, consider the non-interacting ring if one site is separated from it but coupled to one site of the remaining ring by a strong hopping amplitude t'.

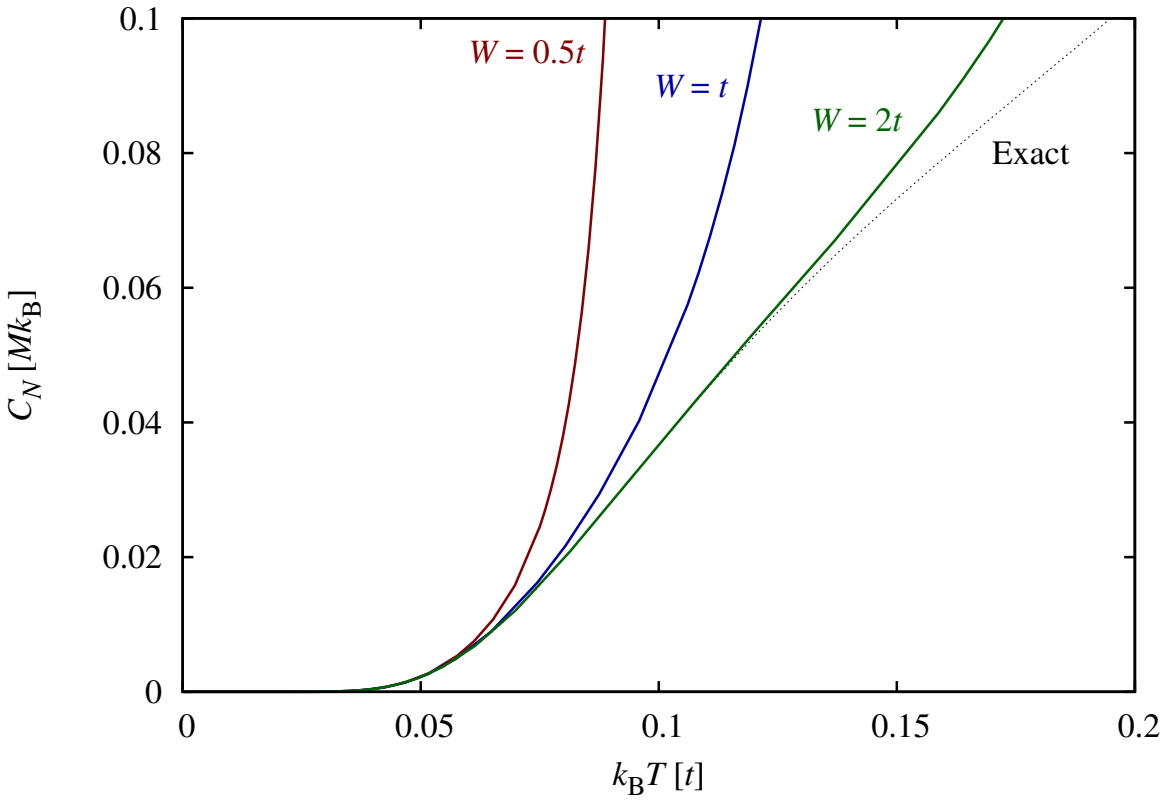

Figure 3.10: Specific heat of the ring of spinless fermions for $M = 30$, $N = 15$ and $V = 0$. The temperature region in agreement increases with larger maximal disorder strength W.

The Hamiltonian for this system therefore reads

$$\hat{H} = t'\hat{c}_1^\dagger\,\hat{c}_2 + t\sum_{j=2}^{M}\hat{c}_{j+1}^\dagger\,\hat{c}_j + \text{h.c.}\,, \tag{3.30}$$

with the periodic boundary condition $\hat{c}_{M+1} = \hat{c}_2$ since the first site represents the separated site. Applying the transformation $U = \exp(i\sigma_y\pi/4)\otimes\mathbb{1}_{M-2}$, where σ_y represents the second Pauli matrix acting on the first two sites, this model can be rewritten as

$$\hat{\tilde{H}} = t'\hat{\tilde{n}}_1^\dagger - t'\hat{\tilde{n}}_2 + t\sum_{j=2}^{M}\hat{\tilde{c}}_{j+1}^\dagger\,\hat{\tilde{c}}_j + \text{h.c.}\,, \tag{3.31}$$

where the operators $\hat{\tilde{X}}$ denote the transformed operators. Thus the ring can be viewed as small perturbation in the case $t \ll t'$ whose degeneracies are therefore lifted and formerly one many-body band is separated into three around $-t'$, 0, t'. The perturbation to the

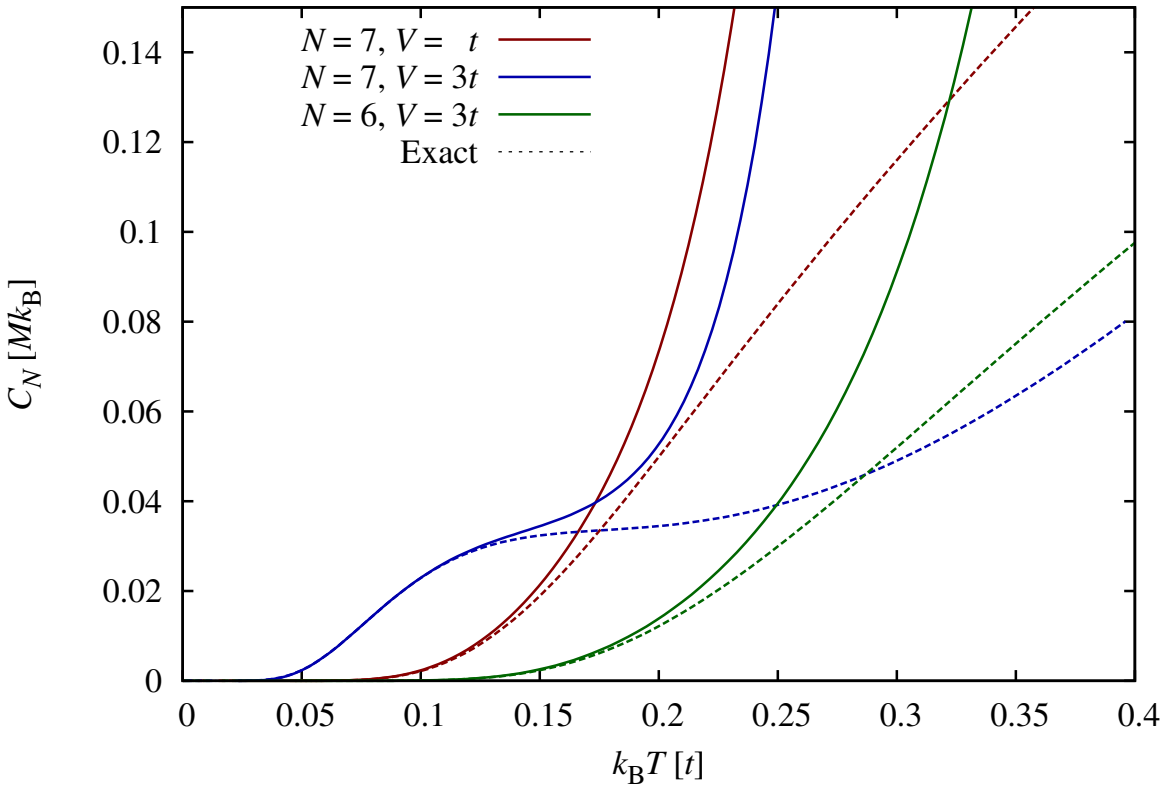

Figure 3.11: When interaction is introduced in the ring with $M = 14$ sites the formation of the charge density wave is visible by an emerging peak in the specific heat calculated by stochastic sampling techniques with $W = t$. Therefore making a bandwidth as well as a filling controlled quantum phase transition observable.

hopping along the new topology leads again nearly to an exponential decay. However, the construction of the disorder Hamiltonian (3.29) ensures in this case only an increased overlap with the lowest eigenstates. If another high energy structure is present, like the splitting into the three many-body bands in this model, an exponential decay is not guaranteed. This is visible at the upper band edges as well as increased overlap elements for the highest band. Nevertheless, since this band will only contribute to the specific heat at very high temperature, its influence should not matter much.

While the imaginary time evolution will allow the study of the cooling of the system, the determination of the temperature of the initial state is still challenging. In order to resolve this issue the result, e.g. for the specific heat, can be fitted to the low temperature expansion (2.27) by adjusting the initial temperature β_0. This means that an additional DMRG run is necessary to determine enough states to obtain the finite size gap. The results for the specific heat show a deviation at first, but after a few iteration of the imaginary time evolution the perturbations from an exponential decay seem to cease to be important, thus achieving agreement with the exact curve (cf. Fig. 3.10). Furthermore, this agreement

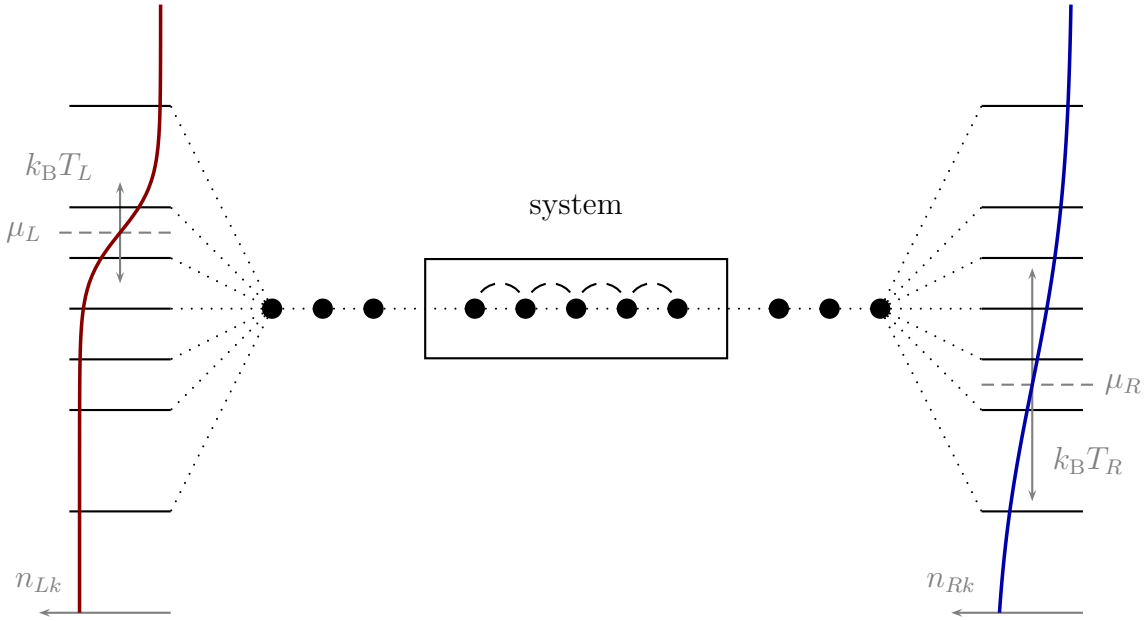

Figure 3.12: Setup for measuring the thermopower of a one-dimensional system (boxed) consisting of hopping (dotted) and interaction (dashed) within the DMRG framework using the implementation of a thermal state. The system is enframed on both sides by thermal states constructed according to (3.25) but placed on different temperatures T_L and T_R as well as different chemical potentials μ_L and μ_R in order to simulate an applied voltage bias $\Delta V = e(\mu_L - \mu_R)$. In determining the voltage bias where no current flows in the system the thermopower can be accessed.

still holds even if interaction is present, allowing the study of quantum phase transitions with this method (cf. Fig. 3.11).

3.7 Summary and Outlook

The formulation of the expectation values at finite temperature by the quantum-mechanical expression using a thermal quantum state showed that in principle one state is sufficient to describe the system at finite temperature. However, considering expectation values of any operator in general needs the enlarging of the original Hilbert space and therefore an increase in memory. Luckily, in order to obtain canonical thermodynamic quantities which are given by sums over the momenta of the Hamiltonian, the enlarging is not necessary.

However, finding such a state is still critical. In particular, just taking a random state would not be sufficient for the method using the original Hilbert space. Better would be a cleverly chosen state. For instance, we propose using the one generated for the non-interacting system even for the corresponding interacting system. Still, if any interaction is present the quantities obtained by those states will still show deviations.

Therefore one has to switch to stochastic techniques. From them the question arises over which kind of accessible variables can be sampled. In order to access thermodynamic quantities of interacting systems we showed that the intrinsic freedom of complex phases in the thermal state of the non-interacting system can be used. This procedure can even be implemented in the DMRG framework, but is questionable for large interaction strength.

For a more general approach of accessing low temperatures we further suggested to target states which lie close to the ground state. Therefore the ground state was taken from a Hamiltonian where the on-site potential as well as the hopping parameters could stochastically vary. This led to good agreement for the specific heat, where an augmentation of the disorder strength led to an increase of the temperature region which could be accessed. Thereby stressing the role of sampling in order to obtain a suitable state.

Furthermore, with the implementation in the DMRG framework of such thermal states even for the non-interacting case, we think it might be possible to access the thermopower. In order to achieve this goal we suggest replacing the momentum leads by leads containing a thermal state in the framework of measuring the conductance [148, 149]. This means the DMRG should be applied to a total system where the system under consideration is enframed by sites occupied according to the thermal state (cf. Fig. 3.12). Adding a coupling between all these sites and the sites at the edge of the system would then lead to a coupling of these thermal environments to the system. If in addition, the chemical potentials of these environments are varied like for the case of measuring the conductance, a voltage bias will lie across the system. For a given temperature difference between the environments this voltage drop is then adjusted, so that no current is flowing through the system. Hence, with this technique the validity of the TICR approximation could be investigated.

Chapter 4

Analytic Approximations at Finite Temperatures

In this chapter, the apparent Fermi liquid (AFL) behavior observed for the delafossites will be studied. This behavior was characterized among others by a linear thermopower with respect to temperature and included a finite offset for a temperature region close to room temperature (cf. Fig. 1.3). It was observed in doped $CuRhO_2$ [19] and doped $CuCrO_2$ [29]. The interpretation for the phenomenon of both materials will be given at the end of this chapter. Before this a theoretical framework will be developed in order to derive a similar behavior.

However, the application of numerical techniques is still challenging. On the one hand first principle techniques, like the augmented spherical wave method (ASW), seem to describe well the low temperature limit while the slope of the AFL behavior is still overestimated [19]. This might indicate many-body scattering contributions, which lead to the question if the TICR constant E_0 in (2.47) can cover them. On the other hand, using a microscopic model is very demanding since many overlapping bands contribute to the band structure as seen in Fig. 1.5.

Therefore, this chapter is concerned with an analytic treatment of the phenomenon. Such a treatment not only allows the discussion of the stability of the AFL, but also provides analytic expressions which can easily be fitted to experiments. In the extreme case, this might lead to a recipe for experimentalists on how to scale the axes of their diagrams to extract microscopic quantities, like the degeneracy in case of modified Heikes formulas (2.41). Thus allowing an easy application of the phenomenological theory to further measurements. Furthermore, an analytic treatment might provide insight into the underlying mechanism and therefore a better understanding.

However, such a treatment is based on a starting point which can be motivated by the structure of the delafossites presented in section 1.2. When discussing Fig. 1.4 and 1.5 there, these materials were characterized by a perturbed two-dimensional structure which is slightly doped. In neglecting higher bands the behavior should therefore be dominated by the discontinuous band edge, especially at high temperatures, when the chemical potential

has left the band. Therefore a suitable starting point would be the expansion of the density of states as a Taylor series around the band edge[1]

$$\rho(\varepsilon) = \sum_{n=0}^{\infty} \frac{\rho_n}{n!} \varepsilon^n \cdot \Theta(\varepsilon)\Theta(W-\varepsilon)\,, \tag{4.1}$$

where W describes the bandwidth, ρ_n denotes the limit of the n-th derivative of the density of states as the energy approaches the band edge from within the band, i.e. $\varepsilon \to 0^+$, and the zero point of the single-particle energies was placed at the band edge. Furthermore, their thermopower, where an AFL behavior was clearly seen, might be determined by the chemical potential through the TICR approximation in (2.47). This quantity was implicitly determined in (2.22) by the density in the system which resembles the doping value $\mathrm{x} = N/M$. For the Taylor series above and a sufficiently large bandwidth, $W \to \infty$, this condition takes the form (cf. appendix)

$$\mathrm{x} = \int_{-\infty}^{\infty} \rho(\varepsilon)\, f\Big(\beta(\varepsilon-\mu)\Big)\, \mathrm{d}\varepsilon = -\sum_n \rho_n \beta^{-(n+1)}\, \mathrm{Li}_{n+1}(\nu)\,, \tag{4.2}$$

where $\nu = -\,\mathrm{e}^{\beta\mu}$ denotes the negative fugacity and Li the polylogarithm.

In the first part of this chapter, different approximation schemes will be developed and applied, in order to extract a behavior of the chemical potential which could explain the observed behavior of the thermopower when using the TICR approximation (2.47). This includes the application of the conventional low and high temperature expansions in terms of the polylogarithm in section 4.1 and 4.2 but in the framework of the polylogarithm. The results of these approximations will be exemplified by comparison to the exact solution given by numerics. For clarity, merely the case where only the first two coefficients of the density of states in (4.1) are non-vanishing will thereby be shown since this limit will be used in the following part, too. This second part is then concerned with application of the theory to the thermopower of doped $CuCrO_2$ (section 4.5) and doped $CuRhO_2$ (section 4.6). Thereby, it will be shown how to gain access to the parameters in the density of states as well as the charge carrier density by measuring the thermopower. The results are summarized in the concluding section 4.7.

4.1 Low Temperature Expansion

The low temperature regime of the doping number constraint as formulated in (4.2) can be accessed by an expansion of the polylogarithm for large negative arguments since the

[1] In fact, the calculation done in this chapter can easily be generalized to arbitrary (non-integer) powers in the series by replacing the factorial by the Gamma function. Only the expansion of the polylogarithm at low temperature (cf. appendix) might cause concern but the behavior can be obtained by the common Sommerfeld approximation.

chemical potential $\mu > 0$ lies within the band for the doped materials. As shown in the appendix expanding the polylogarithm for $\beta\mu \gg 1$ leads to

$$\mathrm{x} = \int_0^\mu \rho(\varepsilon)\ \mathrm{d}\varepsilon + \frac{\pi^2}{6}\rho'(\mu)\,(k_\mathrm{B}T)^2 + \mathcal{O}(T^4)\,, \tag{4.3}$$

which is known from Sommerfeld expansion too. Therefore the chemical potential should be quadratically dependent on temperature as in the three-dimensional case (2.23)

$$\mu = \varepsilon_F - \varpi\,T^2 + \mathcal{O}(T^4) \quad \text{with} \quad \varpi = \frac{\pi^2}{6}{k_\mathrm{B}}^2\frac{\rho'(\varepsilon_F)}{\rho(\varepsilon_F)}\,, \tag{4.4}$$

where ε_F denotes again the Fermi energy and $\rho'(\varepsilon)$ is the derivative of the density of states with respect to energy. This result leads within the TICR framework to

$$S_\mathrm{TICR} = \frac{\varpi}{q_e}\cdot T\,, \tag{4.5}$$

where the result has been used that the TICR constant should vanish for a metal as discussed in section 2.3. However, as seen from the determination of the coefficient ϖ in (4.4), the low temperature thermopower given by (4.5) will vanish for a strict two-dimensional metallic system described by a constant density of states (2.21), $\rho'(\varepsilon_F) = 0$, since the chemical potential is independent of temperature in this limit.

Similarly, the specific heat of the canonical system can be shown to be linear with respect to temperature (cf. appendix):

$$C_\mathrm{x} = \gamma\,T + \mathcal{O}(T^3) \qquad \text{with} \qquad \gamma = \frac{\pi^2}{3}\rho(\varepsilon_F)\,{k_\mathrm{B}}^2 M \tag{4.6}$$

In addition, a similar ratio of the thermopower in the TICR approximation (2.47) and the specific heat as in (2.51) can be found: In the case when the Taylor series of the density of states is dominated by only one term with power n, the resulting ratio becomes again only dependent on the doping:

$$\mathfrak{q}_\mathrm{TICR} = -\frac{\varpi}{\gamma} = -\frac{1}{2M}\frac{\rho'(\varepsilon_F)}{\rho(\varepsilon_F)^2} = -\frac{1}{2\mathrm{x}}\frac{n}{n+1} \tag{4.7}$$

Note however the findings of section 2.3: In the low temperature limit the TICR approximation might not be valid, therefore this ratio might get renormalized, e.g. there for the three-dimensional system by a factor of six.

Furthermore, the technique described by using an expansion for $\beta\mu \gg 1$ of the polylogarithm allows a breakdown temperature to be obtained. As a measure of the condition where the expansion is violated, the temperature where $\beta\mu = 2$ can be taken. With this breakdown criteria and the chemical potential from (4.4), this breakdown temperature is given by

$$T_S = \frac{\sqrt{1 + \varepsilon_F\varpi/{k_\mathrm{B}}^2} - 1}{\varpi/k_\mathrm{B}}\,. \tag{4.8}$$

The region in the phase diagram where the temperature is below the stated one will be denoted as Sommerfeld region. Remarkably, the above temperature is smaller than the Fermi temperature

$$T_F = \frac{\varepsilon_F}{k_\mathrm{B}} \,. \tag{4.9}$$

In particular, for small Fermi energies and quadratic coefficients of the chemical potential, like in the case where only a discontinuity at the band edge is present ($\varpi = 0$), this temperature amounts to half of its value. When comparing the numerical inversion of (4.2) it was found in Fig. 4.1 that the stated temperature (4.8) describes the breakdown better than the Fermi temperature (4.9). In contrast, for less dominant discontinuity the approximation (4.4) might even be valid slightly above the temperature T_S. Since the delafossites showed a dominant discontinuity, a Fermi liquid behavior in these materials is expected to break down earlier than indicated by the Fermi temperature. For this reason and to be able to investigate alternative behaviors, approximation schemes at higher temperature will be discussed in the following.

4.2 High Temperature Expansion

For high temperatures the chemical potential of (4.4) will be far below the band edge. Since this means that $\beta\mu \ll -1$ the Taylor series of the polylogarithm (A.13) can be used. Using only the linear term of this series in the negative fugacity $\nu = -\,\mathrm{e}^{\beta\mu}$ will result in the doping constraint (4.2) given by

$$\mathrm{x} = \sum_n \rho_n \beta^{-(n+1)}\, \mathrm{e}^{\beta\mu} + \mathcal{O}(\mathrm{e}^{2\beta\mu}) \,. \tag{4.10}$$

Thus it resembles the result known if the Fermi function is replaced by the Boltzmann distribution in the original integral definition (2.22). Therefore the chemical potential in this approximation μ_B follows as

$$\mu_B = -k_\mathrm{B}T \,\, \ln \frac{k_\mathrm{B}T\, \tilde{\rho}(k_\mathrm{B}T)}{\mathrm{x}} \,, \tag{4.11}$$

where a renormalized density of states is introduced

$$\tilde{\rho}(\varepsilon) = \sum_n \rho_n \varepsilon^n \cdot \Theta(\varepsilon) \,. \tag{4.12}$$

Although this quantity is only an abbreviation in the above formula, its interpretation will become clear in the next section. The region in the phase diagram where the formula (4.11) is valid will be called Boltzmann region. The border of this region can be described by a similar breakdown temperature as introduced previously for the Sommerfeld region, but

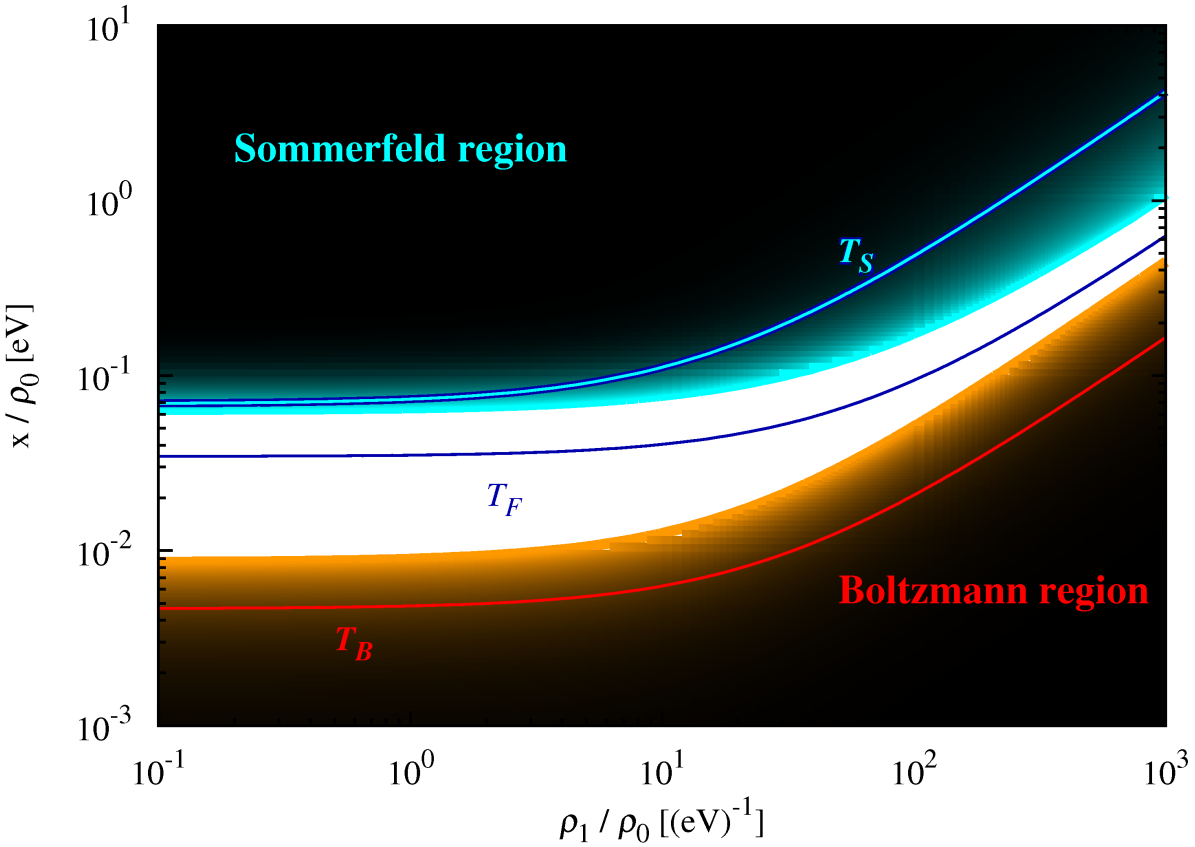

Figure 4.1: Comparison of the result for the chemical potential in low and high temperature expansion (4.4), (4.11) to the numerical solution of (4.2) at a temperature $T = 400\,\mathrm{K}$ for different materials described by a density of states which only contains the first two terms of a Taylor series $\rho(\varepsilon) = (\rho_0 + \rho_1\varepsilon) \cdot \Theta(\varepsilon)$ and is doped by a fraction of x charge carriers. The areas denote the relative error between the exact solution an the approximated ones up to 10%. The lines describe the parameter values if the breakdown or Fermi temperatures become equal to the specific temperature T.

now for the condition $\beta\mu_B = -2$. However, in (4.10) this requires the inversion of the function $\tilde{\rho}$ following from the density of states:

$$\mathrm{x}\,\mathrm{e}^2 = k_\mathrm{B} T_B\, \tilde{\rho}(k_\mathrm{B} T_B) \tag{4.13}$$

Assuming that the breakdown temperature T_B is still small, the function $\tilde{\rho}$ is governed by the first terms of the Taylor series. Thus this temperature scale is given by

$$T_B \approx \frac{\sqrt{1 + 4\,\mathrm{e}^2 \mathrm{x} \rho_1/\rho_0^2} - 1}{2 k_\mathrm{B} \rho_1/\rho_0}\,. \tag{4.14}$$

Furthermore, above this temperature a linearization of the expression (4.11) around a certain temperature $\tilde{T}$

$$\mu_B = \mu_B^{(0)} + \mu_B^{(1)} \, (T - \tilde{T}) - \varpi \, (T - \tilde{T})^2 \,, \tag{4.15}$$

$$\mu_B^{(0)} = -k_{\mathrm{B}}\tilde{T} \;\ln \frac{k_{\mathrm{B}}\tilde{T}\,\tilde{\rho}(k_{\mathrm{B}}\tilde{T})}{\mathrm{x}} \,, \tag{4.16}$$

$$\mu_B^{(1)} = -k_{\mathrm{B}} \;\ln \frac{k_{\mathrm{B}}\tilde{T}\,\tilde{\rho}(k_{\mathrm{B}}\tilde{T})}{\mathrm{x}} - k_{\mathrm{B}}[1 + k_{\mathrm{B}}\tilde{T}(\ln\tilde{\rho})^{(1)}] \,, \tag{4.17}$$

$$\varpi = \frac{k_{\mathrm{B}}}{2\tilde{T}}[1 + 2k_{\mathrm{B}}\tilde{T}(\ln\tilde{\rho})^{(1)} + (k_{\mathrm{B}}\tilde{T})^2(\ln\tilde{\rho})^{(2)}] \,, \tag{4.18}$$

where $(\ln\tilde{\rho})^{(n)}$ denotes the n-th derivative of the logarithm of the renormalized density of states at the thermal energy $k_{\mathrm{B}}\tilde{T}$, proves to be a good approximation, at least if again a dominant discontinuity or a linear term is assumed (cf. Fig. 4.1).

In addition, since at these high temperatures the chemical potential is believed to have left the band, the occurring situation might be similar to the one discussed at the non-resonant level model (2.46). Then the TICR approximation should be valid. Combining the above expression with this approximation (2.47) leads to a linear thermopower

$$S_{\mathrm{TICR}} = \frac{E_0 - \mu_B^{(0)} + \mu_B^{(1)}\tilde{T} + \varpi\tilde{T}^2}{q_e} \cdot \frac{1}{T} - \frac{1}{q_e}(\mu_B^{(1)} + 2\varpi\tilde{T}) + \frac{\varpi}{q_e} \cdot T \tag{4.19}$$

$$= \frac{E_0 - \tilde{\varepsilon}_F}{q_e T} - S_0 + \frac{\varpi}{q_e} T \,. \tag{4.20}$$

In contrast to the low temperature behavior (2.50) this expression contains a finite offset S_0, as seen in experiments (cf. Fig. 1.3), as well as a hyperbolic offset. However, the linear term ϖT will not be dominant if the expansion temperature is sufficiently large. Therefore, the thermopower could be interpreted as constant with temperature, in similarity to the known plateau like behavior from the Heikes formula (2.41). In addition, its doping dependence would be given by that of the chemical potential (4.11) which resembles for low doping the result in the atomic limit as will be discussed in more detail later on.

In summary, the result obtained in this section might explain the AFL behavior seen for doped $CuRhO_2$. However, if the parameters of the density of states are extracted out of the band structure Fig. 1.5 the calculated breakdown temperature of this approximation (4.14) will be larger than the temperature where the behavior has been observed in the experiments. Furthermore, for dominant discontinuity the gap between this breakdown temperature and the one from the low temperature expansion (4.8) opens considerably (cf. Fig. 4.1). Therefore another approximation is needed to investigate the missing region.

4.3 Approximation of the Polylogarithm Difference

In order to fill the gap arising between the Boltzmann and Sommerfeld region, it is useful to take a closer look at the similarity of the polylogarithm of different orders (cf. Fig. 4.2). While every polylogarithm intersects at the origin and have the same slope there as well (cf. appendix), their behavior still remains similar at finite negative arguments. Since the first polylogarithm resembles an elementary function $\mathrm{Li}_1(\nu) = -\ln(1-\nu)$, it is very appealing to consider the other orders in terms of an approximation of the polylogarithm difference (APLD) [23]

$$d_n(\nu) = \mathrm{Li}_{n+1}(\nu) - \mathrm{Li}_1(\nu)\,. \tag{4.21}$$

Introducing and expanding this difference in (4.2) as a Taylor series around a certain negative fugacity ν_0 yields

$$\begin{aligned}\mathrm{x} = {} & k_\mathrm{B}T\,\tilde{\rho}(k_\mathrm{B}T)\ln(1-\nu) \\ & - \sum_{n\neq 0} \rho_n d_n(\nu_0)\,(k_\mathrm{B}T)^{n+1} \\ & - \sum_{n\neq 0} \rho_n \Big(d_{n-1}(\nu_0) - d_{-1}(\nu_0)\Big)\,{\nu_0}^{-1}\,(k_\mathrm{B}T)^{n+1}(\nu-\nu_0) - \mathcal{O}\Big((\nu-\nu_0)^2\Big)\,.\end{aligned} \tag{4.22}$$

The first term, proportional to the logarithm in this approximation can be understood as following from a temperature dependent averaged density of states $\tilde{\rho}$ which was already introduced in the high temperature approximation (4.12). In the case of low temperatures when the first two orders dominate this renormalized density of states, it just resembles the original density of states but taken at the thermal energy:

$$\rho(\varepsilon) \to \tilde{\rho}(k_\mathrm{B}T) \approx \rho(k_\mathrm{B}T) \tag{4.23}$$

However, it will differ from the original one for more sophisticated cases.

Additionally, the zeroth order of the Taylor series only shifts the doping value used in the theory,

$$\mathrm{x} \to \mathrm{x} + dx(k_\mathrm{B}T) \qquad \text{with} \qquad dx(k_\mathrm{B}T) = \sum_{n\neq 0} \rho_n d_n(\nu_0)\,(k_\mathrm{B}T)^{n+1}\,, \tag{4.24}$$

since this term does not depend on the chemical potential. It resembles the requirement to fulfill the doping constraint (4.2) at the expansion point.

The first order terms in this expansion would result in the chemical potential given by

$$k_\mathrm{B}T\bar{\rho}\,(1+\,\mathrm{e}^{\beta\mu})\exp\Big(k_\mathrm{B}T\bar{\rho}\,(1+\,\mathrm{e}^{\beta\mu})\Big) = k_\mathrm{B}T\bar{\rho}\exp\left(\frac{\mathrm{x} + dx(k_\mathrm{B}T) - k_\mathrm{B}T\bar{\rho}\,(\nu_0-1)}{k_\mathrm{B}T\,\tilde{\rho}(k_\mathrm{B}T)}\right), \tag{4.25}$$

where $k_\mathrm{B}T\bar{\rho}$ is the prefactor of the linear term in (4.22) similar to $dx(k_\mathrm{B}T)$ for the zeroth order. The solution of this equation can be found as the Lambert $\mathcal{W}$ function [150] with

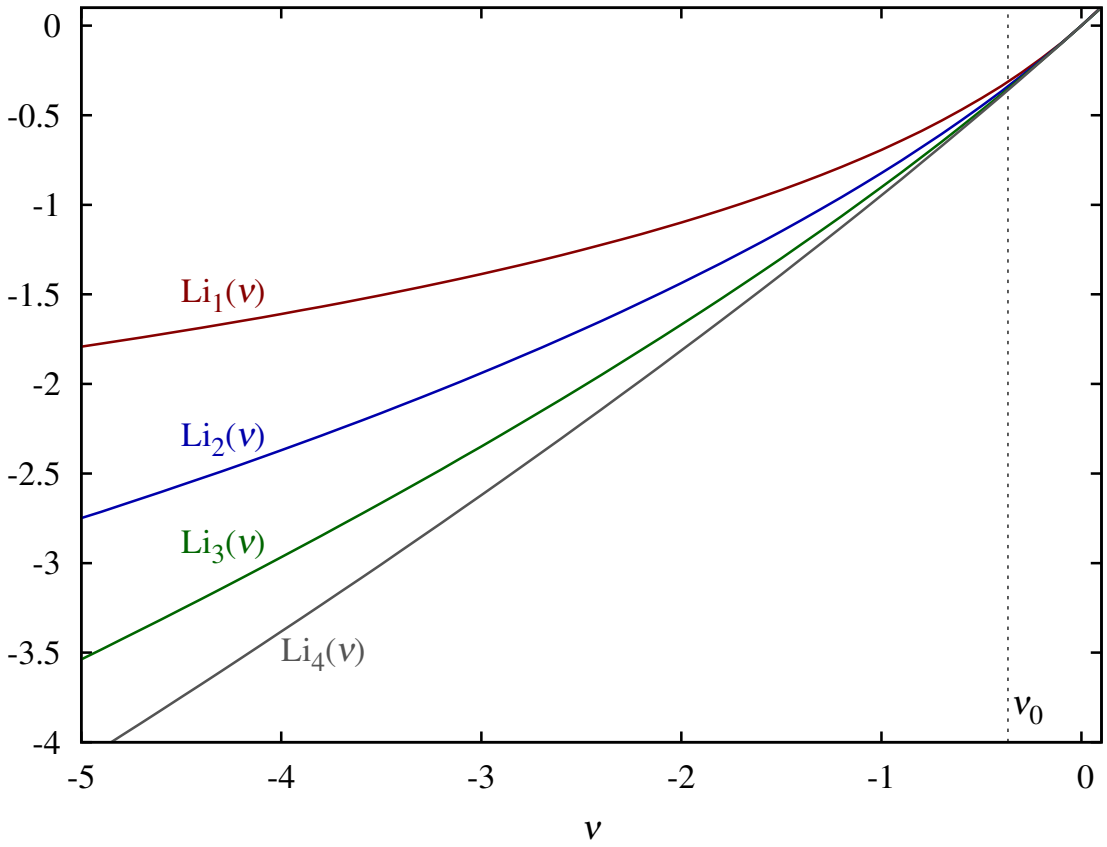

Figure 4.2: The behavior of polylogarithmic functions of different order remains similar for small negative arguments. The negative fugacity ν_0 marked on the right-hand side (dotted line) denotes the temperature T_0 which will later serve as expansion temperature (4.34).

the right-hand side as argument. Of course, for small (positive) arguments this function can again be linearized. Since this will lead to the same solution as if only the zeroth order term is taken, the first order contributions will only give corrections at large doping (4.24) or low temperatures. Therefore this as well as all higher orders will be neglected in the following, leading to the chemical potential in this approximation μ_P given as

$$\mu_P = k_\mathrm{B}T \ \ln\left[\exp\left(\frac{\mathrm{x} + dx(k_\mathrm{B}T)}{k_\mathrm{B}T\tilde{\rho}(k_\mathrm{B}T)}\right) - 1\right] \tag{4.26}$$

$$= k_\mathrm{B}T\Big(z + \ln(2\sinh z)\Big)\,, \tag{4.27}$$

with the argument of the hyperbolic function

$$z = \frac{\mathrm{x} + dx(k_\mathrm{B}T)}{2k_\mathrm{B}T\,\tilde{\rho}(k_\mathrm{B}T)} = \frac{\mathrm{x} + \sum_{n\neq 0}\rho_n d_n(\nu_0)\,(k_\mathrm{B}T)^{n+1}}{2\sum_n \rho_n\,(k_\mathrm{B}T)^{n+1}}\,. \tag{4.28}$$

In this approximation, the doping dependence of the chemical potential as seen in (4.26) changes qualitatively from the one obtained in the high temperature limit (4.11). Therefore,

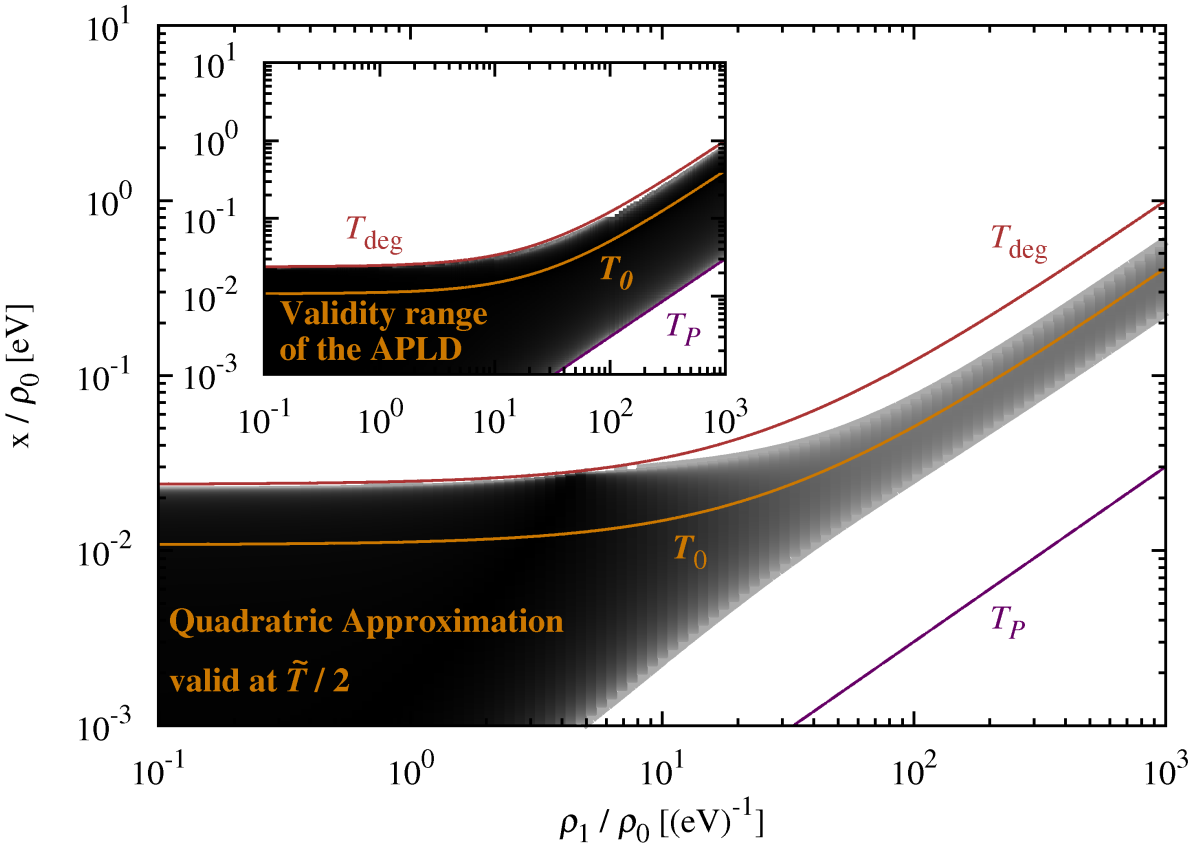

Figure 4.3: The comparison of the result for the chemical potential within the APLD similar to Fig. 4.1. The areas denote the relative error between the exact solution and the quadratic approximated one up to 100% or between the result by the APLD (4.26) and the exact solution (inset). The lines describe the parameter values if the degeneracy $T_{\rm deg}$, APLD expansion T_0 or upper-breakdown temperature T_P given by (4.30), (4.34) and (4.31) become equal to the specific temperature $T = 400\,\mathrm{K}$. The expansion temperature was taken as $\tilde{T} = 2T$.

the thermopower within the TICR approximation following from this expression can be viewed as a generalization of the Heikes formula (2.41) (cf. discussion after (4.20)).

The validity of this expression can be related to the results of the high temperature approximation and Sommerfeld expansion in particular cases: For a very large expansion temperature the difference of the polylogarithms $d_n(\nu_0)$ becomes negligible. Due to the assumed high temperatures the result of Boltzmann approximation μ_B in (4.11) is obtained by an additional expansion of the exponential function in (4.26). In contrast, in decreasing the expansion temperature the corresponding fugacity will reach unity, i.e. $\nu_0 \to -1$. After this point a slight variation of the chemical potential or the temperature will lead to a greater change in the fugacity. Therefore higher orders become important (cf. discussion after (4.25)) and the Taylor series (4.22) will break down for smaller temperature differ-

ences. This means the APLD as presented should only be used for temperatures larger than the degeneracy temperature T_{deg}. This temperature is implicitly given by

$$\mathrm{x} = -\sum_n \rho_n \,\mathrm{Li}_{n+1}(-1)\,(k_{\mathrm{B}} T_{\mathrm{deg}})^{n+1}\,. \tag{4.29}$$

If the Taylor series (4.1) is dominated by its first terms (4.29), it can be solved yielding

$$T_{\mathrm{deg}} \approx \frac{-\ln 2 + \sqrt{(\ln 2)^2 + \pi^2 \mathrm{x}\rho_1/3\rho_0^2}}{\pi^2 k_{\mathrm{B}}\rho_1/6\rho_0}\,, \tag{4.30}$$

where the chemical potential vanishes according to (4.2) (cf. Fig. 4.3). However, for a very dominant discontinuity, the first term in (4.22) will give the dominant contribution to the doping. Therefore, the other terms will resemble small corrections whose importance will decrease as the first term increases. Since the latter was treated exactly in the APLD, this means that the validity region is increased to very low temperatures. As stated, in the limit of a strict two-dimensional system when only a discontinuity is present in the density of states, the approximation becomes exact and resembles the result of Sommerfeld expansion after performing a Taylor series for small temperatures. This limit will be thoroughly discussed in the following section.

While (4.29) limits the application of the approximation (4.26) to small temperatures, it will fail for temperatures much larger than the expansion temperature T_0, too. This issue arises due to the fact that the chemical potential in this approximation has a logarithmic singularity where the argument of the exponential function in (4.26) vanishes. The singularity can also be seen in the numerical solution in Fig. 4.3 where it seems that the APLD remains valid until close to this anomaly. Since at these temperatures the high temperature approximation is valid, this approximation should be used for temperatures similar or larger than the temperature T_P which is implicitly given by

$$\mathrm{x} = -dx(k_{\mathrm{B}} T_P) = -\sum_{n\neq 0} \rho_n d_n(\nu_0)\,(k_{\mathrm{B}} T_P)^{n+1}\,, \tag{4.31}$$

where the logarithms in (4.26) has its singularity. If again the Taylor series (4.1) is dominated by its first two terms this expression simplifies to

$$T_P \approx \sqrt{\frac{\mathrm{x}}{-d_1(\nu_0)\,\rho_1 {k_{\mathrm{B}}}^2}}\,. \tag{4.32}$$

Remarkably, this temperature diverges in the two-dimensional limit where only a discontinuity is present in the density of states. This again shows that the APLD will become exact in this limit.

A suitable expansion point for the APLD therefore has to lie between the degeneracy temperature (4.29) and this singularity temperature (4.31). Since the breakdown temperature of the high temperature approximation (4.14) will always be larger than the

latter temperature the expansion fugacity $-\nu_0$ has to take a value between e^{-2} and unity, i.e. $-1 \leq \nu_0 \leq -\mathrm{e}^{-2}$. It is therefore appealing to use $\nu_0 = -\mathrm{e}^{-1}$ which means the chemical potential is at the thermal energy below the band edge, i.e. $\mu = -k_\mathrm{B}T$. Putting this temperature into the doping constraint (4.2) determines this temperature implicitly by

$$\mathrm{x} = -\sum_n \rho_n \,\mathrm{Li}_{n+1}(-\mathrm{e}^{-1})\,(k_\mathrm{B}T_0)^{n+1}\,, \tag{4.33}$$

which when the first terms of the Taylor series (4.1) are dominant can be solved to

$$T_0 \approx \frac{\ln(1-\nu_0) - \sqrt{\Big(\ln(1-\nu_0)\Big)^2 - 4\,\mathrm{Li}_2(\nu_0)\,\mathrm{x}\rho_1/\rho_0^2}}{2k_\mathrm{B}\rho_1/\rho_0\,\mathrm{Li}_2(\nu_0)}\,. \tag{4.34}$$

With this expansion temperature T_0, further simplifications can be brought to (4.26): In this case the absolute value of the difference of the polylogarithm functions of first orders amounts to $|d_1(\nu_0)| = 0.03$ and monotonically decreases with larger expansion temperatures. This value is significantly smaller than the corresponding coefficient in (4.22) $\ln(1+\mathrm{e}^{-1}) = 0.3$ describing the effect of the averaged density of states $\tilde{\rho}$ at this expansion temperature. Furthermore, since it gets multiplied by at least ${k_\mathrm{B}}^2T^2$ its effect to the doping at room temperature will be significantly smaller than common values of the doping. Although the difference increases slightly for higher orders (cf. Fig. 4.2), the shift of the doping dx in the expansion (4.26) may be neglected, especially if the Taylor series is governed by its first terms. Since this means neglecting even the first order in the expansion of the APLD (4.22) the expansion point ν_0 would not be present in the solution of the chemical potential (4.26). Therefore an even larger application region is expected in this case which is in agreement with the diverging behavior of the break down temperature T_P from (4.31) as well as the discussion of the lower break down temperature after (4.29).

Reviewing the results of this section, for dominating discontinuity the characteristic (breakdown) temperatures found in (4.8), (4.9), (4.14), (4.30), (4.31) and (4.34) may be ordered as

$$T_S < T_F < T_\mathrm{deg} < T_0 < T_B < T_P\,. \tag{4.35}$$

4.4 APLD and an Apparent Fermi liquid

In this section we will address the question when the chemical potential can again be approximated by a quadratic form. This would then lead within the TICR approximation (2.47) to a linear thermopower characterizing an AFL. However, as will be shown, an important tendency can be gained by considering the case where only a discontinuity is present in the density of states

$$\rho(\varepsilon) = \rho_0 \cdot \Theta(\varepsilon)\,. \tag{4.36}$$

In order to apply this insight later on to experiments, where a more realistic model would be appropriate, the general case is shortly discussed afterwards.

As mentioned previously in this limit where only a discontinuity is present (4.36) the APLD becomes exact, therefore the breakdown temperatures do not have to be considered. Performing a quadratic expansion around the transition temperature T_0 in this case leads to

$$\begin{aligned}\mu_{P-} &= \mu_P^{(0)}(\tilde{T}) + \mu_P^{(1)}(\tilde{T}) \cdot (T - \tilde{T}) - \varpi \cdot (T - \tilde{T})^2 && (4.37)\\ &= \quad k_\mathrm{B}\Big(z + \ln(2\sinh z)\Big)\tilde{T} \\ &\quad - k_\mathrm{B}\Big(z\coth z - \ln(2\sinh z)\Big)\,(T - \tilde{T}) \\ &\quad - k_\mathrm{B}\frac{z^2}{2\sinh^2 z}\frac{1}{\tilde{T}}\,(T - \tilde{T})^2\,, && (4.38)\end{aligned}$$

where the argument of the hyperbolic functions (4.28) is simplified to

$$z = \frac{\mathrm{x}}{2\rho_0 k_\mathrm{B}\tilde{T}}\,. \tag{4.39}$$

Due to the fact that the linear coefficient after reordering in powers of T will not vanish (cf. Fig. 4.4) this leads to an AFL behavior. Furthermore, the quadratic coefficient ϖ possesses in its $\tilde{T}$ dependence an inflexion point near its maximum at

$$z\coth z = \frac{3}{2}\,. \tag{4.40}$$

Thus the terms of higher order will have small values near this maximum and the quadratic expansion will approximate the function very well around this point. Therefore defining a particular expansion temperature $\tilde{T}_{P-}$. Since the numerical solution of (4.40) reads $z \approx 1.29$ this temperature is given by

$$\tilde{T}_{P-} \approx 4505\,\frac{\mathrm{K}}{\mathrm{eV}} \cdot \frac{\mathrm{x}}{\rho_0} = 0.8\,T_S = 0.3\,T_\mathrm{deg}\,. \tag{4.41}$$

An interesting aspect of this temperature is that the chemical potential have not yet moved far from the Fermi energy. In fact, the low temperature expansion (4.4) would describe a chemical potential independent of temperature. It therefore stays at the Fermi energy with increasing temperature. At the specified temperature, when it differs from the Fermi energy by $\Big(\varepsilon_F - \mu_P(\tilde{T}_{P-})\Big)/\varepsilon_F = 3\%$ it finally starts moving towards the band edge (for comparison: $\Big(\varepsilon_F - \mu_P(2\tilde{T}_{P-})\Big)/\varepsilon_F = 25\%$). This is due to the fact that the Fermi distribution is cut at the band edge (at $\tilde{T}_{P-}$ it is reduced by 8% there) while at higher energies no such cut is effective (cf. Fig. 4.5). Therefore the chemical potential has to shift to lower values in order to fulfill the doping constraint (2.22). In addition, the beginning of this shift can be approximated as a Taylor series (4.38) with non-vanishing quadratic coefficient, therefore distinguishing it from the Fermi liquid parameter. Nevertheless, a

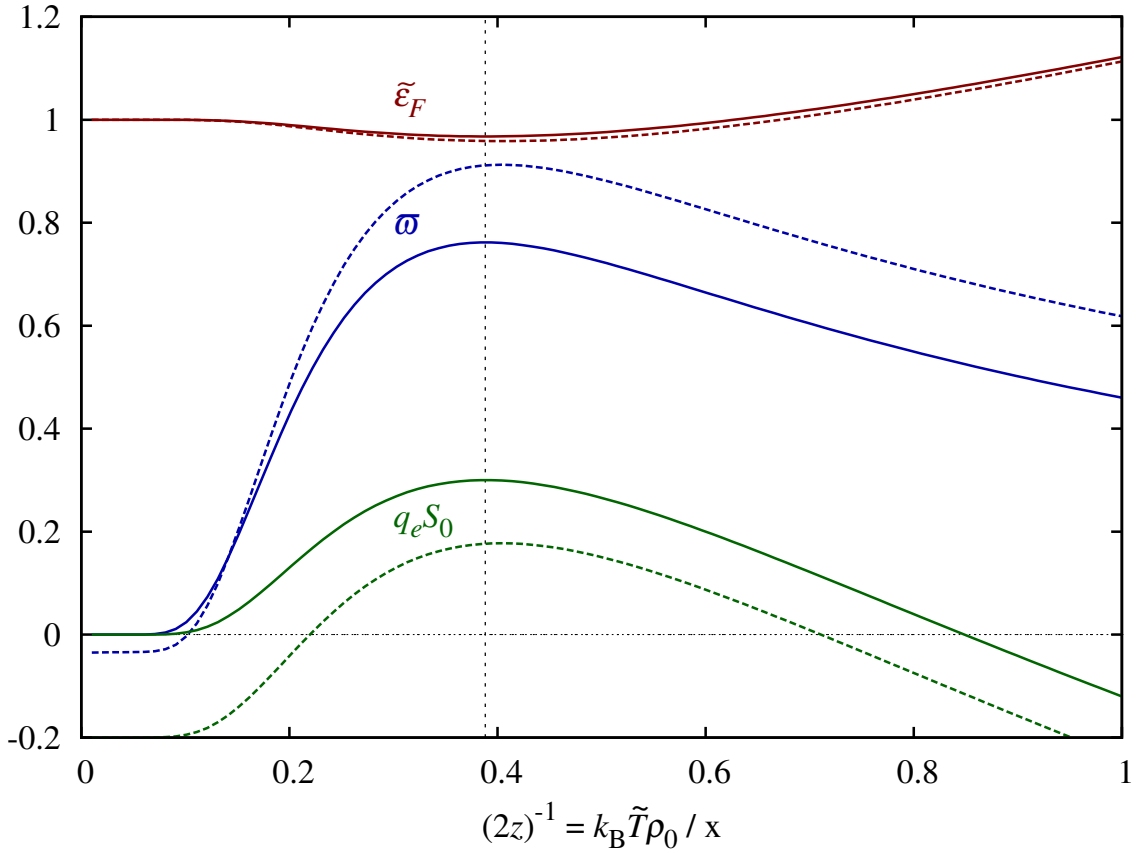

Figure 4.4: Behavior of the temperature coefficients of the quadratic expansion $\mu_{P-} = \tilde{\varepsilon}_F + q_e S_0 T - \varpi T^2$ for only a discontinuity according to (4.38). The temperature dependence of these parameters are weakest around the temperature $\tilde{T}$ given by (4.40). Additionally, the curves for an additional linear term $\rho_1 = 2\,(\mathrm{eV})^{-1}\,\rho_0$ in the density of states with a doping of $x = 0.2\,\mathrm{eV}\,\rho_0$ are shown according to (4.42) and (4.43) (dashed lines). At these values, the close stationary points have begun to shift independently, causing the AFL to destabilize. In the figure $\tilde{\varepsilon}_F$, $q_e S_0$, ϖ are given in units of ρ_0/x, ${k_B}^{-1}$ and ${k_B}^{-2}x/\rho_0$ respectively.

cross-over from a true Fermi liquid behavior, i.e. with finite parameters, to such an AFL one can not be observed in this limit.

However, on the one hand in considering very small additional coefficients of higher order terms in the Taylor series, the real Fermi liquid parameter would be non-vanishing. On the other hand, the boost of the chemical potential near the temperature $\tilde{T}_{P-}$ may still be possible to observe on top of the background behavior caused by these coefficients. Since the breakdown temperature of the observable Fermi liquid T_S will be slightly lower than the stated temperature (4.41) this leads to a comparably small transition region between a Fermi liquid and an AFL behavior. Analytically, this represents itself as follows: When taking the effects in (4.26) of the full Taylor-series of the density of states into account,

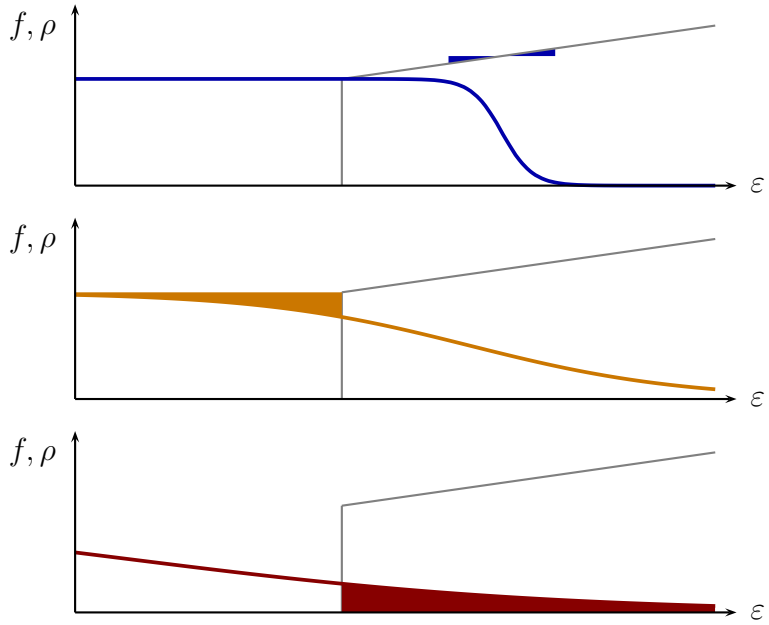

Figure 4.5: Mechanism causing the chemical potential to shift with temperature for Fermi liquid and apparent Fermi liquid behavior. For the former one (top) an asymmetry of the density of states ρ at the Fermi edge, e.g. a linear increase of states, causes a quadratically dependent chemical potential. In the high temperature expansion (bottom) the decreasing values of the Fermi function f causes the chemical potential to shift which when expanded shows a linear term as well. A similar effect can be observed at intermediate temperature (middle), only that the decreasing values outside of the band causes the shift. In the case of a dominant discontinuity this shift can even be stronger than those caused from Fermi liquid theory, and therefore it might be possible to observe this effect.

both the hyperbolic argument as described in (4.28) and the modification of the derivatives in the quadratic expansion have to be taken into account:

$$\mu_P^{(1)}(\tilde{T}) \to \mu_P^{(1)}(\tilde{T}) \quad - \quad k_\mathrm{B}\,\tilde{z}(1+\coth z)\,, \tag{4.42}$$

$$\varpi \to \varpi\left(1+\frac{\tilde{z}}{z}\right)^2 \quad + \quad k_\mathrm{B}\frac{1+\coth z}{2\Big(\tilde{\rho}(k_\mathrm{B}\tilde{T})\Big)^2}$$

$$\cdot\left[z k_\mathrm{B}\tilde{T}\tilde{\rho}^{(2)}\,\tilde{\rho}(k_\mathrm{B}\tilde{T}) + dx^{(1)}\tilde{\rho}^{(1)} - 2z k_\mathrm{B}\tilde{T}\Big(\tilde{\rho}^{(1)}\Big)^2 - \frac{1}{2}dx^{(2)}\,\tilde{\rho}(k_\mathrm{B}\tilde{T})\right], \tag{4.43}$$

with $\tilde{z}=\Big(2z k_\mathrm{B}\tilde{T}\tilde{\rho}^{(1)} - dx^{(1)}\Big)/(2\tilde{\rho})$ and where $\tilde{\rho}^{(n)}$ denotes the n-th derivative of the renormalized density of states and $dx^{(n)}$ respectively the one of the doping change both taken at the thermal energy $k_\mathrm{B}\tilde{T}$. These adjustments cause the common stationary point of all three coefficients of the chemical potential μ_{Pq}, as a polynomial in temperature T, to shift inde-

pendently (cf. Fig. 4.3). Therefore, this destabilizes the quadratic approximation thereby destroying the AFL and stressing the role of a large discontinuity for this kind of AFL. However, as expected at the beginning of this paragraph, in adjusting the doping x in the case of small other coefficients ρ_n for $n > 0$ of the Taylor series, a narrow region remains where the different stationary points are close to one another. As indicated in Fig. 4.4, the observation temperature $\tilde{T}_{Pq}$ of the AFL of this region would then be larger than the temperature given in (4.41).

In contrast to the AFL by the high temperature approximation, where the temperature only has to be larger than the breakdown temperature T_B, the AFL by APLD is centered around the temperature $\tilde{T}_{P-}$ from (4.41) if only a discontinuity is considered or slightly above for small further coefficients. In addition it crucially depends on the influence of the discontinuity. This can be seen in the phase diagram too, for instance if only a linear coefficient is considered (cf. Fig. 4.6). Of course in a realistic density of states the presence of an upper band can destroy these phases as well if the chemical potential becomes too close to it. Therefore a large enough gap is necessary too.

As mentioned previously, the offset of the thermopower within the APLD (4.42) and (4.43) with (4.19), as well as the one obtained in the high temperature approximation (4.17) and (4.18) with (4.19) can be related to modified Heikes formula (2.41) in the limit of low doping. In this case the nominator in the Heikes formula (2.41) is taken as unity leading to

$$S_{\text{Heikes}} = \frac{k_{\text{B}}}{q_e} \ln \frac{1}{x} \,. \tag{4.44}$$

Therefore only a factor in front of the argument of the logarithm is missing to obtain the formula of the high temperature approximation if the TICR constant is neglected (cf. (4.11) with (2.47)). Furthermore, as shown in previous studies [86–88] a degenerate lower level with degeneracy g leads to a shift in Heikes formula and therefore a modification of formula (4.44) by an offset of $q_e^{-1} k_{\text{B}} \ln g$. Thus, the APLD as well as the high temperature approximation result in the same formula as the modified Heikes formula for low doping if this degeneracy is identified by $g = k_{\text{B}} \tilde{T} \rho_0$ in case of a purely two-dimensional system (cf. Fig. 4.7). Remarkably, this means that not the total number of states in the lower band contributes to the thermopower, but only a small fraction of it. Reviewing this result from the atomic limit, the degeneracy of the lower level in modified Heikes formula is replaced by only that part of the broadened level which is close to its upper edge with respect to the thermal energy, similar to the discussion of properties in Fermi liquid theory (cf. Fig. 2.4). For less dominant discontinuity this identification changes in the high temperature approximation to

$$g = k_{\text{B}} \tilde{T} \, \tilde{\rho}(k_{\text{B}} \tilde{T}) \exp\Big(k_{\text{B}} \tilde{T} (\ln \tilde{\rho})^{(1)} + (k_{\text{B}} \tilde{T})^2 (\ln \tilde{\rho})^{(2)} \Big) \,. \tag{4.45}$$

However, even with this identification the modified Heikes formula can not account for the results obtained by the introduced approximations for doping values that are not that

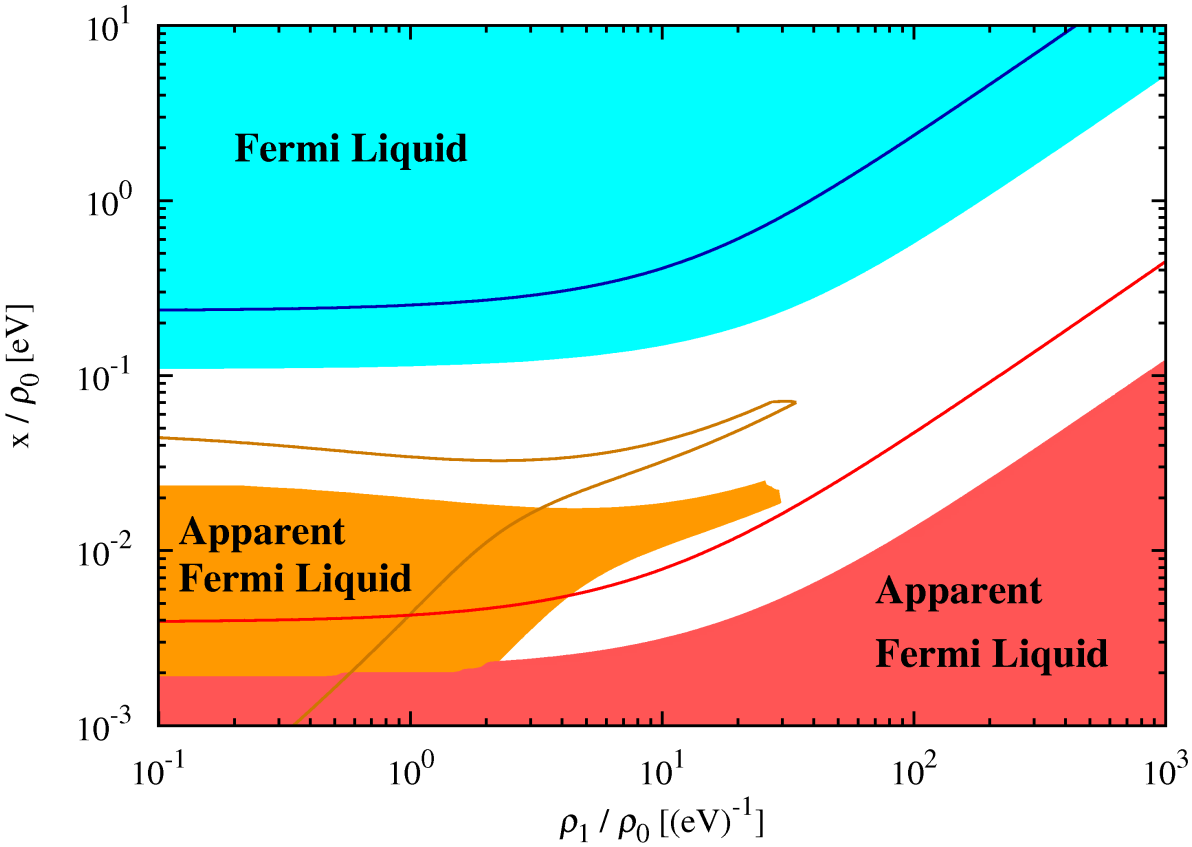

Figure 4.6: Phase diagram for a density of states given by $\rho(\varepsilon) = (\rho_0 + \rho_1\varepsilon)\cdot\Theta(\varepsilon)$, $T = 400\,\mathrm{K}$ (areas) and $T = 800\,\mathrm{K}$ (lines). In the different colored regions the relative errors between the exact solution of the chemical potential and the one described by the stated behavior is smaller than 50%. For the AFL by APLD (AFL region on the left), equations (4.42) and (4.43) are compared to (4.26), respectively for the one given by the high temperature approximation (4.11) (AFL region present in the lower right corner). In these regions the more general Fermi liquid and AFL expressions (4.4), (4.11), (4.26) differ from the exact solution by less than 1%.

small. Then the decrease of the thermopower with respect to increased doping is damped as compared to the behavior of the Heikes formula. This damping is even more pronounced in the APLD which leads astonishingly to an increase within the APLD for large doping values.

4.5 Application to the Delafossite $CuCrO_2$

In the following sections the observed AFL behavior in the thermopower of the delafossites will be studied. In particular, this section will be concerned with the AFL noticed in

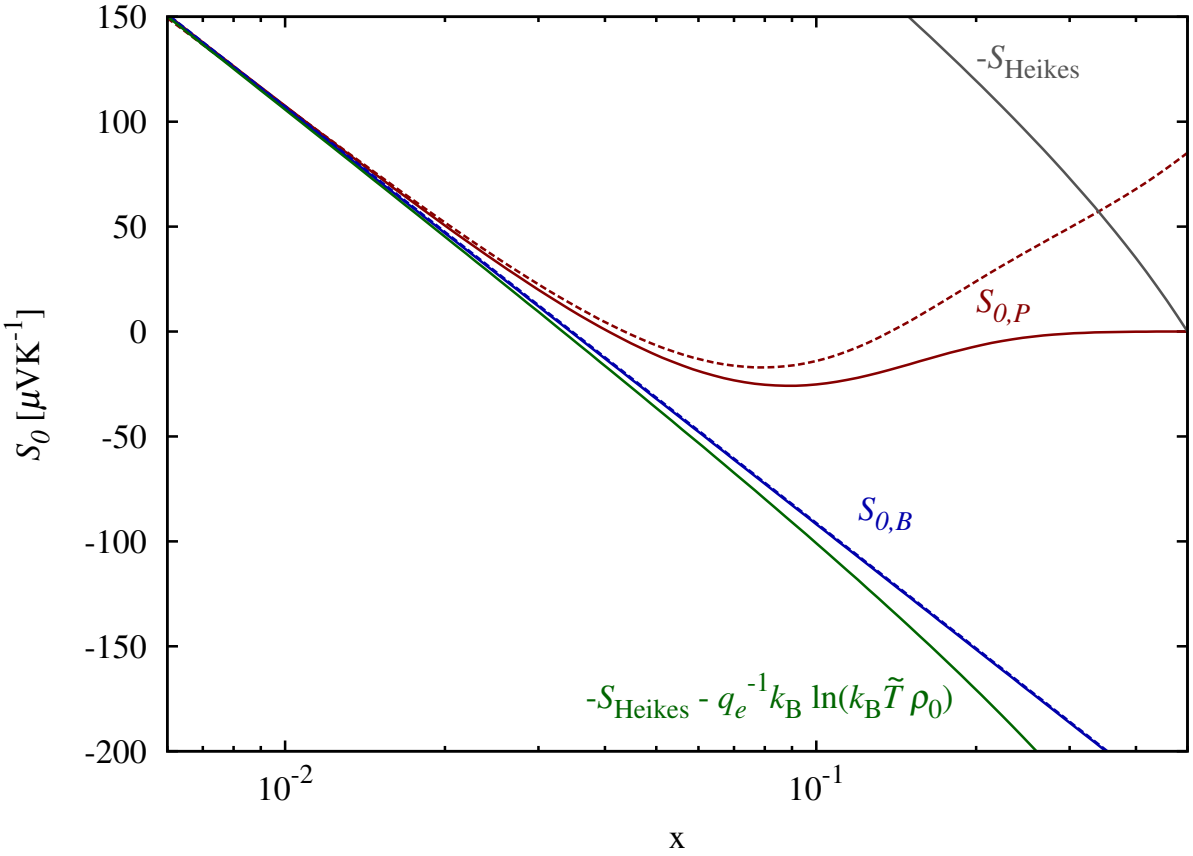

Figure 4.7: Comparison of the offsets of the thermopower (4.20) in the high temperature approximation $S_{0,B}$ as well as in the APLD $S_{0,P}$ obtained within the TICR framework. The solid lines represent the results for a purely two-dimensional system, i.e. $\rho_n = 0$ for $n > 0$ with $\rho_0 = 1\,(\text{eV})^{-1}$, while the dashed ones are drawn if an additional linear term $\rho_1 = 2\,(\text{eV})^{-1}\,\rho_0$ is present in the density of states. Both cases are shown for an expansion temperature $\tilde{T} = 400\,\text{K}$. The curve of the perturbed two-dimensional system obtained by the high temperature approximation does not change much compared to the one of the unperturbed system. In addition, the result of the Heikes formula S_{Heikes} from (2.41) is shown as well as the curve which is shifted by the proposed degeneracy factor appearing in modified Heikes formula.

$CuCr_{1-x}Mg_xO_2$ while the subsequent section is devoted to that found in $CuRh_{1-x}Mg_xO_2$. It will be investigated if the derived formulas for the chemical potential can explain the measured thermopowers in combination with the TICR approximation. This means that the obtained chemical potentials (4.15), (4.42) and (4.43) should be put in the TICR approximation (2.47) and that the resulting expression should be fitted to the experimental data by adjusting the coefficients in the Taylor series. However, fitting such an infinite number of parameters is obviously not practicable. Instead, only the first two terms of

the Taylor series should be considered. In addition, the replacement of chromium by magnesium as well as the substitution of rhodium later leads to a hole-doping in the t_{2g} band (cf. section 1.2). For this kind of doping the upper band edge is important in contrast to the lower one which was described in (4.1) for electron-like doping. In order to apply the previously discussed framework, the signs of all energies should therefore be inverted. This leads to the density of states to be given by

$$\rho(\varepsilon) = (\rho_0 - \rho_1 \varepsilon) \cdot \Theta(-\varepsilon)\,. \tag{4.46}$$

Furthermore, since the lower band edge was neglected, the density of states can not be normalized with respect to the orbitals contributing to the band. Since the particle number constraint (4.2) can be scaled arbitrarily, only two of the parameters in (4.46) and the doping are independent. Thus only the normalized doping y and the parameter ratio r can be adjusted. They are defined by

$$y = \frac{\mathrm{x}}{\rho_0}, \qquad r = \frac{\rho_1}{\rho_0}\,. \tag{4.47}$$

When measuring the thermopower of doped $CuCrO_2$ [29] (cf. Fig. 4.8) the data for low doping does not seem to show a linear regime as clearly as doped $CuRhO_2$ (cf. Fig. 1.3). However, for intermediate values of the doping a trend towards a linear region is visible above $T = 600\,\mathrm{K}$. Since this temperature is very high the results of the lowest doped sample can be interpreted as a linear behavior, but with an even increased temperature $T = 900\,\mathrm{K}$ which served as expansion temperature $\tilde{T}$. Therefore the region where the parameters can be adjusted to the determined formulas should be restricted to values above the former temperatures. Moreover, to account for the strong noise the samples are showing the offset and linear term of the thermopower was adjusted by considering the quantities

$$\frac{TS(T) - \bar{T}S(\bar{T})}{T - \bar{T}} \qquad \text{with} \qquad \bar{T} = 700\,\mathrm{K}\,, \tag{4.48}$$

since they do not depend on the E_0 parameter of the TICR. This parameter was then adjusted by an additional fit. In calculating the exact solution by numerics afterwards the results can then be compared to the data points at lower temperatures. Note that already when the data was first investigated [29] samples with large doping where proven to be contaminated by the forming of a spinel phase. Therefore mainly the data for the low and intermediate doping as shown in Fig. 4.8 will be addressed.

Adjusting the parameters in (4.47) while comparing the experimental values to those obtained by the approximation for high temperatures in section 4.2 gives already reasonable parameters (cf. Tab. 4.1), in contrast to those for low temperatures. That would mean for this material the temperature scale would be very low although it is believed to be strongly correlated. Nevertheless, adjusting the parameters for the formula of the APLD from section 4.3 differ from these. At a closer look this is due to the fact, that the obtained parameters of the APLD would lead to a breakdown temperature T_P close to

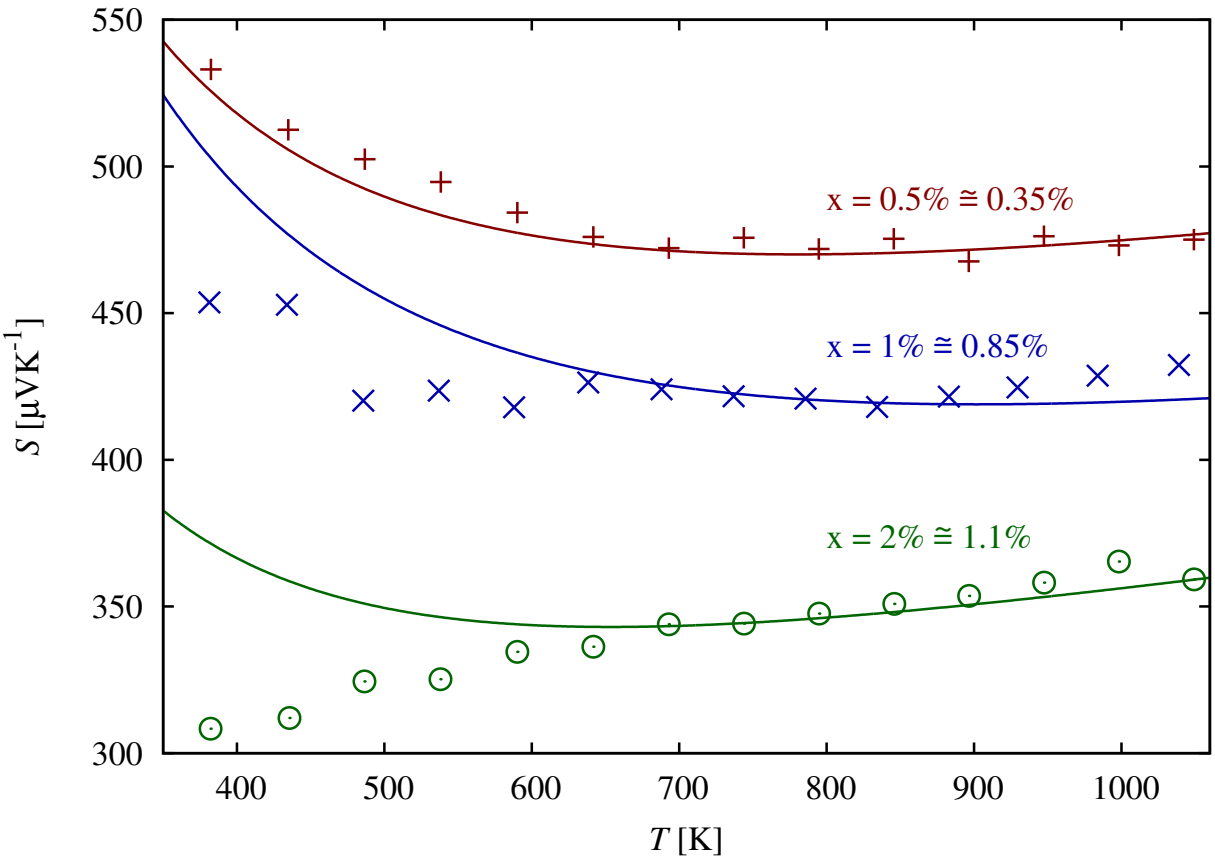

Figure 4.8: Comparison of the thermopower of $CuCr_{1-x}Mg_xO_2$ given by experimental data (points) according to [29, 151] to the one obtained from the parameters of the density of states for values of the determined doping of x = 0.35%, 0.85% and 1.1% respectively for the nominal doping x = 0.5%, x = 1% and x = 2%. The TICR parameter E_0 has been adjusted to the different doping values.

the considered one. Therefore a larger expansion temperature $T_0 = \mu\,(2k_\mathrm{B})^{-1}$ has to be considered. However, with this expansion temperature the simplification made after (4.34) would not hold any more. Thus, it requires to take the zeroth order $dx(k_\mathrm{B}T)$ of the APLD in (4.22) into account, which is proportional to $d_1(\nu_0)$ for the density of states in (4.46). With these modifications the results coincide with those obtained from the high temperature approximation.

While the results of the TICR parameter $E_0 \approx 100\,\mathrm{meV}$ are close to those reported for doped manganites, but with opposite signs since they are electron-doped [20, 98], the slope ρ_1 seems to dominate the effective density of states for this material. This is in agreement with a previous first principle study [29]. Furthermore, the results exhibit a strong increase of both parameters for the highest doped samples which fall in the range where the formation of a secondary spinel or CuO phase was previously reported [29] as

x [%]	ρ_0 $[(\mathrm{keV})^{-1}]$	ρ_1 $[(\mathrm{eV})^{-2}]$	r $[(\mathrm{eV})^{-1}]$	y [meV]	E_0 [meV]	$\tilde{\mathrm{x}}$ [%]
0.5	175	35	200	28.6	131	0.35
1.0	141	28.3	200	70.7	153	0.85
2.0	220	44	200	91	112	1.10
3.0	608	122	200	49.3	58.2	0.60
4.0	823	165	200	48.6	51.9	0.59
5.0	1180	236	200	42.4	36.7	0.51

Table 4.1: Parameters of the effective density of states ρ_0, ρ_1 as determined by a fit of the thermopower of (2.47) with (4.11) to the experimental values of $CuCr_{1-x}Mg_xO_2$ given for the values of the nominal doping x as extracted from the fitting parameters y, r and E_0. In addition the deduced effective charge carrier density $\tilde{\mathrm{x}}$ is shown too.

mentioned above.

However, the other samples exhibit some variations for the parameters too: Although they show a clear common parameter ratio $r = 200\,(\mathrm{eV})^{-1}$ the value for the normalized doping y still varies. During the first investigation [29] a similar issue was observed since the targeted nominal doping,

$$\mathrm{x} = 0.5\%,\ 1\%,\ 2\%\,, \tag{4.49}$$

did not succeed due to the mentioned forming of the spinels. Therefore, in that study statistical electron diffraction spectroscopy (EDS) was used to determine the change of the size of the unit cell. From their results, more reliable values can be obtained [151] leading to quite different doping values

$$\tilde{\mathrm{x}}_{\mathrm{EDS}} = 0.2\%,\ 0.6\%,\ 1.1\%\,. \tag{4.50}$$

Similarly, this encourages adjusting the doping in the present method to find the effective charge carrier density. This issue and its solution is not only known for doped $CuCrO_2$, but has been addressed for several other manganites, too [98]. However, since the doping values can only be obtained from (4.47) if the parameters of the density of states are known, one sample should be picked in order to calibrate the others. If the most reliable value of the reported EDS data $\tilde{\mathrm{x}}_{\mathrm{EDS}} = 1.1\%$ is used for the nominal one of $\mathrm{x} = 2\%$ the parameters of the density of states,

$$\rho_{0,B} = 0.121\,(\mathrm{eV})^{-1}, \qquad \rho_{1,B} = 24.2\,(\mathrm{eV})^{-2}\,, \tag{4.51}$$

coincide for all low doped samples for doping values of

$$\tilde{\mathrm{x}} = 0.35\%,\ 0.85\%,\ 1.1\%\,, \tag{4.52}$$

which are within the error margins of those suggested from the EDS measurements. Furthermore, if the charge carrier concentration is calculated for the higher doped samples a decrease is obtained, indicating again the mentioned problems in sample preparation.

Formula	x [%]	r [$(\mathrm{eV})^{-1}$]	y [meV]	E_0 [meV]
μ_P	1	3.5	4.8	33
μ_{Pq}	1	3.1	4.6	31
μ_{P-}	1	-	2.4	6.1
μ_P	4	3.4	6.0	11
μ_{Pq}	4	3.4	6.0	11
μ_{P-}	4	-	3.1	-14
μ_P	10	3.4	21	36
μ_{Pq}	10	2.5	19	32
μ_{P-}	10	-	13	17

Table 4.2: Stationary points of fitting the thermopower of (2.47) with (4.26), (4.38), (4.42) and (4.42) to the experimental data of $CuRh_{1-x}Mg_xO_2$ in the region where an AFL behavior is observed.

The calculation of the thermopower using the exact numerical solution leads to good agreement between theory and experiment as can be seen in Fig. 4.8. Additionally, the hyperbolic offset caused by the TICR parameter seems to describe the increase at low temperature and doping, while the agreement is lost below $T \approx 600\,\mathrm{K}$ for intermediate doping values. This might be due to a breakdown of the TICR, but surprisingly coincides with the Boltzmann breakdown temperatures for these samples $T_B = 349\,\mathrm{K},\ 565\,\mathrm{K},\ 644\,\mathrm{K}$. These values confirm the placement of the observed behavior in the region of the phase diagram where the AFL by the high temperature approximation can be found, too.

4.6 Application to the Delafossite $CuRhO_2$

As mentioned in the introduction, the doped band insulator $CuRhO_2$ shows a clear linear behavior of the thermopower with respect to temperature. However, the adjustment of the parameters in the derived formulas to the measurements of $CuRh_{1-x}Mg_xO_2$ [19] shows a different picture than in the case of the doped Mott-insulator $CuCrO_2$: On the one hand, a blind fit of the low temperature expansion (4.4) in combination with the TICR (2.47) would give negative discontinuities due to the observed offset in the thermopower. For the high temperature one (4.15) on the other hand, both the parameter ratio r and normalized doping y varies strongly between the samples, taking even negative values for the highest doped material for the former quantity. Therefore, the observed behavior can not be explained by these approximations. Nevertheless, adjusting the parameters in the formula obtained by the APLD with the simplification stated after (4.34) leads to more consistent results.

In comparing the results produced by a fit using the formula of the APLD with the expansion temperature (4.34) (cf. Tab. 4.2), the values of the parameter of the TICR $E_0 \approx 30\,\mathrm{meV}$ are in agreement for the lowest and highest doped samples and fall in a region similar to those reported for manganites [19, 98], too. Furthermore, the results of

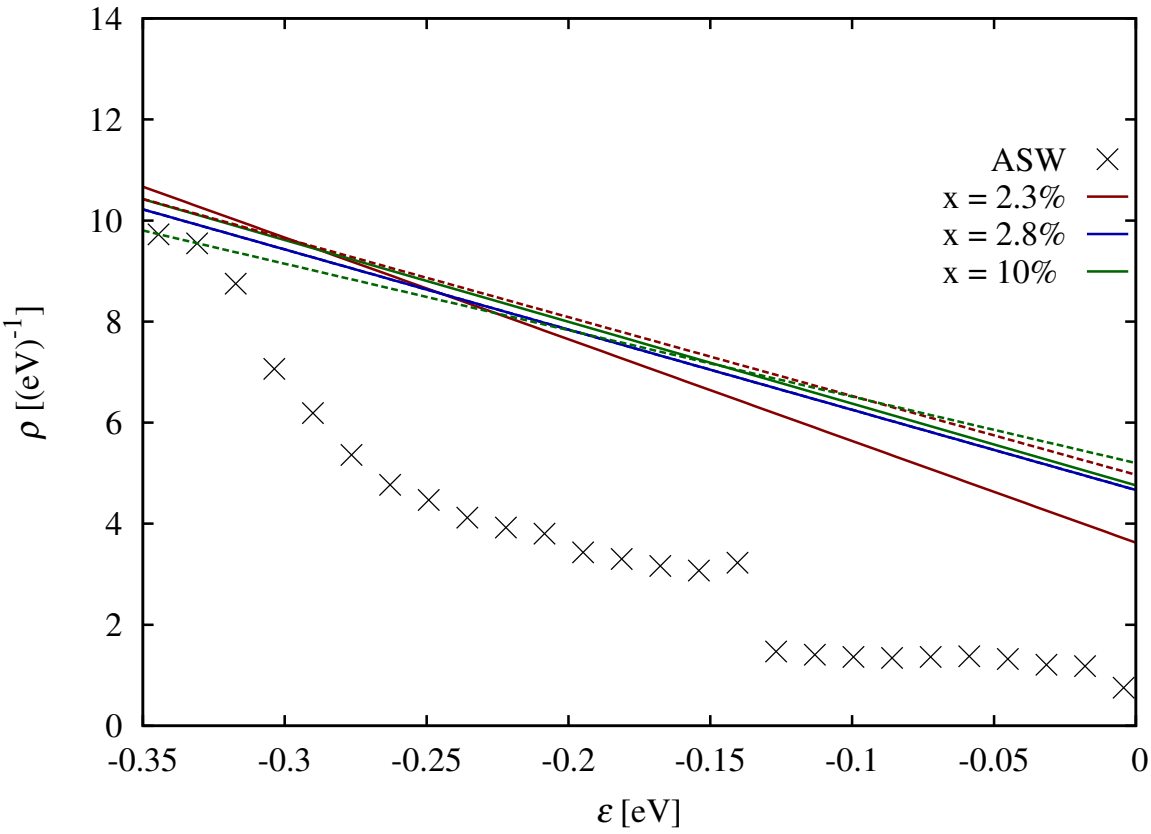

Figure 4.9: Density of states of $CuRh_{1-x}Mg_xO_2$ as given by the augmented spherical wave method (ASW) [19] and their shape as determined by a fit to the exact form (4.26) (solid) and quadratic expansion (4.42), (4.43) (dashed) within the APLD for different values of the doping of x = 2.3%, 2.8% and 10%.

the expansion for vanishing parameter ratio (4.38) gives values similar to those obtained from the quadratic expansion and from fitting the full solution (4.26). Again the parameter ratios found are close, while the values of the effective doping vary. Therefore the doping can be adjusted where the results of the parameters of the density of state coincide for doping values of

$$\mathrm{x} = 2.3\%,\ 2.8\%,\ 10\%\,. \tag{4.53}$$

With these values of the doping, all samples give therefore rise to the same parameters of the density of states of

$$\rho_{0,P} = 4.7\,(\mathrm{eV})^{-1}, \qquad \rho_{1,P} = 16\,(\mathrm{eV})^{-2}\,. \tag{4.54}$$

These results of the APLD are close to those obtained by first principle studies (cf. Fig. 4.9). The obtained parameters place the largest doped sample of this material in the phase diagram (cf. Fig. 4.6) precisely in the narrow area of the validity range of the AFL by APLD,

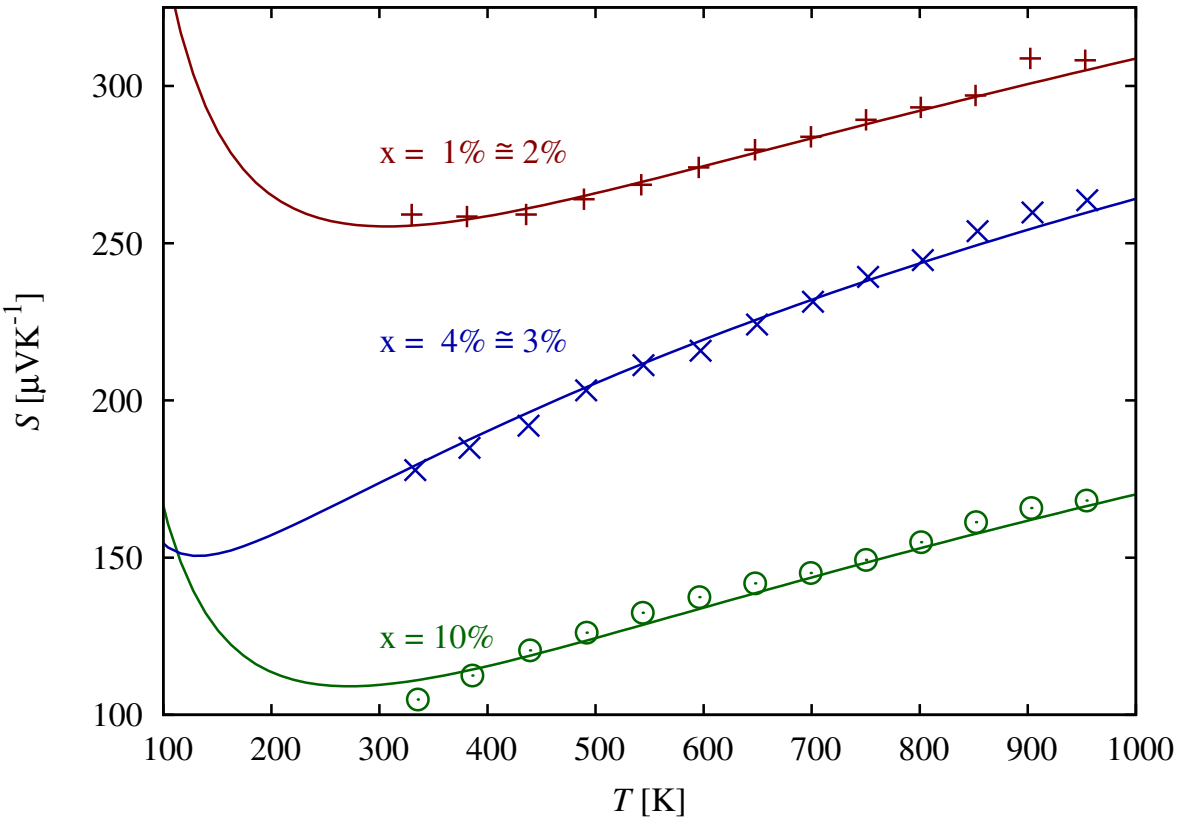

Figure 4.10: Comparison of the thermopower of $CuRh_{1-x}Mg_xO_2$ given by experimental data (points) to the one obtained from the parameters of the density of states for values of the doping of x = 2%, 3% and 10%. The TICR parameter E_0 has been adjusted to the different doping values.

while the lowest doped samples are closer to the region described by the high temperature approximation. This is further supported by the fact that the Boltzmann breakdown temperature for the largest doped sample $T_B(\mathrm{x} = 10\%) = 1316\,\mathrm{K}$ is larger than the one considered while the expansion temperature of the APLD $T_0(\mathrm{x} = 10\%) = 653\,\mathrm{K}$ lies within the region where the linear behavior is observed. Therefore the observed AFL can be understood as the remains of a broader manifestation for larger discontinuity. Compared to doped $CuCrO_2$ this material exhibits therefore a discontinuity enhanced thermopower although larger doping values were considered. Furthermore, the recalculation of the thermopower using the exact solution shows an extraordinary good agreement (cf. Fig. 4.10). At low temperature the hyperbolic offset E_0 of the thermopower dominates the theoretical behavior for this material too. Nevertheless, since the data does not show a strong upturn this rather indicates the breakdown of the TICR in agreement with the discussion in section 2.3. However, a slight upturn can be found for the lowest doped sample which compared to the intermediate one has a larger E_0 constant. Since interaction effects are ex-

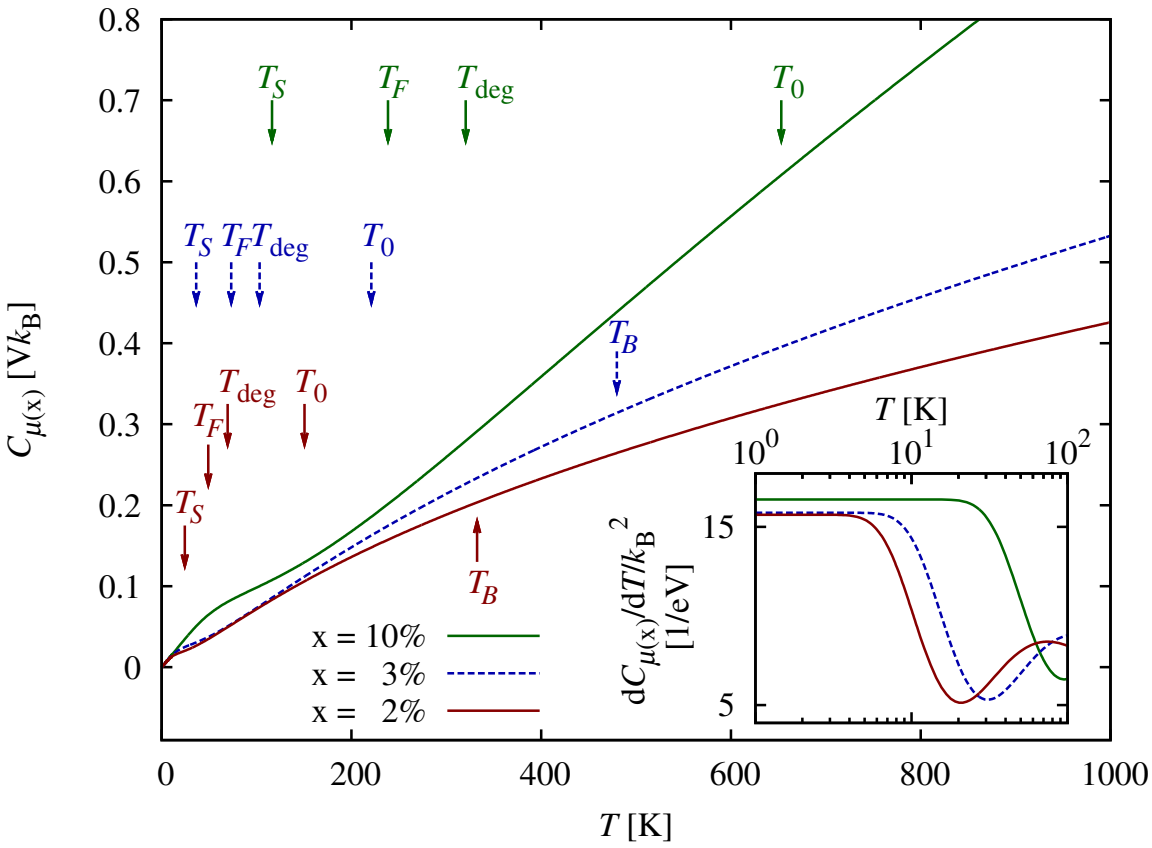

Figure 4.11: Specific heat of $CuRh_{1-x}Mg_xO_2$ and its derivative with respect to temperature (inset) given by the calculation with the parameters of the density of states from (4.54) for values of the doping x = 2%, 3% and 10%. The curves show a transition between a Fermi liquid and an apparent Fermi liquid indicated by an inflexion point. The arrows indicate the position of the characteristic (breakdown) temperatures for the different doping values.

pected to be negligible due to nearly filled bands, this might arise from scattering processes caused by a larger disorder in this sample which could explain the insulating behavior at very low temperatures [19], too.

From the parameters of the density of state further quantities like the specific heat can be determined (cf. Fig. 4.11). Since the calculation of the specific heat is not dependent on the TICR approximation a Fermi liquid behavior can be observed at very low temperatures. Nevertheless, for low doping the effective mass gets renormalized in comparison to calculations in which the discontinuity is neglected. This phase breaks down at a temperature which decreases with decreasing doping, in agreement with the expected insulating behavior for zero doping. However, the breakdown temperatures are obviously not well described by the Fermi temperature T_F, but seem to occur at temperatures somewhat below the analytically introduced smaller breakdown temperature T_S. In the vicinity of this

temperature a peak in the derivative of the specific heat is found (cf. inset of Fig. 4.11). It should be observable in experiments, in particular for low doping. Above the transition area, around the degeneracy temperature T_{deg}, a linear region emerges which extends to T_0, where the chemical potential has left the band, and for large doping even beyond. Note that the difference between the apparent effective mass and the bare one exceeds those usually expected from interaction effects obtained using the slave-boson saddle-point approximation applied to a nearly filled band [152]. At higher temperatures for the two lower doped samples, the slope gradually reaches a slightly smaller value, forming another linear region above the breakdown temperature of the high temperature approximation T_B. This region is described by the AFL in the high temperature approximation. Under an increase of the doping, the APLD replaces the high temperature approximation as the valid approximation at intermediate temperature. In this way the transition from the AFL in the high temperature approximation to the one given by the APLD is visible. This can be seen in Fig. 4.6 too, where an expansion around $\tilde{T} = 800\,\mathrm{K}$ was considered and the difference of the chemical potential at a temperature $T = 400\,\mathrm{K}$ was studied. The transition occurs therein when moving upwards, respectively increasing the normalized doping $y = x/\rho_0$, along the line for $r = \rho_1/\rho_0 = 3.4\,(\mathrm{eV})^{-1}$. Since the transition temperatures T_0 for the different doping are always lower than the expansion temperature $\tilde{T}$ the APLD (4.26) remains valid.

4.7 Summary and Outlook

In summary the density of states of the delafossites was described by a Taylor series with a dominant zero order term due to their underlying perturbed two-dimensional structure. Furthermore, since the considered materials were only slightly doped, this series was placed around the band edge. Thereby paying respect to the fact, that at intermediate temperature the chemical potential has left the band and therefore the region at the band edge provides the largest values of the Fermi function, where states still exists.

With this simplification of those materials Sommerfeld expansion and Boltzmann approximation could be formulated as expansions of the polylogarithm. On the one hand, the low temperature expansion showed a Fermi liquid behavior which may extend up to room temperature for dominant discontinuity and large doping. On the other hand, we obtained an AFL behavior already from the high temperature expansion. This behavior is not only characterized by a non-vanishing term of the chemical potential, which is linear in temperature, but also exhibits the same qualitative doping dependence as the Heikes formula in the low doping regime. Therefore it showed that this famous formula might be applied even to semi-conductors in some cases, although the interpretation of extracted quantities changes. Moreover, within this framework we were able to obtain breakdown temperatures for both cases. These temperatures showed a gap between the application range of these approximations which even broadens for a dominant discontinuity.

In order to access the missing temperature range, we developed the APLD which ap-

proximates in lowest order the density of states by its value at the thermal energy $k_{\mathrm{B}}T$, if only the first two terms of the Taylor series are considered. By this approximation we were able to specify a characteristic temperature where another AFL behavior can be observed, if only a discontinuity is present. This temperature increases with perturbations to the two-dimensionality of the system before the AFL region finally breaks down. In addition, the doping dependence of the chemical potential and therefore of the thermopower in the TICR approximation would differ from the one known from the Heikes formula around this temperature. Furthermore, due to the interpretation of this approximation, which we gave in section 2.3, this scheme should be valid within the validity range of the APLD.

While the high temperature approximation was sufficient to explain the thermopower of doped $CuCrO_2$, the APLD was needed for the interpretation of the doped delafossite $CuRhO_2$. Thereby, we could make a contribution to the pressing question of the real amount of charge carriers by assuming the same density of states for each sample of the materials. Moreover, since we obtained an effective density of states we could calculate the specific heat for the latter material, showing distinguishing features which might motivate further experiments.

Chapter 5

Conclusion

Motivated by the findings of the delafossites where an apparent Fermi liquid behavior was measured around room temperature, i.e. a linear thermopower and quadratic resistivity with respect to temperature, we addressed the question, how to access thermodynamic properties as well as the thermopower in temperature regions insufficiently covered so far.

In order to access quantities which are dependent on temperature within the DMRG framework we started from the ancilla approach where a single thermal quantum state can describe the system at a specific temperature. However, in order to target thermodynamic expectation values we could successfully demonstrate that enlarging the Hilbert space in this technique is not necessary. Instead, we proposed to use a thermal state, which we could generate in different ways:

On the one hand, we used the exactly known state of a non-interacting system, which could successfully be implemented in the DMRG framework. On the other hand, we generated an approximation to this state by taking the ground state of the original Hamiltonian, which was perturbed by both on-site disorder and disordered hopping parameters. Both showed a similar picture when calculating the overlap amplitudes of the generated state with the many-body eigenstates of the Hamiltonian. These overlap amplitudes resemble roughly an exponential decay with respect to the many-body energies of the system as is necessary for a thermal state. Nevertheless, for finite interaction strength stochastic sampling over different trial states was still necessary. In case of the thermal state of the non-interacting system we showed that the exploitation of the freedom of its arbitrary internal phases leads to surprisingly good results, even for large interaction strength at low temperatures. Furthermore, we proposed that with this technique it should be possible to access the thermopower, which can be applied to the delafossites if the DMRG is improved to access higher dimensional systems.

Since these materials are usually composed by connected layers, we focused on the effects of a density of states governed by the first terms of a Taylor series too. Thereby, we were able to place Sommerfeld expansion and Boltzmann approximation in the framework of using polylogarithm and obtained better breakdown criteria. Enlarging the application region of the latter approximation, we developed the APLD which enables to cover the

complete temperature region above the degeneracy temperature where the chemical potential leaves the band. Especially, for a dominant discontinuity in the density of states like in a two-dimensional system this approximation could be interpreted by replacing the energy dependent density of states by its value at the thermal energy. Furthermore, such a dominant discontinuity enlarges the validity range of this approximation scheme even further, covering the full temperature range for an unperturbed two-dimensional system.

These techniques enabled us to investigate the thermopower of doped $CuCrO_2$ and doped $CuRhO_2$ within the TICR approximation, which we could interpret by the non-resonant level model. In the study we were not only able to extract the parameters of a simplified density of states of these materials but to contribute to the question of the real charge carrier density too. In addition, we showed that while the former material can be understood in a Boltzmann picture where the lower tail of the Fermi function dominates the properties, the latter exemplifies another situation which is governed by the upper tail and which is only observable due to the dominating discontinuity at the band edge. Both situations lead to a quasi linear behavior of the thermopower, explaining the observed AFL behavior whose effects we suggested should be measurable in the specific heat as well.

Appendix

Polylogarithms and their expansion results at low temperature

In this chapter, the polylogarithms are defined by the integral which occurred in section 2.2 and which properties lead to the development of the approximation introduced in section 4.3. Some mathematical properties are derived afterwards including an inversion formula for real arguments. In the following, this formula allows to obtain the result of Sommerfeld expansion when the formalism is applied on the physical constraint of fixed particle number. In addition, it is shown, that the specific heat can exactly be determined in the grand canonical ensemble, while the low temperature approximation is needed for the canonical one.

When considering the doping constraint (4.2) and the density of states as series of powers s the following integrals appear:

$$\mathrm{Li}_{s+1}(z) = -\frac{1}{\Gamma(s+1)} \int_0^\infty x^s \, f\Big(x - \ln(-z)\Big) \, \mathrm{d}x \,, \tag{A.1}$$

where $f(x) = (1 + \mathrm{e}^x)^{-1}$ denotes the Fermi function (2.18) and $\mathrm{Re}(s) > -1$ as well as $z \notin \{x \in \mathbb{R} \,|\, x \geq 1\}$ are assumed for reasons of convergence. The functions Li_{s+1} defined in (A.1) are called the polylogarithm [153] of order $s+1$ and are illustrated for the first integer orders in Fig. 4.2 on page 66. It is easily shown that they fulfill a recursion relation with respect to their orders via their derivatives:

$$\frac{\partial \, \mathrm{Li}_{s+1}(z)}{\partial z} = \frac{1}{\Gamma(s+1)} \int_0^\infty x^s \, f'\Big(x - \ln(-z)\Big) \, \mathrm{d}x \, \frac{1}{z} \tag{A.2}$$

$$= \frac{1}{z\Gamma(s+1)} \left[x^s \, f\Big(x - \ln(-z)\Big) \Big|_0^\infty - s \int_0^\infty x^{s-1} \, f\Big(x - \ln(-z)\Big) \, \mathrm{d}x \right] \tag{A.3}$$

$$= -\frac{1}{z\Gamma(s)} \int_0^\infty x^{s-1} \, f\Big(x - \ln(-z)\Big) \, \mathrm{d}z = \frac{\mathrm{Li}_s(z)}{z} \,, \tag{A.4}$$

where $f'(x)$ denotes the derivative of the Fermi function. In addition, this recursion relation

means that all these functions share a similar behavior around the origin, i.e.

$$\lim_{z\to 0} \mathrm{Li}_s(z) = -\frac{1}{\Gamma(s)} \lim_{z\to 0} \int_0^\infty \frac{z x^{s-1}}{z - \mathrm{e}^x}\, \mathrm{d}x = 0\,, \tag{A.5}$$

$$\lim_{z\to 0} \frac{\partial\, \mathrm{Li}_s(z)}{\partial z} = \lim_{z\to 0} \frac{\mathrm{Li}_{s-1}(z)}{z} = \frac{1}{\Gamma(s-1)} \int_0^\infty x^{s-2}\, \mathrm{e}^{-x}\, \mathrm{d}x = 1\,. \tag{A.6}$$

More popular is the recursion formula in integral form through which the polylogarithm can alternatively be defined:

$$\mathrm{Li}_{s+1}(z) = \int_0^z \frac{\mathrm{Li}_s(x)}{x}\, \mathrm{d}x \tag{A.7}$$

The name of the functions derives from this recursion formula (A.7) and the fact, that one of these functions can be expressed by the logarithm. In particular, the function of first order represents this elementary function but at a shifted argument:

$$\begin{aligned}
\mathrm{Li}_1(z) &= -\int_0^\infty \frac{z}{z - \mathrm{e}^x}\, \mathrm{d}x && \text{(A.8)}\\
&= -\int_{z-1}^\infty \frac{z}{t(t-z)}\, \mathrm{d}t && \text{(A.9)}\\
&= -\int_{z-1}^\infty \left(\frac{1}{t-z} - \frac{1}{t}\right)\, \mathrm{d}t && \text{(A.10)}\\
&= -\ln \frac{t-z}{t}\bigg|_{z-1}^\infty && \text{(A.11)}\\
&= -\ln(1-z)\,, && \text{(A.12)}
\end{aligned}$$

where in (A.9) the integral was rewritten as dependent on the denominator, i.e. applying the substitution $t = z - \mathrm{e}^x$. If the known series expansion of the logarithm for $|z| < 1$ is combined with the recursion relation (A.7) a similar series expansion,

$$\mathrm{Li}_s(z) = \sum_{m=1}^\infty \frac{z^m}{m^s}\,, \tag{A.13}$$

can be found. This allows the extension of the definition of the polylogarithm to arbitrary order $s \in \mathbb{C}$. Furthermore, from (A.13) can be inferred, that these functions are real valued for real arguments $|x| < 1$ and real order $n \in \mathbb{R}$. While for real arguments larger unity $x \geq 1$, the polylogarithm functions exhibit a branch cut like the shifted logarithm (A.12), the functions can be evaluated at an arbitrary argument as well. Remarkably, if the argument is smaller than the negative unity $x < -1$ the value of those functions can be related to those with the inverse argument by the inversion formula [154]. In the

case of positive integer orders it simplifies so that only the logarithm enters besides the polylogarithm [153]:

$$\mathrm{Li}_n(-x) = 2\sum_{m=0}^{\lfloor n/2\rfloor} \mathrm{Li}_{2m}(-1)\,\frac{(\ln x)^{n-2m}}{(n-2m)!} - (-1)^n\,\mathrm{Li}_n\Big(-\frac{1}{x}\Big) \tag{A.14}$$

This can be proven using the integral version of the recursion formula (A.7):

$$\mathrm{Li}_{n+1}(-x) = \int_0^{-x} \frac{\mathrm{Li}_n(t)}{t}\,\mathrm{d}t \tag{A.15}$$

$$= \mathrm{Li}_{n+1}(-1^-) + \int_{1^+}^{x} \frac{\mathrm{Li}_n(-y)}{y}\,\mathrm{d}y \tag{A.16}$$

$$= \mathrm{Li}_{n+1}(-1^-) + 2\sum_{m=1}^{\lfloor n/2\rfloor} \mathrm{Li}_{2m}(-1)\,\frac{1}{(n-2m)!}\int_{1^+}^{x} \frac{(\ln y)^{n-2m}}{y}\,\mathrm{d}y$$
$$- (-1)^n \sum_{m=1}^{\infty} \frac{(-1)^m}{m^n}\int_{1^+}^{x} y^{-m-1}\,\mathrm{d}y \tag{A.17}$$

$$= \mathrm{Li}_{n+1}(-1^-) + 2\sum_{m=1}^{\lfloor n/2\rfloor} \mathrm{Li}_{2m}(-1)\,\frac{1}{(n-2m)!}\int_{0^+}^{\ln x} z^{n-2m}\,\mathrm{d}z$$
$$- (-1)^n \sum_{m=1}^{\infty} \frac{(-1)^m}{m^n}\int_{1^+}^{x} y^{-m-1}\,\mathrm{d}y \tag{A.18}$$

$$= \mathrm{Li}_{n+1}(-1^-) + 2\sum_{m=1}^{\lfloor n/2\rfloor} \mathrm{Li}_{2m}(-1)\,\frac{1}{(n-2m+1)!}(\ln x)^{n-2m+1}$$
$$- (-1)^{n+1} \sum_{m=1}^{\infty} \frac{(-1)^m}{m^{n+1}}\Big(x^{-m} - (1^-)^m\Big) \tag{A.19}$$

$$= \mathrm{Li}_{n+1}(-1) + 2\sum_{m=1}^{\lfloor n/2\rfloor} \mathrm{Li}_{2m}(-1)\,\frac{(\ln x)^{n+1-2m}}{(n+1-2m)!}$$
$$- (-1)^{n+1}\,\mathrm{Li}_{n+1}\Big(-\frac{1}{x}\Big) + (-1)^{n+1}\,\mathrm{Li}_{n+1}(-1) \tag{A.20}$$

$$= 2\sum_{m=0}^{\lfloor (n+1)/2\rfloor} \mathrm{Li}_{2m}(-1)\,\frac{(\ln x)^{n+1-2m}}{(n+1-2m)!} - (-1)^{n+1}\,\mathrm{Li}_{n+1}\Big(-\frac{1}{x}\Big), \tag{A.21}$$

where the substitutions $y = -t$ and $z = \ln y$ were used in (A.16) and (A.18) respectively. Note that for convergence reasons of the series 1^+ (1^-) denotes values slightly greater (smaller) than 1, i.e. $1 \pm \delta$, where the limit $\delta \to 0$ has been done in the penultimate line.

The initial condition is satisfied since

$$\mathrm{Li}_1(-x) = -\ln(1+x) = -\ln x - \ln\left(1 - \frac{1}{-x}\right) = -\ln x + \sum_{m=1}^{\infty} \frac{1}{m}\,(-x)^{-m}\,. \tag{A.22}$$

For a general density of states $\rho(\varepsilon)$ as decomposed in series of powers, these functions represent the integral of each summand appearing in the particle number condition (2.22). In the case of a Taylor series of only one band around the band edge[1] at ε_0 it takes the form

$$\rho(\varepsilon) = \sum_n \frac{\rho_n}{n!}(\varepsilon - \varepsilon_0)^n\,\Theta(\varepsilon - \varepsilon_0)\,\Theta(\varepsilon_0 + W - \varepsilon)\,, \tag{A.23}$$

where W denotes the bandwidth.

For such a density of states formula (A.14) can be used to derive the low temperature properties. The particle number density or doping x is determined by the sum over all states which are occupied as given by the Fermi function f. This sum becomes an integral as described in (2.19) which can be rewritten by the polylogarithm functions:

$$\mathrm{x} = \int \rho(\varepsilon)\, f\Big(\beta(\varepsilon - \mu)\Big)\ \mathrm{d}\varepsilon \tag{A.24}$$

$$= \int_{\varepsilon_0}^{\varepsilon_0 + W} \sum_n \frac{\rho_n}{n!}\,(\varepsilon - \varepsilon_0)^n \frac{1}{1 + \mathrm{e}^{\beta(\varepsilon-\mu)}}\ \mathrm{d}\varepsilon \tag{A.25}$$

$$= \sum_n \frac{\rho_n}{n!}\left[\int_{\varepsilon_0}^{\infty} - \int_{\varepsilon_0+W}^{\infty}\right](\varepsilon - \varepsilon_0)^n\,\frac{1}{1 + \mathrm{e}^{\beta(\varepsilon-\mu)}}\ \mathrm{d}\varepsilon \tag{A.26}$$

$$\begin{aligned} = \sum_n \frac{\rho_n}{n!}\beta^{-(n+1)}\Bigg[& \int_0^{\infty} x^n \frac{1}{1 + \mathrm{e}^{x + \beta(\varepsilon_0 - \mu)}}\ \mathrm{d}x \\ & - \int_0^{\infty} (x + \beta W)^n\,\frac{1}{1 + \mathrm{e}^{x + \beta(W + \varepsilon_0 - \mu)}}\ \mathrm{d}x\Bigg] \end{aligned} \tag{A.27}$$

$$\begin{aligned} = -\sum_n \rho_n \beta^{-(n+1)}\Bigg[& \mathrm{Li}_{n+1}(-\mathrm{e}^{\beta(\mu - \varepsilon_0)}) \\ & - \sum_{j=0}^{n} (\beta W)^{n-j} \binom{n}{j} \frac{j!}{n!}\,\mathrm{Li}_{j+1}(-\mathrm{e}^{\beta(\mu - W - \varepsilon_0)})\Bigg]\,, \end{aligned} \tag{A.28}$$

[1] In the calculation performed in this chapter, the zero point of energy will not be fixed in order to allow the application of the derived formulas to multiple bands. In this case, the band edge, bandwidth and the Taylor coefficients would acquire an additional band index. The summation over this index would be carried out at the sum of the Taylor series.

with the substitution $x = \beta(\varepsilon - \varepsilon_0)$ in the penultimate line. From the series representation of the polylogarithm (A.13) the second term in the formula above will be suppressed by the factor $\mathrm{e}^{-\beta W}$ for low temperatures. Therefore for a large bandwidth this term can be neglected. From the inversion formula (A.14) the remaining first term in (A.28) can be rewritten, yielding the result of Sommerfeld expansion in lowest order in temperature:

$$\begin{aligned}
\mathrm{x} \approx & -\sum_n \rho_n \beta^{-(n+1)} \left(2 \sum_{m=0}^{\lfloor (n+1)/2 \rfloor} \mathrm{Li}_{2m}(-1) \, \frac{\big(\beta(\mu-\varepsilon_0)\big)^{n+1-2m}}{(n+1-2m)!} \right. \\
& \left. - (-1)^{n+1} \sum_{m=1}^{\infty} \frac{(-1)^m}{m^{n+1}} \, \mathrm{e}^{-m\beta(\mu-\varepsilon_0)} \right) && \text{(A.29)} \\
= & -2 \sum_n \rho_n \beta^{-(n+1)} \left(\mathrm{Li}_0(-1) \, \frac{\beta^{n+1}}{(n+1)!} \, (\mu-\varepsilon_0)^{n+1} \right. \\
& \left. + \, \mathrm{Li}_2(-1) \, \frac{\beta^{n-1}}{(n-1)!} \, (\mu-\varepsilon_0)^{n-1} + \mathcal{O}(\beta^{n-3}) \right) && \text{(A.30)} \\
= & -2 \, \mathrm{Li}_0(-1) \sum_n \frac{\rho_n}{(n+1)!} \, (\mu-\varepsilon_0)^{n+1} \\
& - 2 \, \mathrm{Li}_2(-1) \, \beta^{-2} \sum_n \frac{\rho_n}{(n-1)!} \, (\mu-\varepsilon_0)^{n-1} + \mathcal{O}(\beta^{n-3}) && \text{(A.31)} \\
= & \int_0^{\mu} \rho(\varepsilon) \, \mathrm{d}\varepsilon + \frac{\pi^2}{6} \beta^{-2} \, \rho'(\mu) + \mathcal{O}(\beta^{-4}) \, , && \text{(A.32)}
\end{aligned}$$

where in the last line the series were identified as the Taylor series of the anti-derivative and the derivative of the density of states $\rho(\varepsilon)$ with respect to energy, and $\mathrm{Li}_0(-1) = -1/2$, as well as $\mathrm{Li}_2(-1) = -\pi^2/12$ were used. Expanding the chemical potential in this expression as power series with respect to temperature

$$\mu = \varepsilon_F + \mu_1 \, T - \varpi \, T^2 + \mu_3 \, T^3 + \mathcal{O}(T^4) \, , \tag{A.33}$$

and expanding the resulting expression further in a Taylor series, so that a comparison of the coefficients of the temperature dependence is possible leads to

$$\mathrm{x} = \int_0^{\varepsilon_F} \rho(\varepsilon) \, \mathrm{d}\varepsilon \, , \tag{A.34}$$

$$\mu_1 = \mu_3 = 0 \, , \tag{A.35}$$

$$\varpi = \frac{\pi^2}{6} {k_\mathrm{B}}^2 \frac{\rho'(\varepsilon_F)}{\rho(\varepsilon_F)} \, . \tag{A.36}$$

In order to evaluate the grand canonical potential, partial integration has to be applied to proceed afterwards as in the case of the particle number:

$$\Omega/M = -\beta^{-1} \ln Z_\mu/M \tag{A.37}$$

$$= \beta^{-1} \int_{-\infty}^{\infty} \rho(\varepsilon)\, \ln\Big[f\Big(-\beta(\varepsilon-\mu)\Big)\Big]\, \mathrm{d}\varepsilon \tag{A.38}$$

$$= \beta^{-1} \sum_n \frac{\rho_n}{n!} \int_{\varepsilon_0}^{\varepsilon_0+W} (\varepsilon-\varepsilon_0)^n\, \ln\Big[f\Big(-\beta(\varepsilon-\mu)\Big)\Big]\, \mathrm{d}\varepsilon \tag{A.39}$$

$$= \beta^{-1} \sum_n \frac{\rho_n}{n!} \frac{1}{n+1} \Big[W^{n+1} \ln\Big[f\Big(-\beta(\varepsilon_0+W-\mu)\Big)\Big]$$

$$- \beta \int_{\varepsilon_0}^{\varepsilon_0+W} (\varepsilon-\varepsilon_0)^{n+1}\, f\Big(\beta(\varepsilon-\mu)\Big)\, \mathrm{d}\varepsilon\Big] \tag{A.40}$$

$$\approx \sum_n \beta^{-(n+2)} \rho_n\, \mathrm{Li}_{n+2}(-\,\mathrm{e}^{\beta(\mu-\varepsilon_0)}) \tag{A.41}$$

$$= -\int_0^\mu \int_0^{\varepsilon'} \rho(\varepsilon)\, \mathrm{d}\varepsilon\, \mathrm{d}\varepsilon' - \frac{\pi^2}{6} \rho(\mu) {k_\mathrm{B}}^2 T^2 + \mathcal{O}(T^4) \tag{A.42}$$

The derivatives of this expression with respect to temperature determine the low temperature behavior of the entropy and the specific heat in the grand canonical ensemble:

$$\mathcal{S}_\mu/M = -\frac{\partial \Omega/M}{\partial T} = \frac{\pi^2}{3} \rho(\mu) {k_\mathrm{B}}^2 T \tag{A.43}$$

$$C_\mu/M = T \frac{\partial \mathcal{S}_\mu/M}{\partial T} = \frac{\pi^2}{3} \rho(\mu) {k_\mathrm{B}}^2 T \tag{A.44}$$

For an accurate calculation of these quantities in the canonical ensemble the free energy should be determined which can be found from the grand canonical potential by a Lagrange transformation. There the chemical potential is again given by (A.34). The free energy F can therefore be obtained as

$$F/M = \Omega/M + \mu\, \mathrm{x} \tag{A.45}$$

$$= -\int_0^{\varepsilon_F} \int_0^{\varepsilon'} \rho(\varepsilon)\, \mathrm{d}\varepsilon\, \mathrm{d}\varepsilon' - \frac{\pi^2}{6} \rho(\varepsilon_F) {k_\mathrm{B}}^2 T^2 + \varepsilon_F\, \mathrm{x} + \mathcal{O}(T^4)\,. \tag{A.46}$$

Again the derivatives determine the entropy and specific heat in the canonical ensemble:

$$\mathcal{S}_\mathrm{x}/M = -\frac{\partial F/M}{\partial T} = \frac{\pi^2}{3} \rho(\varepsilon_F) {k_\mathrm{B}}^2 T \tag{A.47}$$

$$C_\mathrm{x}/M = T \frac{\partial \mathcal{S}_\mathrm{x}/M}{\partial T} = \frac{\pi^2}{3} \rho(\varepsilon_F) {k_\mathrm{B}}^2 T \tag{A.48}$$

This is the same result as if the chemical potential dependent on temperature is used in the specific heat of the grand canonical ensemble.

Acknowledgements

At the end of this thesis, I would thank the referees Prof. Dr. Fakher F. Assaad and Dr. Dietmar Weinmann as well as Prof. Dr. Peter Wölfle, Dr. Antoine Maignan and Prof. Dr. Raymond Frésard for the possibility to work on these interesting topics. In particular, I'm most grateful for the support of Prof. Dr. Raymond Frésard on the French and Ms. Hornik on the German side without whom this joint thesis would not have been possible. In accordance to this diplomatic act, which was gladly approved by Prof. Dr. Josette Travert, Prof. Dr. Lamri Adoui and Prof. Dr. Horst Hippler, I want to mention that the ordering of the title pages might differ due to administrative issues. For the idea of such a cooperation as well as his technical aid I want to specially show my gratitude to Dr. Peter Schmitteckert who acted as unofficial supervisor throughout the preparation of this thesis too. In addition, I wish to acknowledge the assistance of the Steinbuch Centre for Computing, the Institut für Kondensierte Materie and the Institut für Nanotechnologie who were so kind to let me use their computer clusters where the numerical calculation were processed. On the software side gfortran, g++, awk, pov-ray3.6, gnuplot and latex2ε were used as well as some internet resources, like www.leo.org and www.wikipedia.org. In order to create figures from published data, this data was extracted from figures in the publications mentioned in their captions. Furthermore, I feel obliged to the financial support of the Research Unit 960 "Quantum Phase Transitions", the French-German University and the ANR through NEWTOM (ANR-08-BLAN-0005-01). In particular, Dr. Christine Martin was very helpful in organizing the cooperation for the latter one as well as discussing the chemical side of the considered materials. Furthermore, I want to express my deepest thanks to our secretary Rose Schrempp and to my colleagues, in particular Dr. Alexander Braun, Dr. Johannes Reuther, Dr. Sam Carr and Dipl.-Phys. Stéphane Ngô Đinh at the Institut für Theorie der Kondensierten Materie (TKM), Dr. Emmanuel Guilmeau, Dr. Ulrike Lüders and Dr. Cédric de Vaulx at the Laboratoire de Cristallographie et sciences des Matériaux (CRISMAT), and Dr. Volker Eyert and Prof. Dr. Thilo Kopp from the Universität Augsburg for useful discussions on related topics. Last but not least I am indebted to my friends and family, especially to my cousin Francis Kremer, for their motivating support.

Bibliography

[1] C. de Vaulx, private communication (2009).

[2] S. L. "Strom aus Abwärme: Der thermoelektrische Generator von BMW" *Heise Autos* (2008).

[3] R. R. Furlong and E. J. Wahlquist "U.S. space missions using radioisotope power systems" *Nuclear News* **42** (5), 26-34 (1999).

[4] D. M. Rowe *Thermoelectrics Handbook: Macro to Nano* edited by D. M. Rowe (CRC Press, Boca Raton, 2006), pp. 1-4.

[5] G. V. Chester and A. Thellung "The Law of Wiedemann and Franz" *Proc. Phys. Soc.* **77** (5), 1005-1013 (1961).

[6] C. Kittel *Introduction to Solid State Physics* (John Wiley and Sons, New York, 1953), pp. 222, 307.

[7] M. Ohtaki, H. Koga, T. Tokunaga, K. Eguchi, and H. Arai "Electrical Transport Properties and High-Temperature Thermoelectric Performance of $(Ca_{0.9}M_{0.1})MnO_3$ (M = Y, La, Ce, Sm, In, Sn, Sb, Pb, Bi)" *J. Sol. State Chem.* **120** (1), 105-111 (1995).

[8] H. Ohta, S. Kim, Y. Mune, T. Mizoguchi, K. Nomura, S. Ohta, T. Nomura, Y. Nakanishi, Y. Ikuhara, M. Hirano, H. Hosono, and K. Koumoto "Giant thermoelectric Seebeck coefficient of a two-dimensional electron gas in $StTiO_3$" *Nature Materials* **6** (2), 129-134 (2007).

[9] G. S. Nolas, J. Sharp, and H. J. Goldsmid *Thermoelectrics* in *Springer Series in Materials Science* **45** (Springer, Berlin, 2001), pp. 191-207.

[10] A. Saramat, G. Svensson, A. E. C. Pamqvist, C. Stiewe, E. Mueller, D. Platzek, S. G. K. Williams, and D. M. Rowe "Large thermoelectric figure of merit at high temperature in Czochralski-grown clathrate $Ba_8Ga_{16}Ge_{30}$" *J. Appl. Phys.* **99** (2), 023708 [5 pages] (2006).

[11] X. F. Tang, L. D. Chen, T. Goto, and T. Hirai "Effects of Ce filling fraction and Fe content on the thermoelectric properties of Co-rich $Ce_yFe_xCo_{4-x}Sb_{12}$" *J. Mater. Res.* **16** (3), 837-842 (2001).

[12] H. Kuriyama, M. Nohara, T. Sasagawa, K. Takubo, T. Mizokawa, K. Kimura, and H. Takagi *High-temperature thermoelectric properties of Delafossite oxide $CuRh_{1-x}Mg_xO_2$ Proc. 25th Int. Conf. Thermoelectrics (Vienna)* (IEEE, Piscataway, 2006), p. 97.

[13] Y. Ono, K. Satoh, T. Nozaki, and T. Kajitani "Structural, Magnetic and Thermoelectric Properties of Delafossite-type Oxide, $CuCr_{1-x}Mg_xO_2$ ($0 \leq x \leq 0.05$)" *Jpn. J. Appl. Phys.* **46** (3A), 1071-1075 (2007).

[14] K. Hayashi, T. Nozaki, and T. Kajitani "Structure and High Temperature Thermoelectric Properties of Delafossite-Type Oxide $CuFe_{1-x}Ni_xO_2$ ($0 \leq x \leq 0.05$)" *Jpn. J. Appl. Phys.* **46** (8A), 5226-5229 (2007).

[15] T. Nozaki, K. Hayashi, and T. Kajitani "Thermoelectric Properties of Delafossite-Type Oxide $CuFe_{1-x}Ni_xO_2$ ($0 \leq x \leq 0.05$)" *J. Chem. Eng. Jpn.* **40** (13), 1205-1209 (2007).

[16] I. Terasaki, Y. Sasago, and K. Uchinokura "Large thermoelectric power in $NaCo_2O_4$ single crystals" *Phys. Rev. B* **56** (20), 12685-12687(R) (1997).

[17] D. Bérardan, E. Guilmeau, A. Maignan, and B. Raveau "In_2O_3:Ge, a promising n-type thermoelectric oxide composite" *Solid State Commun.* **146** (1), 97-101 (2008).

[18] Y. Tokura, Y. Taguchi, Y. Okada, Y. Fujishima, T. Arima, K. Kumagai, and Y. Iye "Filling Dependence of Electronic Properties on the Verge of Metal–Mott-Insulator Transitions in $Sr_{1-x}La_xTiO_3$" *Phys. Rev. Lett.* **70** (14), 2126-2129 (1993).

[19] A. Maignan, V. Eyert, C. Martin, S. Kremer, R. Frésard, and D. Pelloquin "Electronic structure and thermoelectric properties of $CuRh_{1-x}Mg_xO_2$" *Phys. Rev. B* **80** (11), 115103 [9 pages] (2009).

[20] M. Miclau, J. Hejtmanek, R. Retoux, K. Knizek, Z. Jirak, R. Fresard, A. Maignan, S. Hebert, M. Hervieu, and C. Martin "Structural and Magnetic Transitions in $CaMn_{1-x}W_xO_3$" *Chem. Mater.* **19** (17), 4243-4251 (2007).

[21] Y. Klein, S. Hébert, A. Maignan, S. Kolesnik, T. Maxwell, and B. Dabrowski "Insensitivity of the band structure of substituted $SrRhO_3$ as probed by Seebeck coefficient measurements" *Phys. Rev. B* **73** (5), 052412 [4 pages] (2006).

[22] M. Tanaka, M. Hasegawa, and H. Takei "Growth and Anisotropic Physical Properties of $PdCoO_2$ Single Crystals" *J. Phys. Soc. Jpn.* **65** (12), 3973-3977 (1996).

[23] S. Kremer and R. Frésard "Thermoelectric transport properties of an apparent Fermi liquid: Relation to an analytic anomaly in the density of states and application to hole-doped delafossites" *submitted to Ann. d. Phys.* [21 pages] (2011).

[24] Ph. de Clermont "Séance du 18 juillet 1873" *Bulletin de la Société chimique de Paris* **20** (2), 99 (1873).

[25] R. D. Shannon, D. B. Rogers, and C. T. Prewitt "Chemistry of Noble Metal Oxides. I. Syntheses and Properties of ABO_2 Delafossite Compounds" *Inorg. Chem.* **10** (4), 713-718 (1971);
C. T. Prewitt, R. D. Shannon, and D. B. Rogers "Chemistry of Noble Metal Oxides. II. Crystal Structures of $PtCoO_2$, $PdCoO_2$, $CuFeO_2$, and $AgFeO_2$" *Inorg. Chem.* **10** (4), 719-723 (1971);
D. B. Rogers, R. D. Shannon, and C. T. Prewitt "Chemistry of Noble Metal Oxides. III. Electrical Transport Properties and Crystal Chemistry of ABO_2 Compounds with the Delafossite Structure" *Inorg. Chem.* **10** (4), 723-727 (1971).

[26] K. Isawa *Oxide Thermoelectrics* edited by K. Koumoto (Research Signpost, Trivandrum, 2002), p. 213.

[27] S. Seki, Y. Yamasaki, Y. Shiomi, S. Iguchi, Y. Onose, and Y. Tokura "Impurity-doping-induced ferroelectricity in the frustrated antiferromagnet $CuFeO_2$" *Phys. Rev. B* **75** (10), 100403(R) [4 pages] (2007).

[28] J.-P. Doumerc, A. Wichainchai, A. Ammar, M. Pouchard, and P. Hagenmuller "On magnetic properties of some oxides with delafossite-type structure" *Mater. Res. Bull.* **21** (6), 745-752 (1986).

[29] A. Maignan, C. Martin, R. Frésard, V. Eyert, E. Guilmeau, S. Hébert, M. Poienar, and D. Pelloquin "On the strong impact of doping in the triangular antiferromagnet $CuCrO_2$" *Solid State Commun.* **149** (23), 962-967 (2009).

[30] M. Tinkham *Group theory and quantum mechanics* (McGraw-Hill, New York, 1964), pp. 86, 282.

[31] R. Seshadri, C. Felser, K. Thieme, and W. Tremel "Metal–Metal Bonding and Metallic Behavior in Some ABO_2 Delafossites" *Chem. Mater.* **10** (8), 2189-2196 (1998).

[32] H. Okabe, M. Matoba, T. Kyomen, and M. Itoh "Magnetic property and electronic structure of itinerant $Pd_xCo_yO_2$ magnets" *J. Appl. Phys.* **93** (10), 7258-7260 (2003).

[33] D. J. Singh "Electronic and thermoelectric properties of $CuCrO_2$: Density functional calculations" *Phys. Rev. B* **76** (8), 085110 [4 pages] (2007).

[34] V. Eyert, R. Frésard, and A. Maignan "On the Metallic Conductivity of the Delafossites $PdCoO_2$ and $PtCoO_2$" *Chem. Mater.* **20** (6), 2370-2373 (2008).

[35] V. Eyert, R. Frésard, and A. Maignan "Long-range magnetic order and spin-lattice coupling in delafossite $CuFeO_2$" *Phys. Rev. B* **78** (5), 052402 [4 pages] (2008).

[36] H. Usui, R. Arita, and K. Kuroki "First-principles study on the origin of large thermopower in hole-doped $LaRhO_3$ and $CuRhO_2$" *J. Phys. : Condens. Matter* **21** (6), 064223 [4 pages] (2009).

[37] S. Schmitt "Non-Fermi-liquid signatures in the Hubbard model due to van Hove singularities" *Phys. Rev. B* **82** (15), 155126 [12 pages] (2010).

[38] C. M. Varma, P. B. Littlewood, S. Schmitt-Rink, E. Abrahams, and A. E. Ruckenstein "Phenomenology of the Normal State of Cu-O High-Temperature Superconductors" *Phys. Rev. Lett.* **63** (18), 1996-1999 (1989).

[39] D. M. Newns, P. C. Pattnaik, and C. C. Tsuei "Role of Van Hove singularity in high-temperature superconductors : Mean field" *Phys. Rev. B* **43** (4), 3075-3084 (1991).

[40] J. A. Hertz "Quantum critical phenomena" *Phys. Rev. B* **14** (3), 1165-1184 (1976).

[41] F. Schwabel *Quantenmechanik für Fortgeschrittene* (Springer, Berlin, 1997).

[42] F. Schwabel *Statistische Mechanik* (Springer, Berlin, 2000).

[43] A. Altland and B. Simons *Condensed Matter Field Theory* (Cambridge University Press, Cambridge, 2010).

[44] G. D. Mahan *Many-particle physics* (Plenum Press, New York, 1990).

[45] H. Bluhm, N. C. Koshnick, J. A. Bert, M. E. Huber, and K. A. Moler "Persistent Current in Normal Metal Rings" *Phys. Rev. Lett.* **102** (13), 136802 [4 pages] (2009).

[46] L. P. Lévy, G. Dolan, J. Dunsmuir, and H. Bouchiat "Magnetization of Mesoscopic Copper Rings : Evidence for Persistent Currents" *Phys. Rev. Lett.* **64** (17), 2074-2077 (1990).

[47] V. Meden and U. Schollwöck "Persistent currents in mesoscopic rings : A numerical and renormalization group study" *Phys. Rev. B* **67** (3), 035106 [9 pages] (2003).

[48] R. A. Molina, D. Weinmann, and J.-L. Pichard "Interacting electron systems between Fermi leads : effective one-body transmissions and correlation clouds" *Eur. Phys. J. B* **48** (2), 243-247 (2005).

[49] P. Schmitteckert and U. Eckern "Phase coherence in a random one-dimensional system of interacting fermions : A density-matrix renormalization-group study" *Phys. Rev. B* **53** (23), 15397-15400 (1996).

[50] P. Schmitteckert, T. Schulze, C. Schuster, P. Schwab, and U. Eckern "Anderson Localization versus Delocalization of Interacting Fermions in One Dimension" *Phys. Rev. Lett.* **80** (3), 560-563 (1998).

[51] P. Schmitteckert, R. A. Jalabert, D. Weinmann, and J.-L. Pichard "From the Fermi Glass towards the Mott Insulator in One Dimension : Delocalization and Strongly Enhanced Persistent Current" *Phys. Rev. Lett.* **81** (11), 2308-2311 (1998).

[52] A. Wobst and D. Weinmann "Two interacting particles in a disordered chain IV : Scaling of level curvatures" *Eur. Phys. J. B* **10** (1), 159-167 (1999).

[53] D. Weinmann, P. Schmitteckert, R. A. Jalabert, and J.-L. Pichard "Delocalization effects and charge reorganizations induced by repulsive interactions in strongly disordered chains" *Eur. Phys. J. B* **19** (1), 139-156 (2001).

[54] R. A. Molina, P. Schmitteckert, D. Weinmann, R. A. Jalabert, G.-L. Ingold, and J.-L. Pichard "Residual conductance of correlated one-dimensional nanosystems : A numerical approach" *Eur. Phys. J. B* **39** (1), 107-120 (2004).

[55] P. Jordan and E. Wigner "Über das Paulische Äquivalenzverbot" *Z. Phys.* **47** (9), 631-651 (1928).

[56] J. M. Luttinger "An Exactly Soluble Model of a Many-Fermion System" *J. Math. Phys.* **4** (9), 1154-1162 (1963).

[57] A. Luther and I. Peschel "Calculation of critical exponents in two dimensions from quantum field theory in one dimension" *Phys. Rev. B* **12** (9), 3908-3917 (1975).

[58] F. D. M. Haldane "General Relation of Correlation Exponents and Spectral Properties of One-Dimensional Fermi Systems: Application to the Anisotropic $S = \frac{1}{2}$ Heisenberg Chain" *Phys. Rev. Lett.* **45** (16), 1358-1362 (1980).

[59] J. E. Hirsch and E. Fradkin "Effect of Quantum Fluctuations on the Peierls Instability: A Monte Carlo Study" *Phys. Rev. Lett.* **49** (6), 402-405 (1982).

[60] J. E. Hirsch and E. Fradkin "Phase diagram of one-dimensional electron-phonon systems. II. The molecular-crystal model" *Phys. Rev. B* **27** (7), 4302-4316 (1983).

[61] M. Hohenadler, H. Fehske, and F. F. Assaad "Dynamic charge correlations near the Peierls transition" *Phys. Rev. B* **83** (11), 115105 [8 pages] (2011).

[62] Q. Yuan, T. Nunner, and T. Kopp "Imperfect nesting and Peierls instability for a two-dimensional tight-binding model" *Eur. Phys. J. B* **22** (1), 37-42 (2001).

[63] N. Pavlenko and T. Kopp "Electron-phonon coupling in a two-dimensional inhomogeneous electron gas: consequences for surface spectral properties" *J. Phys.: Condens. Matter* **20** (39), 395203 [7 pages] (2008).

[64] C. N. Yang and C. P. Yang "One-Dimensional Chain of Anisotropic Spin-Spin Interactions. I. Proof of Bethe's Hypothesis for Ground State in a Finite System" *Phys. Rev.* **150** (1), 321-327 (1966);
C. N. Yang and C. P. Yang "One-Dimensional Chain of Anisotropic Spin-Spin Interactions. II. Properties of the Ground-State Energy Per Lattice Site for an Infinite System" *Phys. Rev.* **150** (1), 327-339 (1966).

[65] M. Karbach and G. Müller "Introduction to the Bethe Ansatz I" *Computers in Physics* **11** (1), 36-44 (1997);
M. Karbach, K. Hu, and G. Müller "Introduction to the Bethe Ansatz II" *Computers in Physics* **12** (6), 565-574 (1998);
M. Karbach, K. Hu, and G. Müller "Introduction to the Bethe Ansatz III" *arXiv:cond-mat/0008018v1* [11 pages] (2000).

[66] M. Takahashi *Thermodynamics of one-dimensional solvable models* (Cambridge University Press, Cambridge, 1999).

[67] I. N. Karnaukhov and A. A. Ovchinnikov "One dimensional strongly interacting Luttinger liquid of lattice spinless fermions" *arXiv:cond-mat/0110289v1* [4 pages] (2001).

[68] P. Schmitteckert and R. Werner "Charge-density-wave instabilities driven by multiple umklapp scattering" *Phys. Rev. B* **69** (19), 195115 [5 pages] (2004).

[69] F. F. Assaad and D. Würtz "Charge and spin structures in the one-dimensional *t-J* model" *Phys. Rev. B* **44** (6), 2681-2696 (1991).

[70] M. Ogata, M. U. Luchini, S. Sorella, and F. F. Assaad "Phase Diagram of the One-Dimensional *t-J* Model" *Phys. Rev. B* **66** (18), 2388-2391 (1991).

[71] H. v. Löhneysen, A. R. Roch, M. Vojta, and P. Wölfle "Fermi-Liquid Instabilities at Magnetic Quantum Phase Transitions" *Rev. Mod. Phys.* **79** (3), 1015-1075 (2007).

[72] M. Zacharias, P. Wölfle, and M. Garst "Multiscale quantum criticality: Pomeranchuk instability in isotropic metals" *Phys. Rev. B* **80** (16), 165116 [15 pages] (2009).

[73] P. Wölfle and E. Abrahams "Quasiparticles beyond the Fermi liquid and heavy fermion criticality" *arXiv:cond-mat/1102.3391v2* [5 pages] (2011).

[74] V. N. Popov and S. A. Fedotov "The functional-integration method and diagram technique for spin systems" *Sov. Phys. JETP* **67** (3), 535-541 (1988).

[75] A. J. Leggett *Granular Nanoelectronics* edited by D. K. Ferry (Plenum Press, New York, 1991), pp. 297-311.

[76] X. Waintal, G. Fleury, K. Kazymyrenko, M. Houzet, P. Schmitteckert, and D. Weinmann "Persistent Currents in One Dimension: The Counterpart of Leggett's Theorem" *Phys. Rev. Lett.* **101** (10), 106804 [4 pages] (2008).

[77] I. Affleck "Universal Term in the Free Energy at a Critical Point and the Conformal Anomaly" *Phys. Rev. Lett.* **56** (7), 746-748 (1986).

[78] C. M. Naón, M. J. Salvay, and M. L. Trobo "Conformal properties of one-dimensional quantum systems with long-range interactions" *Phys Rev. B* **72** (24), 245110 [4 pages] (2005).

[79] P. Drude "Zur Elektronentheorie der Metalle" *Ann. d. Phys.* **4** (11), 369-402 (1900).

[80] A. Rosch "Ist ein See von Elektronen immer eine Fermi-Flüssigkeit?" *Physik in unserer Zeit* **30** (3), 118-122 (1999).

[81] K. Kadowaki and S. B. Woods "Universal relationship of the resistivity and specific heat in heavy-fermion compounds" *Solid State Commun.* **58** (8), 507-509 (1986).

[82] Y. Maeno, K. Yoshida, H. Hashimoto, S. Nishizaki, S. Ikeda, M. Nohara, T. Fujita, A. P. Mackenzie, N. E. Hussey, J. G. Bednorz, and F. Lichtenberg "Two-Dimensional Fermi Liquid Behavior of the Superconductor Sr_2RuO_4" *J. Phys. Soc. Jpn.* **66** (5), 1405-1408 (1997).

[83] C. Urano, M. Nohara, S. Kondo, F. Sakai, H. Takagi, T. Shiraki, and T. Okubo "LiV_2O_4 Spinel as a Heavy-Mass Fermi Liquid: Anomalous Transport and Role of Geometrical Frustration" *Phys. Rev. Lett.* **85** (5), 1052-1055 (2000).

[84] S. Nakamae, K. Behnia, N. Mangkorntong, M. Nohara, H. Takagi, S. J. C. Yates, and N. E. Hussey "Electronic ground state of heavily overdoped non-superconducting $La_{2-x}Sr_xCuO_4$" *Phys. Rev. B* **68** (10), 100502(R) [4 pages] (2003).

[85] K. Miyake, T. Matsuura, and C. Varma "Relation between resistivity and effective mass in heavy-fermion and A15 compounds" *Solid State Comm.* **71** (12), 1149-1153 (1989).

[86] P. M. Chaikin and G. Beni "Thermopower in the correlated hopping regime" *Phys. Rev. B* **13** (2), 647-651 (1976).

[87] D. B. Marsh and P. E. Parris "High-temperature thermopower of $LaMnO_3$ and related systems" *Phys. Rev. B* **54** (23), 16602-16607 (1996).

[88] W. Koshibae, K. Tsutsui, and S. Maekawa "Thermopower in cobalt oxides" *Phys. Rev. B* **62** (11), 6869-6872 (2000).

[89] A. Maignan, D. Flahaut, and S. Hébert "Sign change of the thermoelectric power in $LaCoO_3$" *Eur. Phys. J. B* **39** (2), 145-148 (2004).

[90] S.-P. Kou and Z.-Y. Weng "Self-localization of holes in a lightly doped Mott insulator" *Eur. Phys. J. B* **47** (1), 37-46 (2005).

[91] P. Limelette, S. Hébert, H. Muguerra, R. Frésard, and C. Simon "Dual electronic states in thermoelectric cobalt oxide $[Bi_{1.7}Ca_2O_4]_{0.59}CoO_2$" *Phys. Rev. B* **77** (23), 235118 [5 pages] (2008).

[92] J. Hejtmánek, Z. Jirák, K. Knížek, M. Maryško, M. Veverka, and C. Autret "Valence and spin states in perovskites $LaCo_{0.95}M_{0.05}O_3$ (M = Mg, Ga, Ti)" *J. Magn. Magn. Mater.* **320** (14), e92-e95 (2008).

[93] M. Uchida, K. Oishi, M. Matsuo, W. Koshibae, Y. Onose, M. Mori, J. Fujioka, S. Miyasaka, S. Maekawa, and Y. Tokura "Thermoelectric response in the incoherent transport region near Mott transition: the case study of $La_{1-x}Sr_xVO_3$" *Phys. Rev. B* **83** (16), 165127 [5 pages] (2011).

[94] A. Branschädel, private communication (2011).

[95] M. Büttiker, Y. Imry, R. Landauer, and S. Pinhas "Generalized many-channel conductance formula with application to small rings" *Phys. Rev. B* **31** (10), 6207-6215 (1985).

[96] P. Hu "One-dimensional quantum electron system under a finite voltage" *Phys. Rev. B* **35** (8), 4078-4081 (1987).

[97] D. Segal "Thermoelectric effect in molecular junctions: A tool for revealing transport mechanisms" *Phys. Rev. B* **72** (16), 165426 [7 pages] (2005).

[98] R. Frésard, S. Hébert, A. Maignan, L. Pi, and J. Hejtmanek "Modeling of the thermopower of electron-doped manganites" *Phys. Lett. A* **303** (2), 223-228 (2002).

[99] K. Durczewski and M. Ausloos "Inelastic-phonon-scattering effect on the behavior of the thermoelectric power of metals" *Phys. Rev. B* **49** (18), 13215 [13218] (1994).

[100] K. Durczewski and M. Ausloos "Theory of the thermoelectric Seebeck coefficient: The case of phonon scattering for a degenerate free-electron gas" *Phys. Rev. B* **53** (4), 1762-1772 (1996).

[101] O. A. Petrenko, G. Balakrishnan, M. R. Lees, D. McK. Paul, and A. Hoser "High-magnetic-field behavior of the triangular-lattice antiferromagnet $CuFeO_2$" *Phys. Rev. B* **62** (13), 8983-8988 (2000).

[102] T. Okuda, Y. Beppu, Y. Fujii, T. Onoe, N. Terada, and S. Miyasaka "Specific heat of delafossite oxide $CuCr_{1-x}Mg_xO_2$ ($0 \leq x \leq 0.03$)" *Phys. Rev. B* **77** (13), 134423 [5 pages] (2008).

[103] Q.-J. Liu, Z.-T. Liu, and L.-P. Feng "Theoretical calculations of mechanical, electronic, chemical bonding and optical properties of delafossite $CuAlO_2$" *Physica B* **405** (8), 2028-2033 (2010).

[104] K. Behnia, D. Jaccard and J. Flouquet "On the thermoelectricity of correlated electrons in the zero-temperature limit" *J. Phys.: Condens. Matter* **16** (28), 5187-5198 (2004).

[105] V. S. Oudovenko and G. Kotliar "Thermoelectric properties of the degenerate Hubbard model" *Phys. Rev. B* **65** (7), 075102 [6 pages] (2002).

[106] B. S. Shastry "Sum rule for thermal conductivity and dynamical thermal transport coefficients in condensed matter" *Phys. Rev. B* **73** (8), 085117 [16 pages] (2006).

[107] J. O. Haerter, M. R. Peterson, and B. S. Shastry "Strong Correlations Produce the Curie-Weiss Phase of Na_xCoO_2" *Phys. Rev. Lett.* **97** (22), 226402 [4 pages] (2006).

[108] M. R. Peterson, B. S. Shastry, and J. O. Haerter "Thermoelectric effects in a strongly correlated model for Na_xCoO_2" *Phys. Rev. B* **76** (16), 165118 [14 pages] (2007).

[109] B. S. Shastry "Electrothermal transport coefficients at finite frequencies" *Rep. Prog. Phys.* **72** (1), 016501 [23 pages] (2009).

[110] K. Miyake and H. Kohno "Theory of Quasi-Universal Ratio of Seebeck Coefficient to Specific Heat in Zero-Temperature Limit in Correlated Metals" *J. Phys. Soc. Jpn* **74** (1), 254-258 (2005).

[111] H. Eschrig "$T > 0$ ensemble-state density functional theory via Legendre transform" *Phys. Rev. B* **82** (20), 205120 [9 pages] (2010).

[112] A. W. Sandvik "Stochastic series expansion method with operator-loop update" *Phys. Rev. B* **59** (22), 14157-14160(R) (1998).

[113] O. F. Syljuåsen and A. W. Sandvik "Quantum Monte Carlo with directed loops" *Phys. Rev. E* **66** (4), 046701 [28 pages] (2002).

[114] T. Xiang, J. Lou, and Z. Su "Two-dimensional algorithm of the density-matrix renormalization group" *Phys. Rev. B* **64** (10), 104414 [6 pages] (2001).

[115] J. Rissler, R. M. Noack, and S. R. White "Measuring orbital interaction using quantum information theory" *Chem. Phys.* **323** (2-3), 519-531 (2006).

[116] M. C. Bañuls, D. Pérez-García, M. M. Wolf, F. Verstraete, and J. I. Cirac "Sequentially generated states for the study of two-dimensional systems" *Phys. Rev. A* **77** (5), 052306 [9 pages] (2008).

[117] K. Lanczos "An Iteration Method for the Solution of the Eigenvalue Problem of Linear Differential and Integral Operators" *J. Res. Natl. Bur. Stand.* **45** (4), 225-282 (1950).

[118] E. R. Davidson "The Iterative Calculation of a Few of the Lowest Eigenvalues and Corresponding Eigenvectors of Large Real-Symmetric Matrices" *J. Comput. Phys.* **17** (1), 87-94 (1975).

[119] G. L. G. Sleijpen and H. A. van der Vorst "A Jacobi-Davidson iteration method for linear eigenvalue problems" *SIAM J. Matrix Anal. Appl.* **17** (2), 401-425 (1996).

[120] K. G. Wilson "Renormalization Group and Critical Phenomena. I. Renormalization Group and the Kadanoff Scaling Picture" *Phys. Rev. B* **4** (9), 3174-3183 (1971); K. G. Wilson "Renormalization Group and Critical Phenomena. II. Phase-Space Cell Analysis of Critical Behavior" *Phys. Rev. B* **4** (9), 3184-3205 (1971).

[121] K. G. Wilson "The renormalization group and critical phenomena" *Rev. Mod. Phys.* **47** (4), 773-840 (1975).

[122] S. R. White "Density Matrix Formulation for Quantum Renormalization Groups" *Phys. Rev. Lett.* **69** (19), 2863-2866 (1992).

[123] S. R. White "Density-matrix algorithms for quantum renormalization groups" *Phys. Rev. B* **48** (14), 10345-10348 (1993).

[124] R. M. Noak and S. R. Manmana "Diagonalization- and Numerical Renormalization-Group-Based Methods for Interacting Quantum Systems" *AIP Conf. Proc.* **789** (1), 93-163 (2005).

[125] K. A. Hallberg "New Trends in Density Matrix Renormalization" *Adv. Phys.* **55** (5-6), 477-526 (2006).

[126] U. Schollwöck "The density-matrix renormalization group" *Rev. Mod. Phys.* **77** (1), 259-316 (2005).

[127] R. A. Molina, D. Weinmann, and J.-L. Pichard "Length-dependent oscillations of the conductance through atomic chains: The importance of electronic correlations" *Europhys. Lett.* **67** (1), 96-102 (2004).

[128] C. D. E. Boschi and F. Ortolani "Investigation of quantum phase transitions using multi-target DMRG methods" *Eur. Phys. J. B* **41** (4), 503-516 (2004).

[129] S. Östlund and S. Rommer "Thermodynamic Limit of Density Matrix Renormalization" *Phys. Rev. Lett* **75** (19), 3537-3540 (1995).

[130] N. Schuch, I. Cirac, and F. Verstraete "Computational Difficulty of Finding Matrix Product Ground States" *Phys. Rev. Lett.* **100** (25), 250501 [4 pages] (2008).

[131] F. Verstraete, D. Porras, and J. I. Cirac "Density Matrix Renormalization Group and Periodic Boundary Conditions: A Quantum Information Perspective" *Phys. Rev. Lett.* **93** (22), 227205 [4 pages] (2004).

[132] V. Murg, F. Verstraete, Ö. Legeza, and R. M. Noack "Simulating strongly correlated quantum systems with tree tensor networks" *Phys. Rev. B* **82** (20), 205105 [11 pages] ((2010)).

[133] F. Verstraete, J. J. García-Ripoll, and J. I. Cirac "Matrix Product Density Operators: Simulation of Finite-Temperature and Dissipative Systems" *Phys. Rev. Lett.* **93** (20), 207204 [4 pages] (2004).

[134] M. Zwolak and G. Vidal "Mixed-State Dynamics in One-Dimensional Quantum Lattice Systems: A Time-Dependent Superoperator Renormalization Algorithm" *Phys. Rev. Let.* **93** (20), 207205 [4 pages] (2004).

[135] T. Nishino "Density Matrix Renormalization Group Method for 2D Classical Models" *J. Phys. Soc. Jpn* **64** (10), 3598-3601 (1995).

[136] I. Schneider, A. Struck, M. Bortz, and S. Eggert "Local Density of States for Individual Energy Levels in Finite Quantum Wires" *Phys. Rev. Lett.* **101** (20), 206401 [4 pages] (2008).

[137] Y. Takahashi and H. Umezawa "Thermo field dynamics" *Collect. Phenom.* **2**, 55-80 (1975).

[138] M. Suzuki "Thermo Field Dynamics in Equilibrium and Non-Equilibrium Interacting Quantum Systems" *J. Phys. Soc. Jpn* **54** (12), 4483-4485 (1985).

[139] A. E. Feiguin and S. R. White "Finite-temperature density matrix renormalization using an enlarged Hilbert space" *Phys. Rev. B* **72** (22), 220401(R) [4 pages] (2005).

[140] S. Sota and T. Tohyama "Low-temperature density matrix renormalization group using regulated polynomial expansion" *Phys. Rev. B* **78** (11), 113101 [4 pages] (2008).

[141] P. Schmitteckert "Nonequilibrium electron transport using the density matrix renormalization group method" *Phys. Rev. B* **70** (12), 121302(R) [4 pages] (2004).

[142] R. B. Sidje "Expokit: A Software Package for Computing Matrix Exponentials" *ACM Trans. Math. Softw.* **24** (1), 130-156 (1998).

[143] W. H. Press, B. P. Flannery, S. A. Teukolsky, and W. T. Vetterling *Numerical Recipes: The Art of Scientific Computing* (Cambridge University Press, Cambridge, 1986), pp. 550-554.

[144] S. R. White and A. E. Feiguin "Real-Time Evolution Using the Density Matrix Renormalization Group" *Phys. Rev. Lett.* **93** (7), 076401 [4 pages] (2004).

[145] J. Jaklič and P. Prelovšek "Lanczos method for the calculation of finite-temperature quantities in correlated systems" *Phys. Rev. B* **49** (7), 5065-5068(R) (1994).

[146] M. Aichhorn, M. Daghofer, H. G. Evertz, and W. v. d. Linden "Low-temperature Lanczos method for strongly correlated systems" *Phys. Rev. B* **67** (16), 161103(R) [4 pages] (2003).

[147] B. V. Fine "Typical state of an isolated quantum system with fixed energy and unrestricted participation of eigenstates" *Phys. Rev. E* **80** (5), 051130 [19 pages] (2009).

[148] D. Bohr and P. Schmitteckert "Strong enhancement of transport by interaction on contact links" *Phys. Rev. B* **75** (24), 241103(R) [4 pages] (2007).

[149] P. Schmitteckert "Calculating Green functions from finite systems" *J. Phys. Conf. Ser.* **220**, 012022 [19 pages] (2010).

[150] R. M. Corless, G. H. Gonnet, D. E. G. Hare, D. J. Jeffrey, and D. E. Knuth "On the Lambert $\mathcal{W}$ function" *Adv. Comput. Math.* **5** (1), 329-359 (1996).

[151] E. Guilmeau, M. Poienar, S. Kremer, S. Marinel, S. Hébert, R. Frésard, and A. Maignan "Mg substitution in $CuCrO_2$ delafossite compounds" *accepted for publication in Solid State Comm.* [11 pages] (2011).

[152] R. Frésard and G. Kotliar "Interplay of Mott transition and ferromagnetism in the orbitally degenerate Hubbard model" *Phys. Rev. B* **56** (20), 12909-12915 (1997).

[153] L. Lewin *Polylogarithms and associated functions* (North Holland, New York, 1981), pp. 192, 236.

[154] A. Jonquière "Note sur la série $\sum_{n=1}^{\infty} \frac{x^n}{n^s}$" *Bulletin de la S. M. F.* **17**, 142-152 (1889).